Spectral modeling of Rhea, Dione, and Enceladus

A link to surface exogenic processes in the Saturnian system

Mateo Rejón López

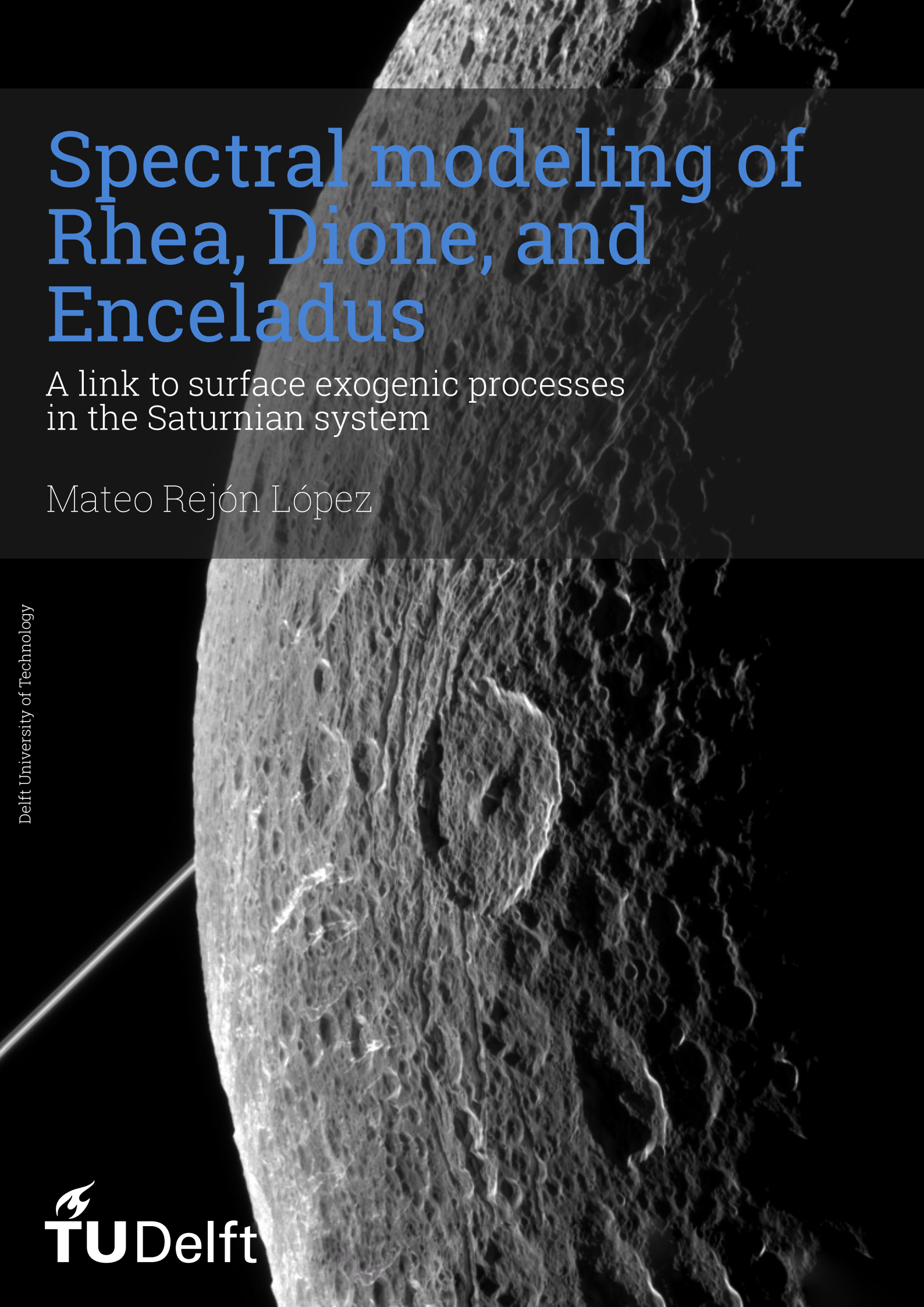

Delft University of Technology

TU Delft

Spectral modeling of Rhea, Dione, and Enceladus

A link to surface exogenic processes in the Saturnian system

by

Mateo Rejón López

Student Name	Student Number
Rejón López, Mateo	5622352

Supervisor: S. Cazaux
Project Duration: April 2023 - December 2023
Faculty: Faculty of Aerospace Engineering, Delft

Cover: PIA17195: Dione's Craggy Surface (Credit: NASA/JPL-Caltech/Space Science Institute)

TU Delft

Preface

Last Summer, I found myself wandering around the *Carmen de los Mártires*, an iconic residence in Granada with a magical garden and exotic architecture, when I came across an untitled poem from Rafael Guillén that caught my eye. Its first sentence can be translated as *"we always arrive at the wrong time"*, or in the words of Rafael,

"Siempre llegamos a destiempo."

Two years before that I set foot in a city I never heard about, knowing nobody and carrying nothing but two suitcases. Little did I know that the four walls I was going to live in for the 2 years to come were going to give a new definition of *home*. Home turned into warm hugs in the morning, coffee table conversations about everything and nothing at the same time, painting walls following the craziest ideas (not always with good results), watching movies in an improvised cinema, and uncountable dinners. We laughed, danced, cried, hugged and loved each other.

This new definition of home includes a varied group of Spanish people who kept me grounded, creating the space to celebrate what unites us and grow together through our differences. Either by playing boardgames, fantasizing about creating a political party or cooking almost every Sunday, you showed what I want my life to be. Thank you for becoming a family and being a ray of sunlight in this cold country.

And the home that will always be home. This work is for all of them. To my parents for setting the example of who I want to become and being there to pick me up if I fall. To my brother, who will always be an integral part of who I am. To Mario, for being there even thousands of kilometers apart. To Alba, whose strength and talent is an endless source of inspiration.

Thank you very much Stéphanie for your constant support and guidance throughout this work and for being a role model beyond professional life. Our discussions outside of Saturn and its moons helped me a lot to navigate the uncertainty of entering a new life stage, as I step out of student life. Moreover, I would like to thank Marie for the immeasurable help with the hustle that the Hapke model represents.

While reading Guillen's poem in Granada, it made me think of a distant home, more than 2,000 kilometers away. Now, I understand that home is where the people you love are. From Granada to Delft and stopping by Cologne, I will be happy to always arrive at the wrong time if it is with all of you. You are my home.

Mateo Rejón López
Delft, December 2023

Summary

A new era of exploration is on the horizon with missions such as the James Webb Space Telescope and the JUpiter Icy Moons Explorer (JUICE), focusing on the enigmatic icy moons within our solar system. Previous missions, like the Cassini-Huygens mission, have provided an invaluable wealth of data regarding Saturnian moons, shedding light on their intricate characteristics. However, despite past studies, a clear link between various surface-altering processes—such as E-ring bombardment, meteoroid impacts, photolysis, dark material, plasma, and energetic electron bombardment—and terrain features has not been fully explored.

This investigation employs the Hapke photometric model to fit the reflectance spectra of the icy moons by using a Least Squares Method algorithm. A novel validation approach is followed by utilizing experimental data obtained from crushed ice particles sourced from the Solid Spectroscopy Hosting Architecture of Databases and Expertise (SSHADE). Additionally, this data serves as a testing ground for innovative techniques in estimating crystallinity based on the 2- and 1.65-micron absorbance features of water ice.

By using data from Cassini's Visual and Infrared Mapping Spectrometer (VIMS), this thesis delves into the characteristics of the icy regolith on moons such as Rhea, Dione, and Enceladus. The analysis encompasses three studies: well-resolved terrain units, variations across an entire moon following their longitudinal lines, and a comparative examination of primary regions affected by various exogenic processes between the different moons.

The results of this study underscore the distinct impacts of each process on the icy regolith. In conclusion, by observing surface features such as grain sizes, crystallinity and surface roughness, it is possible to determine which processes are dominating on the moon's surface. Knowing how these characteristics evolve with time, such observations could also be used to determine (relative) ages of the surface's features.

Contents

List of Figures

List of Tables

Nomenclature

Abbreviations

Abbreviation	Definition
AU	Astronomical unit
CBOE	Coherent backscattering opposition effect
CCD	Charge-Coupled Device
CIRS	Composite Infrared Spectrometer
DN	Data Number
FPA	Focal Plane Assembly
IR	Infrared
ISS	Imaging Science Subsystem
JPL	Jet Propulsion Laboratory
JUICE	JUpiter Icy Moons Explorer
LDA	Low-Density Amorphous
LPG	Laboratory of Planetology and Geodynamics
NASA	National Aeronautics and Space Administration
NIR	Near-Infrared
SHOE	Shadow-hiding opposition effect
SPIPA-B	Icy Planetary Analog Producer—B
SSHADE	Solid Spectroscopy Hosting Architecture of Databases and Expertise
UV	Ultraviolet
UVIS	Ultraviolet Imaging Spectrograph
VIMS	Visible and Infrared Mapping Spectrometer

Symbols

Symbol	Definition	Unit
B_{C0}	CBOE amplitude	[-]
B_{CB}	CBOE function	[-]
B_{S0}	SHOE amplitude	[-]
B_{SH}	SHOE function	[-]
D	Grain size	[μm]
H	Ambartsumian–Chandrasekhar function	[-]
$\hat{H}$	Hessian matrix	[-]
I/F	Radiance factor	[-]
J	Jacobian matrix	[-]
K	Compaction correction	[-]
M	Multiple scattering function	[-]
P	Particle phase function	[-]
Q_E	volume-average extinction coefficient	[-]
Q_S	Volume-average scattering efficiency	[-]
$\hat{R}$	Correlation matrix	[-]
R	Radius	[km]
$R(0)$	Fresnel reflection coefficient	[-]
S	Shadowing function	[-]

Symbol	Definition	Unit
S_e	Total fraction of incident light reflected into all directions	[-]
S_i	Fraction of internally reflected light	[-]
T	Temperature	[K]
I	Oberver's direction	[-]
J	Incident radiation direction	[-]
N	Perpendicular direction	[-]
b	Asymmetry parameter	[-]
c	Backscattering fraction	[-]
e	Emergence angle	[rad]
g	Phase angle	[rad]
h_C	CBOE angular width	[-]
h_S	SHOE angular width	[-]
i	Incidence angle	[rad]
k	Extinction coefficient	[-]
m	Mass fraction of amorphous ice	[-]
n	Refractive index	[-]
$\hat{n}$	Complex refractive index	[-]
p	Porosity	[-]
r	Bidirectional reflectance	[-]
Λ	Mean free path	[μm]
Θ	Internal transmission factor	[-]
α	Absorption coefficient	[-]
λ	Wavelength	[μm]
μ	Location of the 2-micron feature	[μm]
μ_{0e}	Effective cosine of i	[-]
μ_e	Effective cosine of e	[-]
ϕ	Filling factor	[-]
ψ	Azimuth angle	[rad]
$\bar{\theta}$	Surface roughness	[rad]
ρ	Density	[kg/m^3]
$\sum$	Covariance matrix	[-]
$\bar{\omega}$	Single-scattering albedo	[-]

Definitions

Term	Definition
Trailing hemisphere	Side of a celestial body, such as a moon or planet, that faces away from its direction of orbital motion (180°W)
Leading hemisphere	Side of a celestial body that faces in the direction of its orbital motion (90°W)
Saturnian hemisphere	Saturnian moon's side facing the planet (0°W)
Anti-Saturnian hemisphere	Saturnian moon's side facing opposite to the planet (180°W)
Regolith	Loose layer of fragmented material covering the surface of a celestial body

1 Introduction

The solar system is home to a wealth of fascinating worlds, although few have captured the attention of scientists and the public as much as Saturn and its moons. This gas giant has a ring system unlike any other that has ever been observed. This alone is captivating; however, its varied and rich range of moons adds a greater scientific interest to the system. Previous missions, including the pioneering Voyager missions in the late 20th century, offered initial glimpses into the Saturnian system, awakening the fascination with these distant moons. The Cassini-Huygens mission furthered the understanding, providing detailed observations and uncovering the diverse geological features of the icy moons; such as a prime example of cryo-volcanism in Enceladus. Before these missions, the knowledge of Saturn's icy moons relied primarily on telescopic observations. Accurate measurements were only made possible by in-situ observations, which provided crucial information about what happens on their surfaces on a very local scale [1].

Even though spacecraft observations have provided detailed close-up views of the Saturnian icy moons, it is essential to estimate the physical properties of the regolith to understand the overall characteristics of these satellites. By studying the moons' surfaces in detail, especially considering different terrains and geological features, a more nuanced understanding of how their physical properties vary can be developed. Modeling radiative transfer in planetary regoliths is paramount for interpreting their spectral observations in the context of surface physical properties. The wavelength-dependent light-scattering behavior is influenced by regolith properties like particle albedos, grain microstructure, compaction state, and surface texture.

The Cassini mission brought about a revolution by conducting close-up observations, capturing high-resolution images, and collecting a wealth of data in a wide range of illumination conditions. Cassini's extended mission allowed for repeated and comprehensive observations over time, revealing dynamic processes, seasonal changes, and the effects of external influences on the icy moon surfaces. The spacecraft's findings shed light on potential habitats for life, particularly in the case of Enceladus.

The study of icy moons carries profound implications for understanding the richness of planetary evolution and the potential for life beyond Earth. These moons may harbor clues about the fundamental processes shaping planetary bodies and the conditions necessary for the emergence of life. As new missions aim to investigate icy worlds (such as the JUpiter Icy Moons Explorer, JUICE), this project provides several tools to determine the dynamic interactions at play on icy moons. By connecting the dots between spectral modeling, regolith characteristics, and surface exogenic processes, a comprehensive understanding of the intricate interactions shaping the Saturnian system's geological history is achieved, contributing valuable insights to the broader field of planetary science.

1.1. Research question

Surface exogenic processes are those that affect the state of the icy region on the uppermost layers of a celestial body and that have an external origin. They play a crucial role in shaping and altering the surfaces of Saturnian satellites. These phenomena can sometimes have opposite effects, making it challenging to estimate the regolith's age and evolution. Meteoroid impacts, for example, heat up the surface layers, leading to melting and vaporization of material that increases grain size and reduces

porosity [2]. On the contrary, E-ring particle deposition adds new material to the surface, with smaller grains [3].

A significant knowledge gap remains in understanding how different surface processes interact and influence each other. Establishing clear links between surface processes and regolith characteristics is essential for drawing a complete picture of the evolution of icy bodies. Studies linking photometric observations of the icy moons with particular surface processes have been developed [4]. Yet, a link between the different processes and regolith characteristics has been overlooked. Hence, this research aims to answer the following research question:

> ***How do exogenic surface processes affect the regolith characteristics on the icy moons?***

The main research question can be decomposed into sub-questions:

A. *What are the challenges and limitations of applying the Hapke model to icy moon regolith?*

B. *Which techniques can be used to estimate the degree of crystallinity using VIMS data?*

C. *What are the regolith characteristics of different terrain units within the icy moons?*

D. *How do regolith characteristics vary across different regions of icy moons?*

E. *How do the regolith characteristics change between different icy moons?*

1.2. Thesis outline

This thesis is organized into chapters presenting the relevant information required to address the research questions. Chapter 2 presents an overview of the Saturnian system and dives into the surface features of the icy moons studied in this work (Rhea, Dione, and Enceladus), as well as presenting the external surface processes taking place in the system. Chapter 3 provides an introductory overview of spectroscopy, emphasizing its ability to analyze matter based on electromagnetic radiation interactions. It covers the spectra of celestial bodies, explores the spectral characteristics of water ice relevant to Saturn's icy moons, and introduces the Hapke model to establish a foundational framework for subsequent discussions in the work.

Chapter 4 outlines the data sources used in the study, covering the extraction and use of optical constants, details of data obtained from Cassini's Visible and Infrared Mapping Spectrometer (VIMS), and the theoretical framework for performing spectral fits to obtain the surface characteristics from lab data and the icy moons. Chapter 5 addresses two main aspects: utilizing experimental data from the Solid Spectroscopy Hosting Architecture of Databases and Expertise (SSHADE) to validate the fitting procedure of the Hapke model and exploring techniques for ice crystallinity estimation. The utilization of laboratory data presents a novel approach to assess the quality of the model and highlight its limitations and caveats.

Chapter 6 analyzes VIMS data at various scales, examining well-resolved terrain units, longitudinal lines, and main areas affected by exogenic processes across Rhea, Dione, and Enceladus, providing insights into regolith characteristics from the smallest scales resolved by the VIMS instrument to the planetary level. Finally, the conclusions and future work are highlighted in Chapter 7, together with answers to the research questions.

The software developed for this work has been made publicly available: `https://github.com/mrejonlopez/Hapke-Model`.

2

Saturnian System and the icy moons

This chapter extensively explores the Saturnian system, a selection of its icy moons (Rhea, Dione, and Enceladus), and the action of the different exogenic surface processes that shape the icy regolith. First, Section 2.1 presents the Saturnian system, including the satellite and ring systems. Then, Section 2.2 provides a comprehensive overview of the moons' surfaces, delving into key aspects such as topography, grain size, ice morphology, and surface temperatures. Particularly, the different phenomena of Enceladus are presented, including its subsurface ocean and plumes emanating from its southern terrain. Finally, Section 2.3 delves into the external processes that exert influence on the surfaces of these moons.

2.1. Saturnian System

Saturn, positioned as the sixth celestial body in the solar system relative to the Sun and ranking second in mass behind Jupiter, has a semi-major axis of approximately 9.6 astronomical units (AU). The orbital period of this gas giant spans 29.46 Earth years, while rotation around its axis takes 10 hours and 39 minutes, resulting in a spheroid shape. Saturn is mostly made of hydrogen and helium and was formed together with the other planets around 4.5 billion years ago, stabilizing into its present orbit four billion years before [5]. The gas giant's icy particle rings extend outward up to 282,000 km from the planet. These rings, designated alphabetically in order of discovery, contain primary bands designated as rings A, B, and C, with supplementary, yet fainter, rings D, E, F, and G.

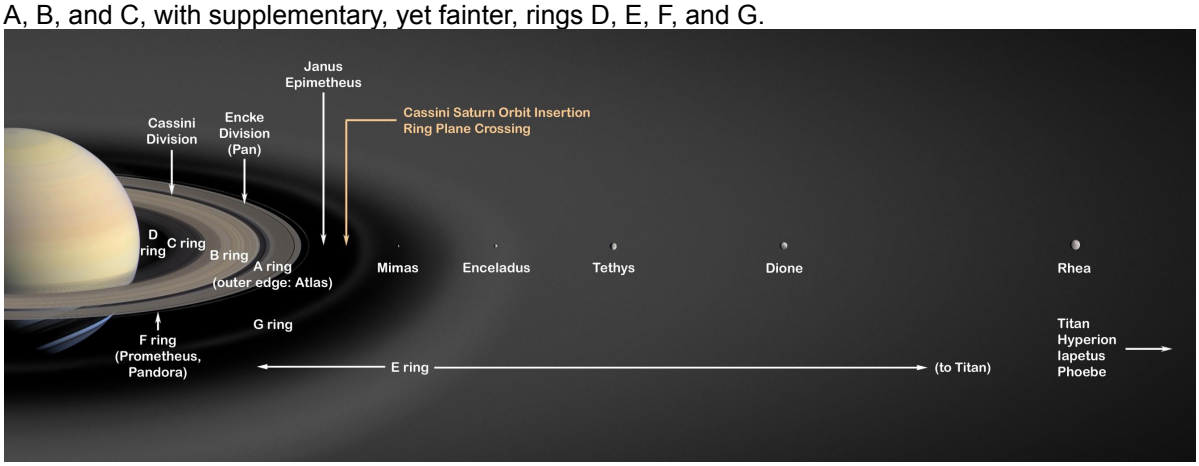

Figure 2.1: Artist's Concept of Saturn's rings and major moons. Credit: NASA/JPL.

Saturn harbors a diversity of moons, totaling 63 confirmed and named satellites, varying in size from moonlets, measuring tens of meters, to Titan, surpassing the size of Mercury [6]. The spatial arrangement of the rings, including distinctive features like the Cassini Division, and primary moons are shown in Fig. 2.1.

The entirety of the Saturnian system resides within Saturn's magnetosphere, having an intensity 578 times that of Earth's. The magnetic field of Saturn experiences modulation owing to the presence

of its rings and moons. The rings act as absorbers of plasma, while ionization from photo-sputtering and ion strikes contributes to the overall plasma content. Moreover, Enceladus' plumes eject water and icy particles, that are ionized and constitute an additional source of plasma. Titan's upper atmosphere and the solar wind, also contribute as minor plasma sources [7].

2.2. Icy moons

Two groups can be identified in Saturn's diverse moon population: an inner group orbiting within 3.6 million km and a more distant cluster situated at approximately 11 million km. The inner moons constitute a regular group, characterized by prograde orbits with low inclinations and eccentricities. On the other hand, the outer moons, forming the second group, exhibit irregular orbits, with over half displaying retrograde motion, and large inclinations and eccentricities [5].

Saturn's satellite system is dynamically intricate, featuring prominent three-body resonances. Notably, three pairs of moons exhibit resonances: Mimas and Tethys (4:2), Enceladus and Dione (2:1), and Titan and Hyperion (4:3) [8]. The gravitational influence of these moons induces destabilizing regions in the adjacent rings, resulting in the formation of gaps within them.

Titan, Saturn's largest moon, was first observed by Huygens in 1655. Subsequent discoveries by Giovanni Cassini, between 1671 and 1684, included Tethys, Dione, Rhea, and Iapetus. William Herschel added Mimas and Enceladus to the list in 1789, while Hyperion was discovered in 1848 by W. C. Bond, G. P. Bond, and William Lassell. Phoebe, identified in 1899 through observational data, paved the way for the discovery of additional minor moons by the Voyager probes, Pioneer, and Cassini spacecraft.

In this study, three particular moons are studied: Rhea, Dione, and Enceladus. The coordinates system defined on the moons locates their prime meridian (the one with 0° longitude) in the Saturnian hemisphere, as all Saturnian satellites are tidally locked. In the western direction, there is the leading hemisphere, at 90°W, which always faces the moon's direction of motion. After it comes to the anti-Saturnian hemisphere, facing away from the planet at 180°W, and the trailing hemisphere, opposite to the direction of motion at 270°W. Each moon features different terrains that are related to the region where they are, and throughout this work, this coordinate system and terminology is extensively used.

2.2.1. Rhea

Rhea has a radius of 764 km and is the second-largest Saturnian satellite, after Titan. This icy moon exhibits a generally heavily cratered surface, with modeled ages between 4.2 and 3.6 Gyr. Its density and moment of inertia point toward a largely homogeneous interior, made of a mixture of 75% H_2O and 25% rocky material. It is tidally locked to Saturn and has an orbital period of approximately 4.5 Earth days. Rhea orbits Saturn at a distance of 527,040 km, immersed in the planet's magnetosphere.

A depiction of its terrain is shown in Fig. 2.2. Its leading hemisphere is a geologically younger surface, featuring a bright, less cratered terrain, that seems to be a result of tectonism [9]. Rhea also presents chains of small, dark spots along its equator, that can be attributed to denser ring or exogenic material.

Rhea's surface is primarily composed of H_2O ice. The different moons show different degrees of contamination with rocky/organic material, causing a darkening of the surface. These contaminants are believed to have a common origin across all moons and are suggested to come from the interaction with solar UV radiation, cosmic rays, or plasma [11]. This dark terrain populates the trailing hemisphere of Rhea, which also features fractures and wisps, similar to those found in Dione.

Rhea's North polar region can be classified in two different types: bright terrain in the trailing zone with large craters (>30 km in diameter), and darker terrain in the leading side with smaller craters (<30 km). In the northern hemisphere, the largest impact crater of Rhea, Tirawa, is located, expanding over 350 km [12].

A prominent feature of Rhea is the presence of the Inktomi crater, a particularly young crater in the leading hemisphere, located at 14°S 112°W, shown in Fig. 2.2 in yellow and Fig. 2.3. This crater was most likely formed by a head-on collision that led to the deposition of fresh material in the nearby area, forming bright rays in the terrain [13].

Through remote sensing, the state of the icy regolith can be inferred. Particularly, Rhea's regolith is believed to be quite porous, with porosity values ranging between 80 and 99% [1]. Through Hapke

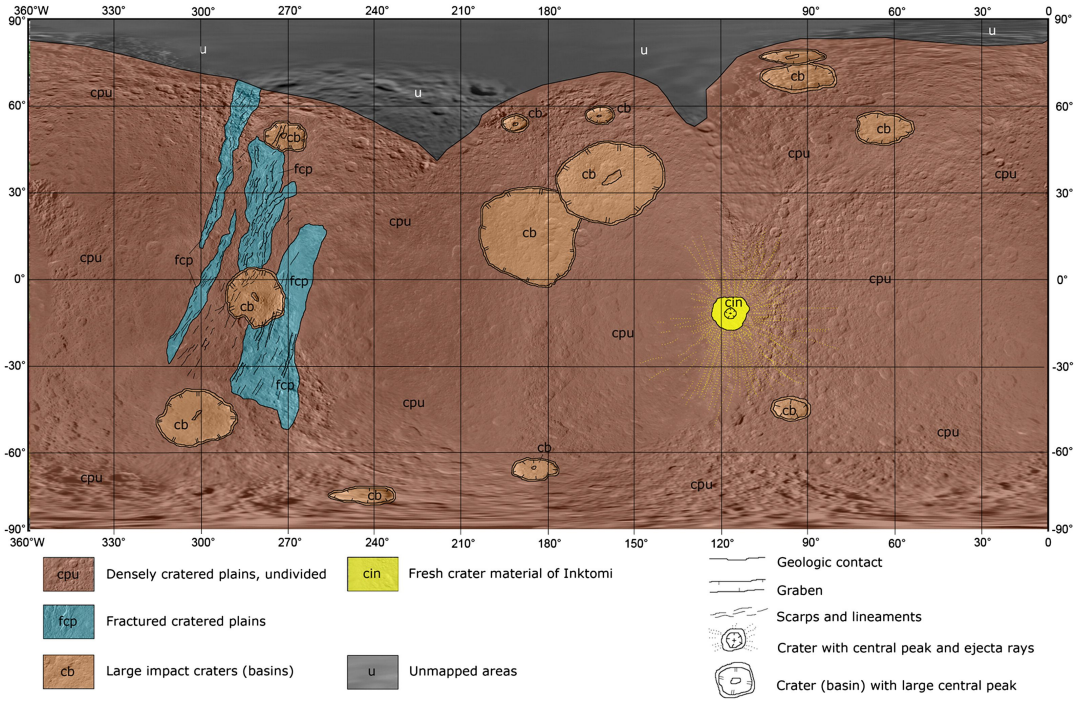

Figure 2.2: Simplified geological map of Rhea's surface overlaid onto Cassini ISS (Imaging Science Subsystem) images [9].

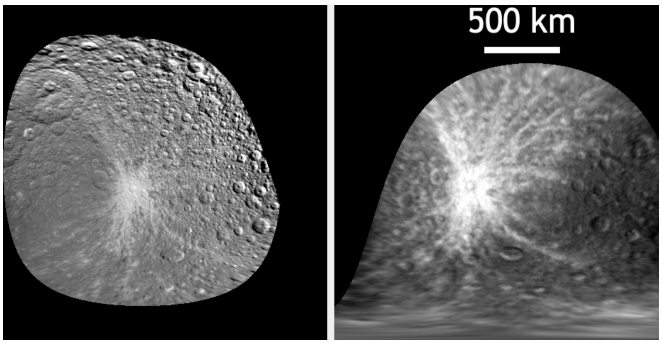

Figure 2.3: Cylindrical projections of the Inktomi crater and the extent of its bright ray system. The images expand from 90°N to 90°S and 60° to 160°W [10].

modeling, the particle sizes of Rhea have been estimated to be in the range of 10 to 30 microns, being smaller in the dark terrain of the trailing hemisphere [14].

G. Filacchione, et al. (2016) [15] looked at the spectral position of the temperature-dependent 3.6 microns broad interband peak measured by Cassini VIMS to determine the full disk spectra temperature of the Saturnian icy moons and develop temperature maps. In the case of Rhea, the differences in albedo and topography between the leading and trailing hemispheres lead to different daytime temperatures. Particularly, the leading hemisphere, around 125 K, while the trailing hemisphere reaches temperatures up to 150 K. Colder temperatures, less than 110 K, are found in the northern hemisphere during winter and the Inktomi crater also presents a reduced temperature (110 K) compared to its surrounding area.

2.2.2. Dione

Dione is one of Saturn's major satellites and orbits at a distance of 377,400 km, between Tethys and Rhea, deep inside the system's magnetosphere. Its mean radius is 562 km and it is made primarily of water ice. However, as one of the densest moons (after Enceladus and Titan), it is believed to have a considerable amount of rocky material ($\sim$45%). This satellite orbits Saturn every 2.7 Earth days [16].

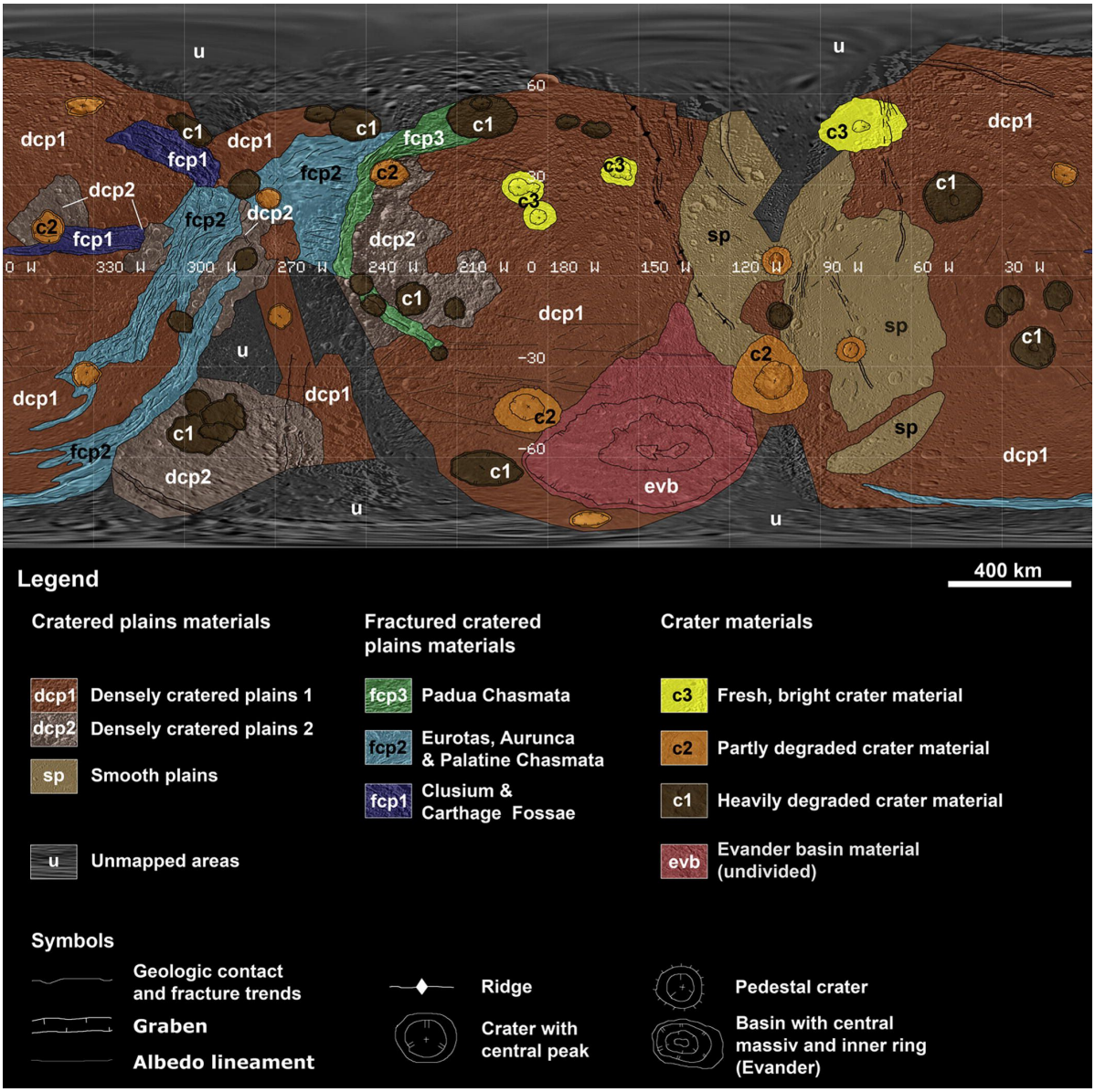

Figure 2.4: Simplified geological map of Dione's surface overlaid onto Cassini ISS images [16].

A depiction of its terrain can be found in Fig. 2.4, featuring a geologically complex surface. One of this moon's peculiarities is the network of bright, linear, or curved contours, pointing toward a geologically young surface; especially at the trailing hemisphere. Dione exhibits a prominent chasma system in its trailing hemisphere, that runs over darker material, similar to the one found in Rhea [17].

Fig. 2.4 shows the different terrain classifications: densely cratered plains (occupying most of the surface of the anti-Saturnian and Saturnian hemispheres), smooth plains (at the leading side) fractures cratered plains (at trailing), and crater material. The unmapped regions represent geologically ambiguous terrain. The densely cratered plains are characterized by high albedo and rough terrain, due to densely packed impact craters, contrary to the smooth plains' low crater density. The fractured cratered plains are displayed in Fig. 2.5 and feature evidence of endogenic activity; particularly, at the "wispy terrain" on the trailing hemisphere. The Eurotas and Aurunca Chasmata dominate the center of Dione's trailing hemisphere, while the younger Padua chasmata cross over them and expand farther East. Finally, impact crater material depict younger crater; among which Creusa is the most recent and prominent one, with ejecta rays as Inktomi in Rhea [17]. The Creusa crater is shown in Fig. 2.5 and is located at 49°N, 76°W. Its ray system extends several hundred kilometers across most of the leading hemisphere [18].

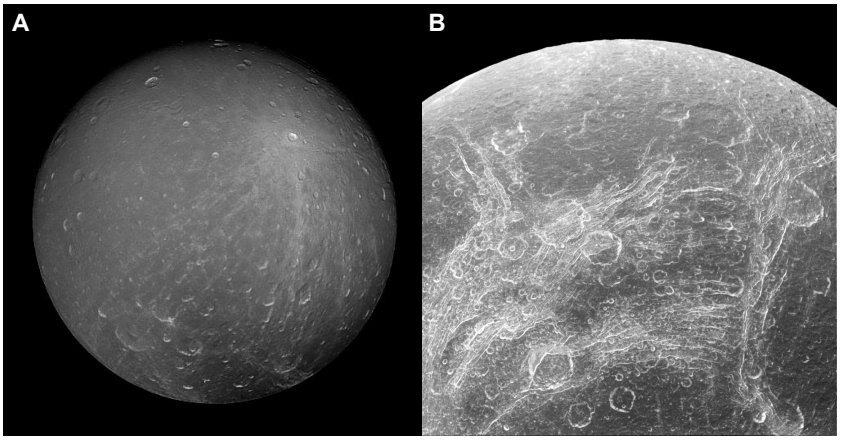

Figure 2.5: Cassini ISS image of (A) Dione's leading hemisphere, featuring the Creusa crater and its ray system and (B) wispy terrain, showing the prominent chasmata system and dark material. Credit: NASA/JPL-Caltech/Space Science Institute.

Dione's leading hemisphere is greatly affected by E-ring particle deposition, making it 40% brighter and more icy than the trailing hemisphere. The leading hemisphere also has spectra related to grain sizes of 10-20 μm while the trailing one has spectra compatible with smaller grain sizes (<10 μm). Dione also has a weak CO_2 absorption band that is non-uniformly distributed, being concentrated in the discolored material on the trailing hemisphere [14].

Furthermore, the trailing hemisphere presents the highest temperature, 140 K. A great area of the leading hemisphere has a temperature of 115 K, northern regions reach 90 K during the winter season and a few pixels' temperatures go down to <88 K in the bright terrains near the Creusa crater. Pre- and post-equinox maps show that seasonal change is well evident, as the south hemisphere becomes cooler (<88 K) while the dark unit of the leading hemisphere remains at a stable temperature [15].

2.2.3. Enceladus

Enceladus is one of the mid-size satellites of Saturn, with a radius of 504 km. It orbits Saturn at a distance of 238,000 km, taking approximately 1.4 Earth days to complete an orbit around the gas giant. This moon is known for its active fractures in the south pole, the so-called "tiger stripes", from where supersonic jets of vapor and ice are ejected into the Saturnian space and populate Saturn's E-ring. Enceladus' density suggests $\sim$60% of its mass is made of rocky material, while ice makes the other 40% [19].

Surface

Enceladus' surface is depicted in Fig. 2.6 and showcases the diversity of its terrain, featuring cratered and uncratered areas, extensive depressions, tectonic structures, and profound fissures within the south polar region [19]. The oldest terrains on Enceladus are the cratered regions expanding from the Saturnian hemisphere, over the north pole, to the anti-Saturnian side. Due to a combination of viscous relaxation and bombardment of plume material, many of the craters are shallower than in other moons [20]. The terrains on the leading and trailing sides are dominated by intense tectonism, exhibiting curved sets of parallel ridges. Crater density decreases from north to south, where the plumes act as a main resurfacing agent [21].

Fig. 2.7.A shows the plumes emanating from the tiger stripes' sulci. These depressions exhibit a distinctive bluish hue and a darker albedo compared to the surrounding icy expanse, as illustrated by Fig. 2.7.C, which also gives the names of each fault [23]. ISS (Imaging Science Subsystem) measurements have revealed that the tiger stripes are comprised of four parallel faults, each extending approximately 130 km in length, 2 km in width, and spaced at an average separation of about 35 km. Each stripe features a depth of roughly 500 m and is flanked by a ridge standing at 100 m in height. The emanating plume material, possessing a darker appearance, extends several kilometers on either side of these features [24]. By measuring the thermal radiation of the area in the 10-16 μm range, the temperature of the south polar region could be estimated, as shown in the thermal maps in Fig. 2.8.

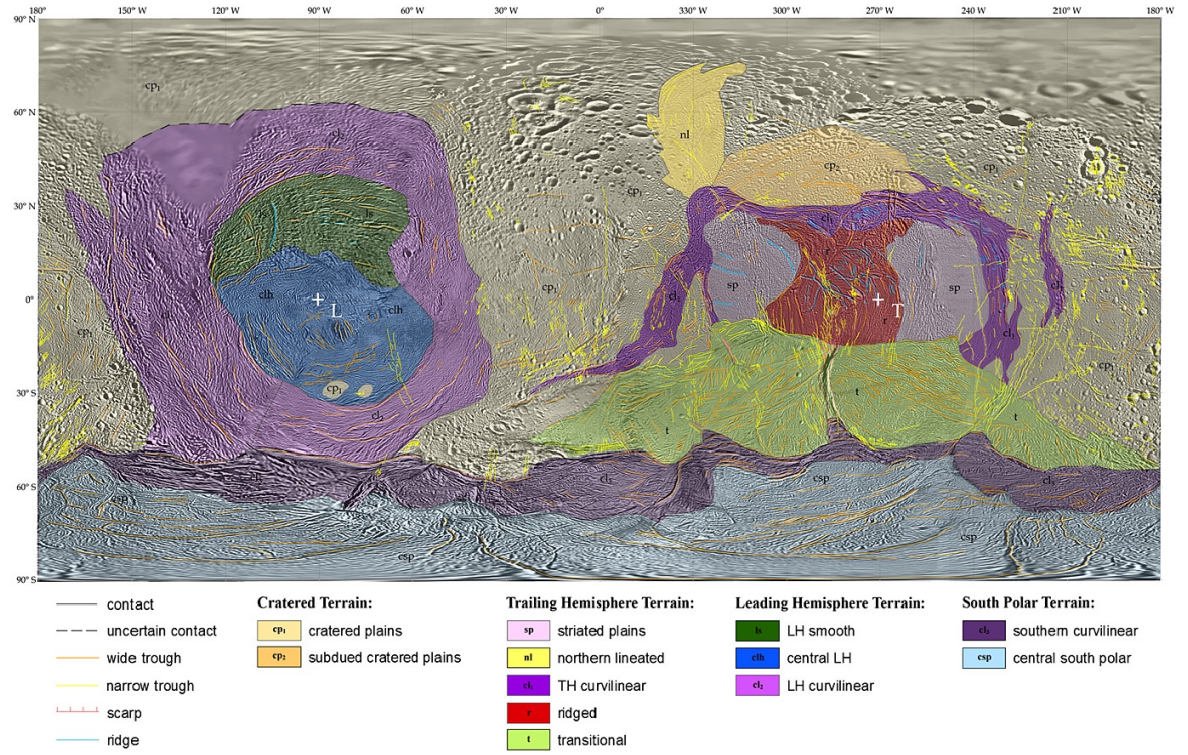

Figure 2.6: Simplified geological map of Enceladus' surface overlaid onto Cassini ISS images [22].

The tiger stripes are particularly hot, having temperatures of up to 85 K, compared with the surrounding terrain, which reaches temperatures of about 60 K.

Enceladus primarily comprises water ice, with the presence of trapped CO_2 in diverse locations, such as the tiger stripes. Cassini VIMS observations have shown a correlation between geologic features and particle size, with larger particles prevalent in the south polar region and smaller ones in older, densely cratered terrain [25]. Reflectance spectroscopy has revealed trace organic compounds within the south-polar terrain, characterized by absorption features associated with aliphatic hydrocarbons. Particularly, NH_3 and methanol traces have been identified in the vicinity of the tiger stripes [26, 27]. Cassini UVIS (Ultraviolet Imaging Spectrograph) measurements suggest a prevalence of crystalline ice on the surface of Enceladus, with a shift to shorter wavelengths indicative of amorphous ice [28]. Observations in ultraviolet and far ultraviolet wavelengths suggest the presence of contaminants causing surface darkening [29].

The identification of CO_2, likely originating from plume deposition, is manifested in various forms, including ice, complexed CO_2, or CO_2 clathrate hydrates. Trapped CO_2 stands out as the sole component identified with certainty, while concentrations of NH_3 remain below 2% [23, 26]. The surface is notably influenced by plume deposition of micro-sized ice grains, particularly prominent in the south polar region, where the constitution of ejecta prevails. Non-icy components from the plumes, such as sodium salts and organic compounds, are estimated to be present in proportions close to 1% on the surface [29].

Numerical models have been used to map particle deposition coming from the plumes with eight ice-particle jets [30]. The deposition rates for various particle sizes, as illustrated in Fig. 2.9, correlate with the IR/UV measurements acquired by Cassini. Smaller particles travel greater distances from the tiger stripes, with the smallest particles escaping Enceladus' gravitational influence.

Plumes and subsurface ocean

The plumes originating mainly from the four tiger stripes, with occasional isolated jets emitted from simple open fractures along the surface, are estimated to have a source rate of 200-300 kg/s [31, 32]. These plumes serve as a source of evidence for the presence of a liquid water ocean beneath

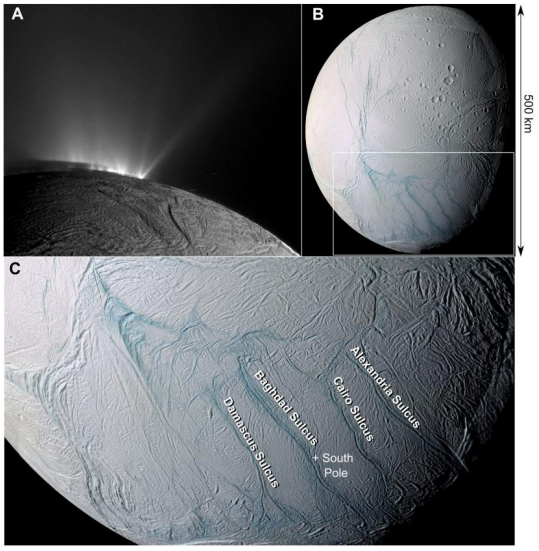

Figure 2.7: Enceladus' surface observed in the visible by Cassini's ISS instrument. (A) plumes emanating from the active south polar region, (B) an enhanced color map, and (C) a close-up view of the south polar terrain and labeling of the four active faults. Colors are enhanced, giving the blue-green appearance to the active faults [23].

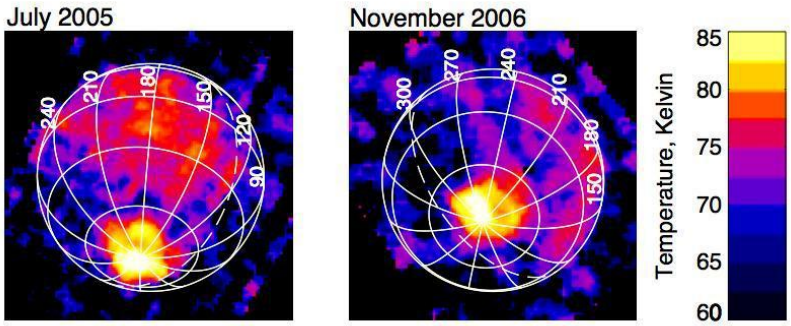

Figure 2.8: Temperature map of Enceladus derived from the thermal radiation in the 10-16 μm wavelength range recorded by CIRS (Composite Infrared Spectrometer) during one of Cassini's flybys. The left image was captured 16 months earlier than the right one. Credit: NASA/JPL/Southwest Research Institute.

Enceladus' icy crust, offering an opportunity to study its characteristics. These jets comprise three phases: solid (dust), gas, and ions. The plumes predominantly feature water as the most abundant component [33].

Fractures within Enceladus's southern region are thought to penetrate the entire thickness of the ice shell, likely filled predominantly with liquid water directly sourced from the subsurface ocean. Tidal heating-induced melting counteracts the narrowing of fractures due to viscous creep and the freezing of water onto the walls [33]. The water level within these fissures is expected to be situated around 10% of the way down to the ocean, where solid particles are believed to be generated through the bursting of bubbles at this level. The freezing of the water surface is prevented by water vapor pressure buildup above the water surface, a result of the combination of narrowing fractures toward the surface, throttling of escaping vapor in the fractures, and salinity-driven overturn or dissipative heating of the water.

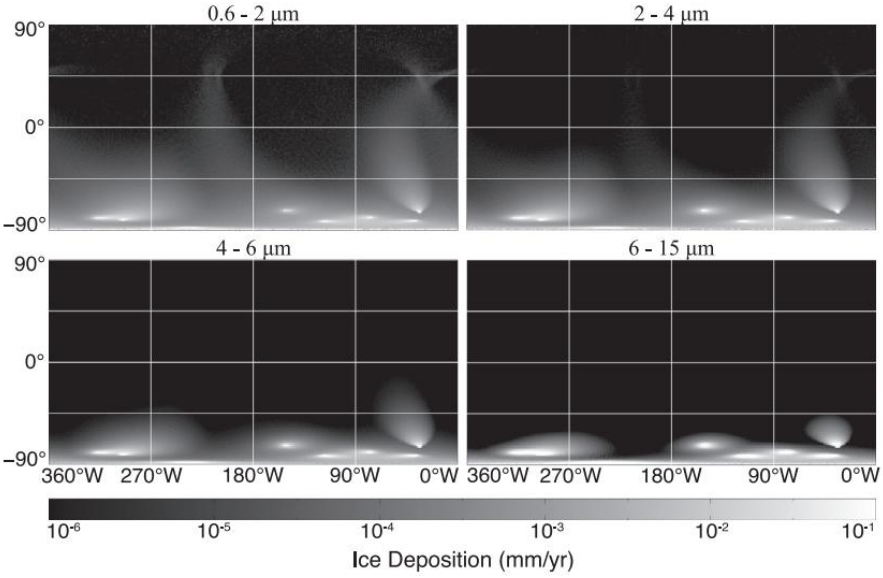

Figure 2.9: Plume particle deposition model rates on Enceladus surface on mm/year for particle sizes between 0.6 and 15 μm [30].

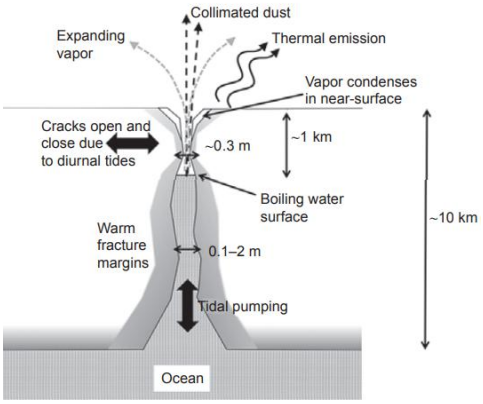

Figure 2.10: Major processes driving plume emission from subsurface ocean [33].

Figure 2.10 illustrates the major processes driving plume emission from the subsurface ocean [33]. Tidal stresses induce lateral motion on the upper section of the cracks, causing periodic opening and closing of the fissures; triggered by the orbital resonance with Dione and Saturn. Additionally, tidal pumping propels subsurface liquid water up the fracture, reaching a level where the water begins to boil and generate vapor. Near the surface, water vapor condenses, narrowing the conduit, and resulting in increased pressure and particle velocity.

Feeding the E-ring

In addition to surface deposition on Enceladus itself, the plumes serve as the primary source of material for the faint E-ring in the Saturnian system, with approximately 5-10% of emitted ice grains escaping Enceladus' gravity field [34]. The particles ejected into the ring influence the system's magnetosphere and coat the surfaces of nearby satellites.

Numerical models predict that the required escape velocity of a plume particle depends on its size and the location of the jet on the surface [35]. This model suggests that between 7.9 and 10.4% of individual jet particles contribute to the ring. The production rate of E-ring particles by Enceladus vents is predicted to be 51 $\pm$ 18 kg/s, implying a lifetime of approximately 8 years for E-ring particles [36].

Observations from the Hubble Space Telescope reveal that the material emitted by Enceladus alters the appearance of neighboring moons. Fig. 2.11 illustrates the strong correlation between the amount of material present in certain regions of the E-ring and the albedo of the Saturnian moons Tethys, Mimas,

Dione, and Rhea. The ejecta resulting from high-velocity impacts with E ring particles coat the surfaces with clean icy microstructures that enhance the albedo of these moons [37].

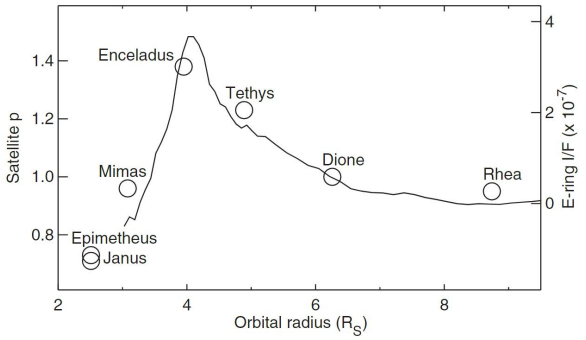

Figure 2.11: Mean visual albedo p of the Saturnian moons plotted against their distance to Saturn. The solid line and right scale represent the E ring pole-on radial reflectance profile [37].

2.3. Surface exogenic processes

A. R. Hendrix et al. (2018) [4] conducted an investigation into the disk-integrated characteristics of Saturn's icy moons in both the UV and IR spectra. The study aimed to establish a correlation between various exogenic processes that release energy onto the surfaces of these moons and the resulting spectral features within this wavelength range. The spectra obtained from these observations revealed distinctive features that could be linked to external processes impacting the surface characteristics of specific regions on the icy moons.

The trailing hemispheres of the icy moons whose orbit lay within Saturn's magnetosphere suffer from the impact of corotating cold plasma, causing the darkening of their surfaces. Electron and ion impacts also trigger chemical reactions that yield an increase in species as H_2O_2, O_2, and O_3 in the icy regolith. On the other hand, particularly energetic electrons hit the leading hemispheres, liberating energy that increases the thermal inertia of the icy regolith. These hemispheres are also susceptible to having a greater presence of dark exogenic material coming from Phoebe's ring or meteoric dust, which are already believed to be a source of contamination of the rings.

E-ring particles mostly hit the trailing sides of Mimas and the leading hemisphere of the satellites orbiting further than Enceladus (Tethys, Dione, and Rhea). The coating produced by these grains has a brightening effect on the surfaces, by the deposition of fresh material and sandblasting of the grains.

Water ice is especially sensitive to photolysis (breakdown by photons), producing species as H_2O_2. Photons have been suggested to play a role in the generation of ozone at Rhea and Dione. The diffusion and recombination of H atoms within the solid ice structure after photolysis can disrupt the crystalline structure, leading to the formation of amorphous ice [38]. Electron irradiation can also induce amorphization in H2O ice, exclusively at temperatures below 60 K [39]. On the other hand, crystallization of amorphous ice can occur under certain conditions. When an amorphous sample is irradiated at temperatures of approximately 13 K by MeV protons or at higher temperatures with a substantial dose of electrons, a phase transition from amorphous to crystalline is observed [40]. Additional triggers for a transition from amorphous to crystalline ice include localized heating resulting from meteoroid impacts and potentially micrometeoroid events [41]. The presence of micrometeorite dust in the outer reaches of the Solar System may contribute to annealing amorphous icy surfaces, with ongoing measurements of the number density of small dust particles by the New Horizons spacecraft. The abundance of amorphous or crystalline ice serves as an indicator of the processes taking place on the surface [13].

Impact craters are one of the main features observed across the different terrains and moons. The process of crater formation involves four major steps represented in Fig. 2.12 [2].

In the initial impact (A), a high-velocity object collides with the planetary surface, excavating material and creating a bowl-shaped depression. Ejected materials, including debris and fragments, are thrown outward from the point of impact. As the impact progresses (B), the bowl-shaped depression evolves into a larger crater shape. The material on the surface around the impact site rebounds upward due to the shockwave generated by the impact, contributing to the formation of the raised rim or edges of the crater. Following the impact (C), ejected materials begin to descend back to the surface, while the

rebounded materials below converge toward the center. This convergence forms a central peak in the middle of the crater, created by the collision and convergence of material. Such craters with a central peak are known as complex craters. In the final structure (D), the crater exhibits distinct features. The ejected material returns to the surface, forming a layer of debris around the crater. A peak stands at the center, resulting from the rebounded and converging material. The edges of the crater may display signs of collapse or slumping, especially if the material is not strongly consolidated.

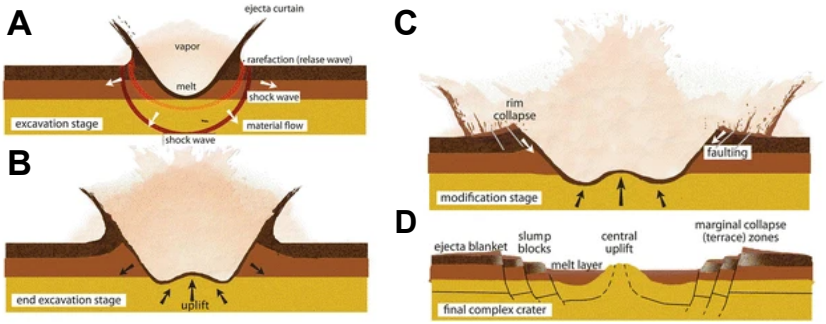

Figure 2.12: Central peak crater formation [2].

The released thermal energy melts the icy regolith, increasing its particle size, while reducing its porosity. Conversely, the vaporized material flash-freezes and precipitates over the surface. These two phenomena associated with an impact alter the surface in opposite directions and it is not clear which one dominates.

3

Spectroscopy and Hapke model

Spectroscopy focuses on the interaction of electromagnetic radiation with matter based on its wavelength. This interaction results in distinctive spectral features that enable the analysis of the composition, physical structure, and electronic properties of the matter in question. This chapter commences with an introductory overview in Section 3.1, outlining the fundamental aspects of spectroscopy and offering an exploration of the spectral characteristics and optical constants of water ice, with a particular focus on their relevance to the study of Saturn's icy moons. Section 3.2 the Hapke photometric model is introduced and explained in depth, setting a solid physical ground upon which to build throughout this work.

3.1. Spectroscopy

The information presented in this section has been extracted from *J. L. Lissauer, Fundamental Planetary Science (2013)* [5]. Electrons bound to an atom can only lay in discrete energy levels. When a photon with the same energy as an energy gap between two electronic states reaches an atom, the electron is excited to a more energetic state, absorbing the photon. The light passing through a gas cloud would excite the atoms that compose the gas, suppressing the wavelengths that match its energy gaps. On the other hand, excited atoms and molecules become de-excited and fall back to their ground state by releasing photons in a cascade process that also involves non-radiative processes.

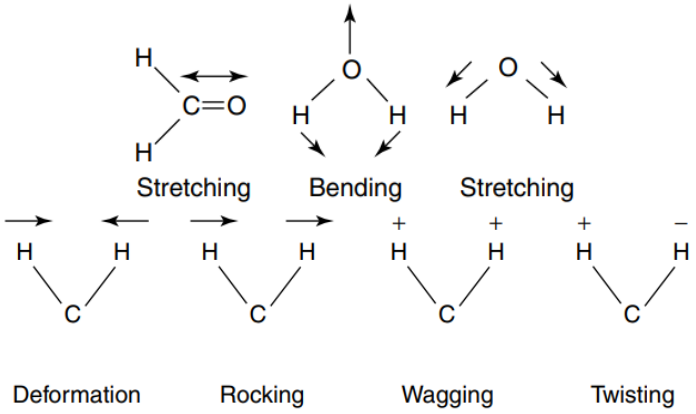

Figure 3.1: Different types of molecular stretching and bending vibrations. Note that the symbols + and - represent out-of-plane vibrations [42].

The distinctive spectral lines found in the absorption or emission spectrum of an atom are linked to its atomic structure. In the case of molecules, the spectrum is not only influenced by their atomic arrangement but also by the molecule's shape and the bonds that bind the atoms together. As a result, the spectrum effectively serves as a unique fingerprint for both atoms and molecules, enabling their identification within an atmosphere or on a surface.

Molecules exhibit a diverse range of vibrational modes, each with its own associated wavelength.

These vibrational excitations predominantly occur in the near-infrared portion of the electromagnetic spectrum. Moreover, molecules can undergo rotational transitions, imprinting their spectral signatures in the far-infrared or microwave regions. Notably, both rotational and vibrational transitions can occur simultaneously, further enriching the spectral complexity of these species.

Molecules can be modeled as a system of interconnected masses, such as springs with varying strengths that correspond to the molecular bonds [42]. In this representation, individual atoms move with respect to one another through processes like bending, stretching, and contracting, as illustrated in Fig. 3.1. It is noteworthy that the depicted stretching can be either symmetric or asymmetric.

The number of absorption bands is constrained by the molecule's degrees of freedom. Various factors, including the Doppler effect in relation to the measuring apparatus, the excited state's lifetime, and temperature-induced broadening due to the thermal Doppler effect and the occupation numbers of excited states, can modify the shape of these bands [42]. Furthermore, whether a molecule exists in a gaseous, liquid, or solid-state significantly influences its spectral profile, as the degrees of freedom of the molecules are constrained. In a solid lattice, vibrational modes manifest as phonons: non-radiative lattice excitations. Fig. 3.2 depicts how various excitations in a CO gas collapse into a single wavelength due to the limitation in movement of the molecules [43].

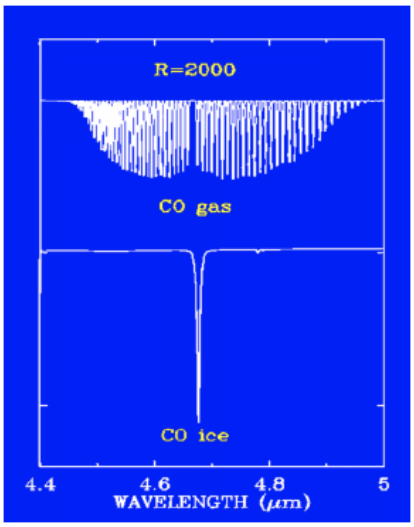

Figure 3.2: Comparison of CO gas spectrum with CO ice [43].

Optical constants

Optical constants comprise how electromagnetic waves interact with specific materials. They are intricately linked to the fundamental properties of the material, and their frequency-dependent behavior offers valuable information into the material's physical characteristics, such as uniformity, resonances, and internal structure [44].

The optical constants are derived from Maxwell's equations and the description of a plane electromagnetic wave. The complex refractive index for a medium can be expressed as

$$\hat{n} = n + ik. \tag{3.1}$$

where n corresponds to the refractive index, k is the extinction coefficient. The introduction of the complex behavior of conductivity and dielectric constants is essential for describing non-isotropic materials, although for isotropic substances, they behave as scalars.

The dielectric constant of a material depends on all the possible interactions between the material and an electromagnetic wave.

The behavior and dependence of optical constants are a direct reflection of a material's internal structure, offering distinctive characteristics for each material. Additionally, a material's absorption characteristics exhibit temperature dependence, attributed to thermal Doppler broadening of absorption bands and changes in the occupation numbers of states due to thermal excitations. Moreover, temperature-induced alterations in a material's density, resulting from thermal expansion, lead to modifications in the refractive index [45].

The optical constants also play a crucial role in describing how much radiation is transmitted, reflected, and absorbed by a medium, in accordance with the Fresnel relations. By measuring the absorbance and transmittance of a thin film, it is possible to directly calculate the complex part of the refractive index, with the real part being deduced through the previously mentioned relations. For a more comprehensive mathematical explanation and presentation of the relevant equations, please refer to [46].

3.1.1. Ice spectroscopy

Depending on the formation conditions, water ice can present itself in a variety of forms according to its molecular structure. A total of twenty crystalline phases of water ice have been identified, and the

search is still ongoing [47].

Amorphous ice, characterized by its lack of structural order, can be synthesized from crystalline ice by subjecting it to high-energy particle irradiation, including ultraviolet (UV) photons, helium ions, and high-energy electrons. When these particles impact a crystalline ice surface, they initiate the generation of various molecular species, including H3O+, OH−, H, OH, and H2. This process disrupts the typically hexagonal and cubic structures present in crystalline ices [40].

Ice phases

The most relevant form of ice on Earth is hexagonal ice, I_h, as the high pressures necessary to create further types of ice are not typically reached. However, other types of ice are believed to be present on Earth. For instance, cubic ice, I_c, has been found at very low temperatures in the higher atmosphere, ice VI, has been spectroscopically identified in diamond inclusions and ice VII has been speculated to be present on cold subduction zones [47].

Most of the ice phases are stable within a range of temperature and pressure, yet some are metastable and their region of stability may overlap with other ice phases [48]. As seen in Fig. 3.3, ice IV and XII lay within the same region of temperature and pressure.

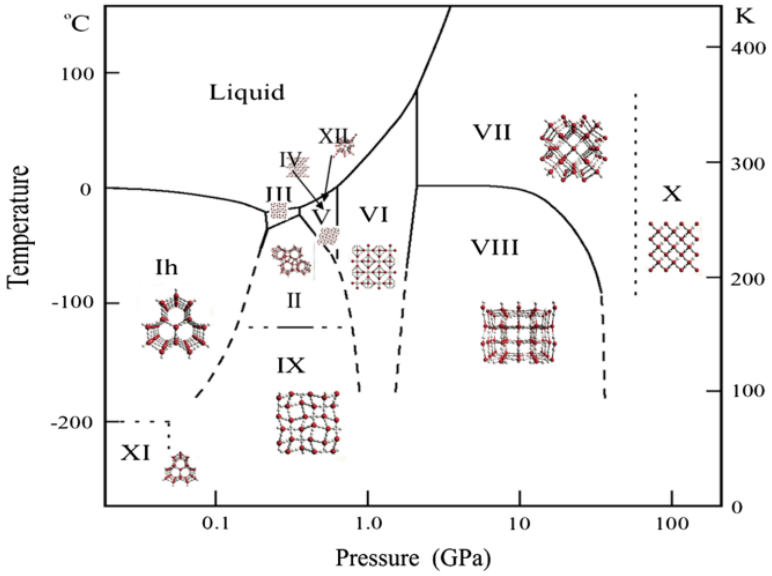

Figure 3.3: Solid-liquid phase diagram of ice. The different lattice structures associated with each water ice type can be appreciated [48].

Fig. 3.3 also shows the molecular structure of the different water ice types, largely studied through neutron-diffraction crystallography. The structure of the water molecules changes to occupy less volume as pressure increases, distorting the angles of the bonds. As pressure increases even further, the distortion of the hydrogen bonds is not sufficient and an interpenetration of the networks occurs, as it is the case for ice VII [48]. As the lattices and arrangement of the molecules change, so does the density. For instance, in the case of ice X the H_2O molecules lay very close to each other, yielding a significant increase in density.

Presently, there exist five distinct varieties of amorphous ice, each defined by its method of formation at the temperature it was created [48]. Another method of characterizing amorphous ices is by their density, which is intricately connected to the pressure under which they were formed, as illustrated in Fig. 3.4 [49].

When subjected to irradiation by photons with sufficient energy to induce molecular dissociation, crystalline ice undergoes a process wherein H_2O molecules are cleaved into H and OH fragments. The resultant H atoms disrupt the crystalline lattice structure via diffusion and recombination within the solid matrix, leading to the ultimate formation of amorphous ice [38]. UV radiation can convert cubic ice into its amorphous counterpart when temperatures fall below 70K. With a photon flux of 10^{12} photons/cm^{2}s^{-1}, crystalline ice within the temperature range of 50 to 70K can transform into an amorphous state within 30 minutes to an hour [50]. At even lower temperatures, around 10K, the conversion process occurs even more rapidly. Similarly, high-energy ion radiation could induce partial amorphiza-

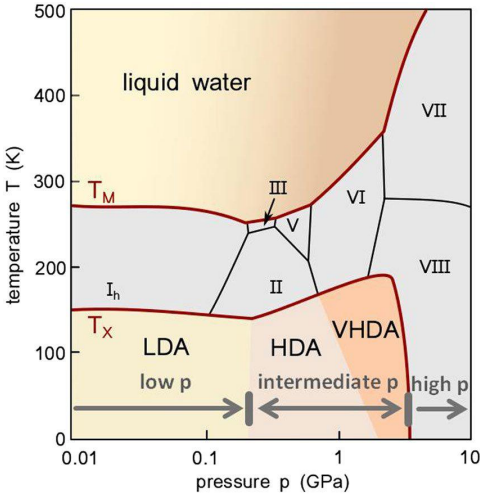

Figure 3.4: Solid-liquid phase diagram of ice including low-density amorphous (LDA), high-density amorphous (HDA), and very high-density amorphous (VHDA) ice. [49].

tion of water ice at temperatures up to 80K, whereas UV radiation initiates this process only when temperatures are below 70K [51].

Crystalline ice can be transformed back into an amorphous state by heating it to temperatures above 110–120K. However, a portion of the ice remains in a ”restrained” amorphous state, characterized by cubic crystallites embedded within an amorphous matrix, until the temperature surpasses the cubic-hexagonal transition point at 188K [52]. Modeling studies have indicated that at 115K, amorphous ice takes less than a year to transition to a cubic state, and at 145K, this transition can occur within just 20 minutes. Observations of comet nuclei have revealed the crystallization of amorphous ice at 137K during a short pulse of warming, and even crystallization at 85K over one million years. Moreover, a phase shift from amorphous to crystalline ice may be produced by localized heating resulting from meteoroid impacts [41].

Optical features of ice

The absorption in ice is dominated by electronic excitations in the UV, molecular vibrations in the near-IR, hindered rotation in the thermal IR, and lattice translations in the far-IR. The absorption coefficient can be measured by transmission in weakly absorbing spectral regions or by reflection in stronger bands [53]. As explained before, the optical constants of a material consist of an imaginary part that accounts for extinction and a real one, the refractive index. Fig. 3.5 shows the real and imaginary parts of ordinary Ih ice at 266 K.

Fig. 3.5 shows how the real index oscillates in a narrow range, while the extinction coefficient can vary up to ten orders of magnitude. Fig. 3.5d shows how the imaginary part drops to 10^{-10}, meaning that ice practically absorbs no radiation in this spectral region. Fig. 3.5e reveals the primary absorption mechanisms of ice Ih in the infrared (IR) spectrum. The fundamental vibrational modes of water molecules are clearly observed in ice, with bending vibrations appearing at 6 μm, as well as both symmetric and antisymmetric bending modes at 3 μm. These frequencies exhibit shifts compared to the absorption spectrum in the gas phase due to the formation of hydrogen bonds that shape the ice's lattice structure. Specifically, the stretching mode shifts to a lower frequency in ice, indicating that the hydrogen bonds within the ice lattice weaken the spring constants of the covalent O-H bonds. On the other hand, the bending mode shifts to a higher frequency, as the formation of hy-

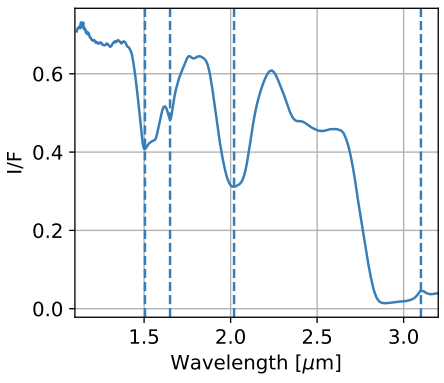

Figure 3.6: Simulated spectrum of crystalline water ice highlighting the main spectral features (1.5, 1.65, 2.0 and 3.1 μm).

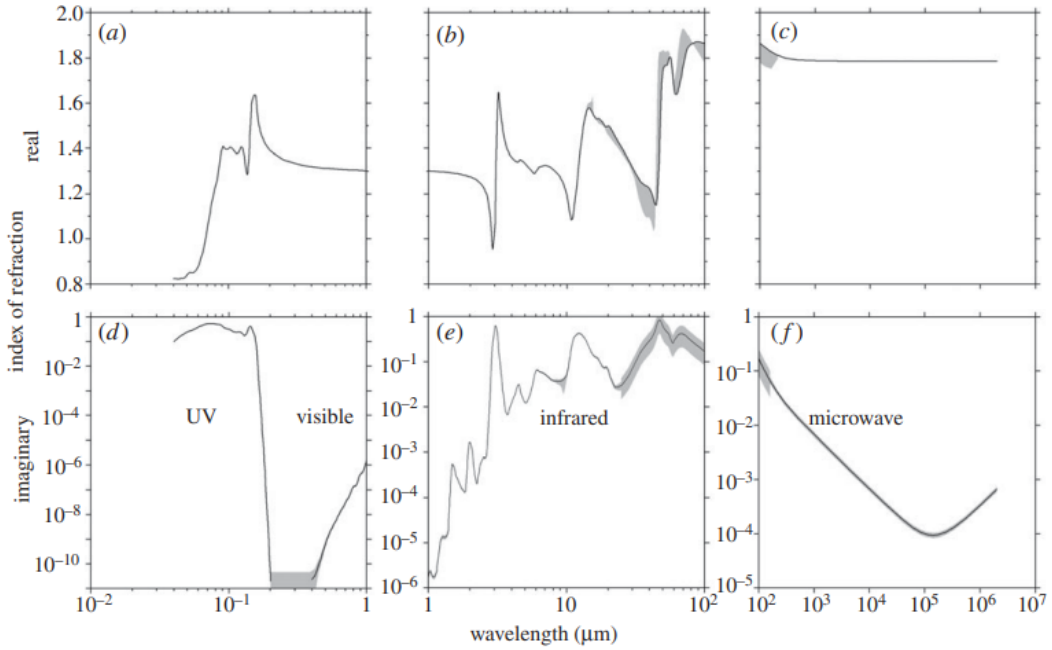

Figure 3.5: Optical constants of ice Ih at 266 K. The shadowed areas represent uncertainty [53].

drogen bonds necessitates the opening of the H-O-H angle, resulting in a stiffer spring constant for bending [53].

Fig. 3.6 shows the distinctive optical features in the near-infrared (NIR) range. They are closely related to the molecular structure of water and the interactions between water molecules in the lattice [54, 53]. At approximately 1.5 μm, water ice exhibits an absorption feature arising from the O-H stretching mode. The position and shape of this absorption band depend on the specific type of ice and its temperature, being sensitive to crystallinity. Another absorption feature emerges at 1.65 μm, originating from the O-H stretching mode as well. This feature is influenced by the structure and hydrogen bond network within the ice lattice. Its intensity depends on the state of ice, going absent for purely amorphous ice, grain size or temperature. Further into the NIR range, at 2 μm, another absorption band also attributed to the O-H stretching vibrations is appreciated. One of the most prominent NIR absorption bands of water ice occurs at 3.1 μm. This feature is associated with the O-H bending vibrations and is particularly significant for its sensitivity to the phase of water ice (crystalline or amorphous) and its molecular environment. This absorption band's position and width can reveal crucial details about the ice's temperature and its structural properties.

3.2. Hapke model

The Hapke model was developed by Bruce Hapke in 1993 and updated in 2002, 2008, and 2012, being fully encapsulated in *B. Hapke, Theory of reflectance and emittance spectroscopy (2012)* [55]. The model consists of a set of parameters related to an airless surface of a celestial body that influences the way light is reflected. Particularly, each parameter allows inferring characteristics of the surface's regolith, such as particle size, porosity, or surface roughness. The parameters influencing the model are explained in the following paragraphs, and an illustration and definition of these parameters are presented in Fig. 3.7 and Table 3.1.

It is useful to define a set of angles as the ones given in Fig. 3.8, where i is the angle between the direction of incidence and the normal vector to the surface, e is the angle between the normal of the surface and the observer and the phase angle g is the angle between the direction of incidence and observer as seen from the surface. The azimuth angle, ψ, is the angle between the direction of incidence and emergence measured on a plane perpendicular to the normal. The phase angle is related to the other three as

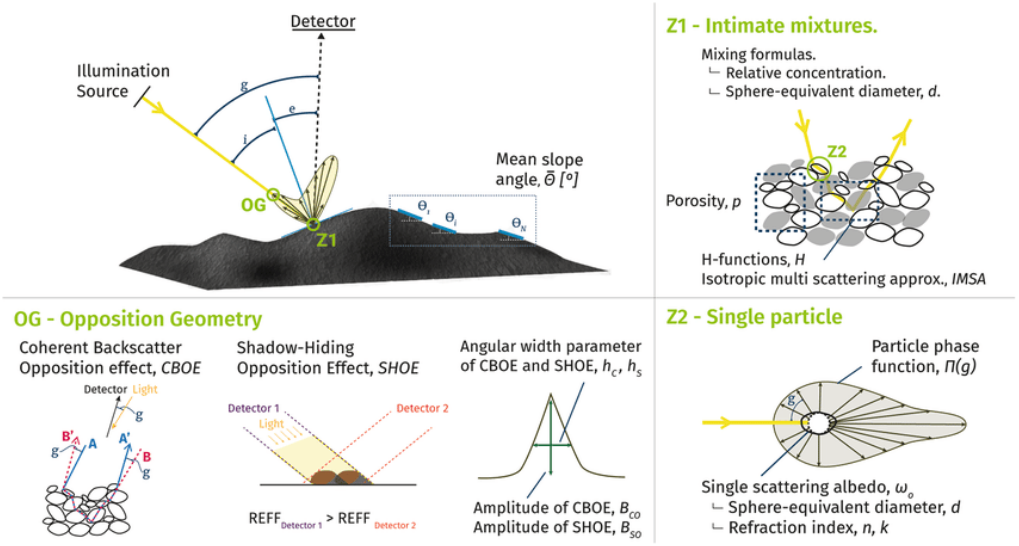

Figure 3.7: Hapke model key parameters that control the reflectance of the surface. The definition of each parameter is presented in Table 3.1 [56].

$$\cos g = \cos e \cos i + \sin e \sin i \cos \psi. \tag{3.2}$$

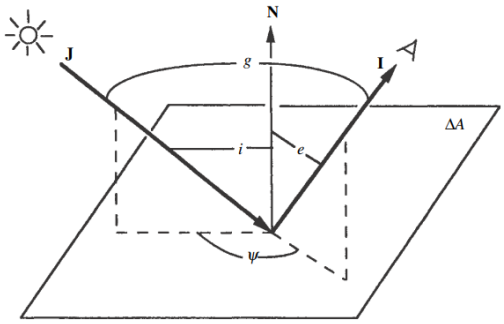

Figure 3.8: Diagram of the relevant angles in reflectance geometry. **J** represents the direction of the incident radiation, **N** is perpendicular to the surface and **I** points towards the observer. The plane containing **J** and **I** is the scattering plane [55].

It is of interest to define a set of values that describe how light is reflected and scattered by a surface. First, the bidirectional reflectance is the fraction of light that is reflected from a surface in the direction of the observer. It is the ratio of the radiance, I, emitted by the surface in the direction of the observer over the solar flux:

$$r = \frac{I}{\pi F}. \tag{3.3}$$

The radiance factor, also known as I/F, compares the reflectance to a Lambertian ideal surface that is illuminated under an incidence of 0 degrees.

$$\frac{I}{F} = \pi r. \tag{3.4}$$

The bidirectional reflectance is given by,

$$r(i,e,g) = K\frac{\bar{\omega}(\lambda)}{4\pi}\frac{\mu_{0e}}{\mu_{0e}+\mu_e}[P(g)B_{SH}(g) + H(\bar{\omega},\mu_{0e})H(\bar{\omega},\mu_e) - 1]S(i,e,\psi,\bar{\theta})B_{CB}(g,\lambda), \tag{3.5}$$

where $\bar{\omega}$ is the single-scattering albedo, μ_{0e} and μ_e are the effective $\cos(i)$ and $\cos(e)$, respectively, adjusted to the surface's roughness, P is the particle phase function, H is the Ambartsumian–Chandrasekhar function that models the effect of multiple scattering by anisotropic scatterers, S is

the shadowing function, B_{CB} represents the coherent back-scattering opposition effect, B_{SH} models the shadow-hiding opposition effect and K is the compaction correction. Each term will be explored individually in this chapter.

Table 3.1: Hapke parameters and their definition. Refer to Fig. 3.7 for illustrations [56].

Parameter	Symbol	Description	Comment
Single scattering albedo	$\bar{\omega}$	Ratio between the total scattered radiation and the total absorbed radiation by one particle	
Single scattering phase function	(b, c)	Angular distribution of the light scattered by one isolated particle	Various formulations can be used. A popular one is the 2-terms Henyey-Greenstein function.
Surface roughness	$\bar{\theta}$	Quantifies the roughness of the surface	The slope distribution is assumed to be isotropic
Porosity	p	The bulk porosity	Introduced in 2008
Shadow hiding opposition effect (SHOE)	B_s, h_s	Opposition effect due to the self-shadowing of particles in the sample. Described by the amplitude and width of the peak	No dependence with wavelength
Coherent backscattering opposition effect (CBOE)	B_c, h_c	Opposition effect due to coherent interactions between photons scattered along the same path in opposite directions. Described by the amplitude and width of the peak	Dependence with wavelength

3.2.1. Single particles: single scattering albedo and phase function

To model the scattering behavior of a medium, it is normally treated as granular, i.e. a collection of individual particles. Depending on the size of the particles relative to the wavelength of the incident radiation, different scattering regimes appear. The regolith of the icy surfaces falls into the Mie and geometric optics regime, where the wavelength is comparable to or much smaller than the diameter of the particles [57].

Single scattering albedo $\bar{\omega}$

In a granular medium, each particle acts as a scattering unit. The possibility of being scattered or absorbed is directly linked to the single scattering albedo, $\bar{\omega}$, that represents the fraction of light that is diffused by a particle:

$$\bar{\omega} = \frac{Q_S}{Q_E} \tag{3.6}$$

Q_S is the volume-average scattering efficiency including diffraction and Q_E is the volume-average extinction coefficient. As planetary surfaces fall in the Mie and geometric optics regime, $Q_E \approx 1$ [55]. In this regime, one can make use of the so-called equivalent-slab approximation, which consists in modeling the particles as slabs. The total fraction of incident light reflected into all directions from the surface of the slab is S_e, while the fraction of internally reflected light is S_i. The light inside the slab is attenuated by Θ, the internal-transmission factor. Then, Q_S is given by

$$Q_S = S_e + (1 - S_e)\frac{1 - S_i}{1 - S_i\Theta}\Theta, \tag{3.7}$$

where the first term is the light that the particle surface has externally scattered. The denominator of the second term represents light multiplicatively internally scattered across the particle, whereas

the numerator of the second term accounts for light transmitted once through the particle. An analytic approximation of S_e that will be used in this work follows

$$S_e = 0.0587 + 0.8543R(0) + 0.0870R(0)^2, \tag{3.8}$$

where

$$R(0) = \frac{(n-1)^2 + k^2}{(n+1)^2 + k^2} \tag{3.9}$$

is the normal Fresnel reflection coefficient, and n and k are the optical constants (refraction and absorption indexes) of the medium. On the other hand, S_i is given by

$$S_i = 1 - \frac{1}{n^2}[0.9413 - 0.8543R(0) - 0.0870R(0)^2] \tag{3.10}$$

The internal transmission factor is given by the so-called exponential model,

$$\Theta = \exp\left(-\sqrt{\alpha(\alpha+s)}\,\langle D\rangle\right) \tag{3.11}$$

where

$$\langle D\rangle = \frac{2}{3}\left[n^2 - \frac{1}{n}\left(n^2-1\right)^{\frac{3}{2}}\right] D \tag{3.12}$$

represent the average distance traveled by all rays during a single transit in the particle and α is the absorption coefficient, given by

$$\alpha = \frac{4\pi k}{\lambda}. \tag{3.13}$$

Phase function $P(g)$

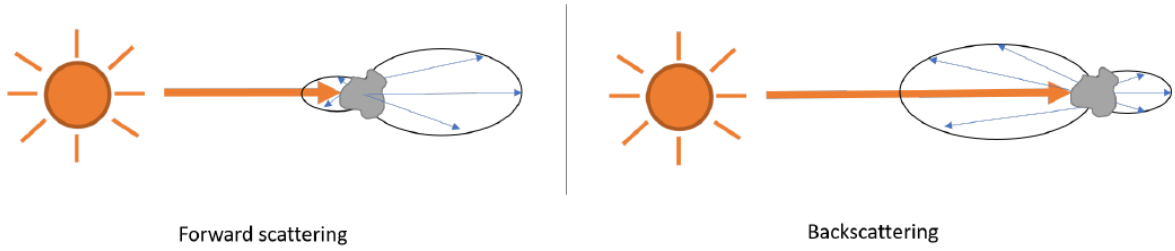

Figure 3.9: Diagram of forward and backscattering lobes [57].

In particle photometry, the Henyey-Greenstein functions are widely used to describe in which direction an incoming photon is scattered [58]. A 2-term function is the most common one in literature and is given by,

$$P(g) = \frac{1-c}{2}\frac{1-b^2}{(1+2b\cos g + b^2)^{3/2}} + \frac{1+c}{2}\frac{1-b^2}{(1-2b\cos g + b^2)^{3/2}}, \tag{3.14}$$

b is the width parameter that can take values between $0 \leq b < 1$ and c represents the relative strengths of the scattering lobes and backscattering fraction. Fig. 3.9 shows the difference between forward and backscattering by a particle and the scattering lobes and Fig. 3.10 shows the physical meaning of both parameters. How prone a particle is to forward or backscattering is given by c, a negative value indicates that forward scattering is dominant while positive values indicate that backscattering is dominant [59].

From experimental studies [60], it has been found that b and c tend to follow the so-called hockey stick relation,

$$c = 3.29\exp\left(-17.4b^2\right) - 0.908. \tag{3.15}$$

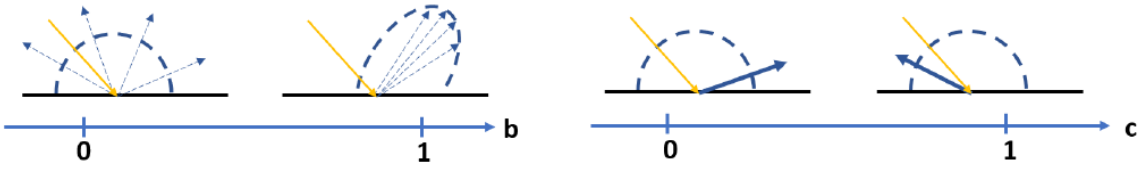

Figure 3.10: Physical meaning of the parameters b and c. Note that the backscattering fraction presented in this diagram follows another formulation of Eq. 3.14; yet, it conveys the same information [57].

Fig. 3.11b shows the effect that changing b has on the phase function, while c changes according to the hockey stick relation (Fig. 3.11a). The greater b, the stronger front and backscattering are while diffusion in other directions is suppressed. As shown in Fig. 3.11a, one can already extract information about the surface from the values of b and c, as different terrains and materials disperse lights in different ways. Increasing b reduces the amount of reflected radiation across the entire spectrum, as shown in Fig. 3.12.

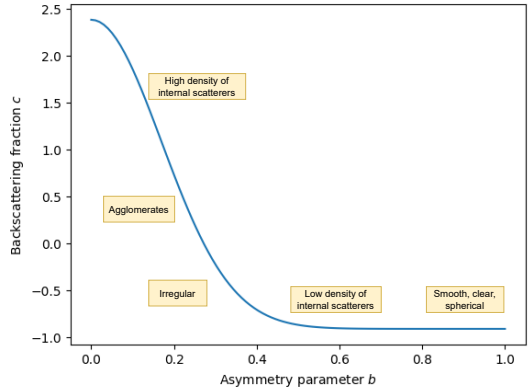

(a) Hockey stick relation as given by Eq. 3.15, adapted from [57].

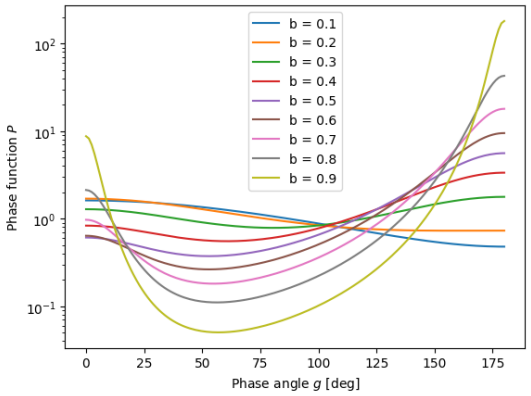

(b) Phase function for different asymmetry parameters according to Eq. 3.14, following a two-term Henyey-Greenstein function. The backscattering fraction, c, has been calculated following Eq. 3.15.

Figure 3.11: Hockey stick and phase function.

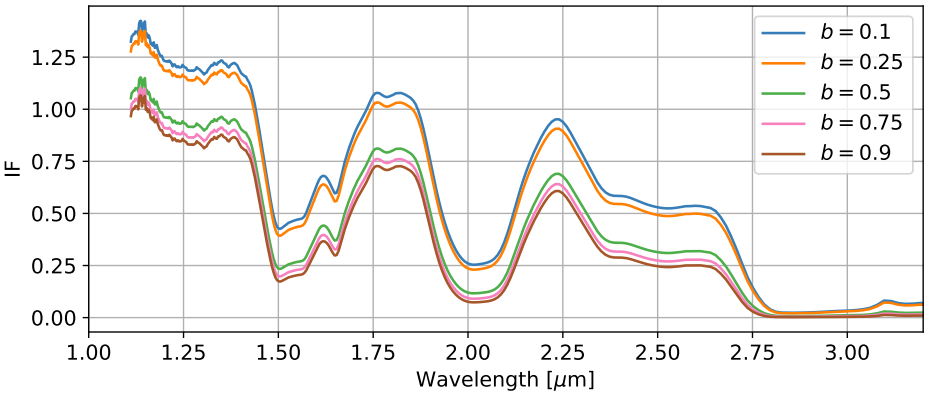

Figure 3.12: Simulated reflectance spectra crystalline water ice for different phase function asymmetry parameters. Hapke parameters are $e = g = 30°$, $i = 0°$, $\phi = 0.5$, $D = 70$ microns, $\bar{\theta} = 30°$ and the optical constants are taken from Mastrapa (2008 & 2009) at 120 K [61, 54].

3.2.2. Interaction with a medium: grain size, filling factor, surface roughness, and multiple scattering

Grain size, D

The grain size represents the mean particle diameter of the surface regolith. Particle size has a direct effect on the single scattering albedo, as shown in Eq. 3.12. Fig. 3.13 represents the effect of varying mean particle diameters on the reflectance spectra of crystalline ice in the spectral range of Cassini's VIMS instrument. One can appreciate how larger grain sizes yield a smaller radiance factor while increasing how pronounced the peaks and valleys are. Note that the position of the main spectral features is not affected by grain size, but rather their intensities. Also, particle size affects how smooth a surface is: larger particles make rougher surfaces. The smoother the surface, the more light is reflected, generally increasing a body's albedo. On the other hand, larger particles absorb more energy, as the change in surface texture helps trap more photons.

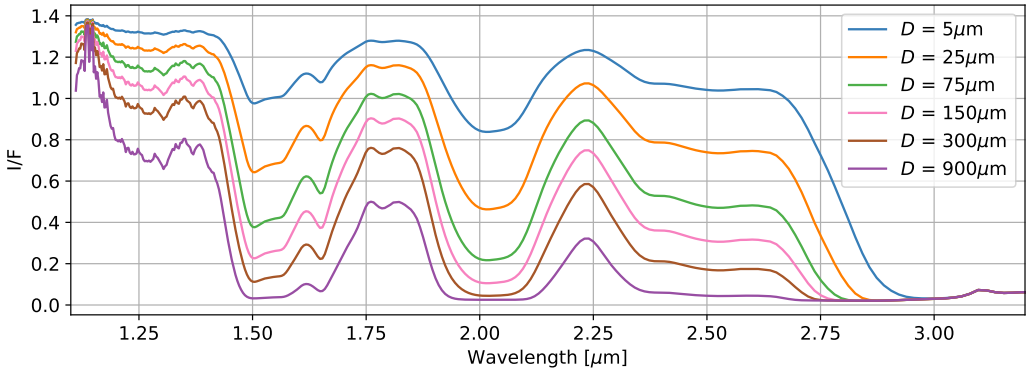

Figure 3.13: Simulated spectrum of crystalline ice at 120 K for different grain sizes. Hapke parameters are $e = g = 30°$, $i = 0°$, $\phi = 0.5$, $b = 0.25$ and $\bar{\theta} = 30°$.

Filling factor, ϕ, and compaction correction, K

The filling factor, ϕ, equals $1-p$, being p the porosity of the regolith. It is the volume fraction occupied by material and ranges between zero (absence of material) and one (no space between grains). As shown in Fig. 3.14, reflected light increases with increasing ϕ, until 0.752, after which the material becomes opaque [55]. For these values, the angular width of the shadow-hiding opposition effect diverges; then, this study will only cover values in the range of $0 \leq \phi < 0.75$.

The light reflected from the upper layers of the surface regolith experiences the effects of macro-porosity: the amount of space taken by the pores in the ice that are much larger than the grains. For that reason, Eq. 3.5 includes the compaction, K, that accounts for this phenomenon. It is related to the filling factor and is given by,

$$K = -\frac{\ln\left(1 - 1.209\phi^{2/3}\right)}{1.209\phi^{2/3}} \tag{3.16}$$

Surface roughness, $\bar{\theta}$

The macroscopic roughness, $\bar{\theta}$ represents the mean local slope of the analyzed terrain, shown in Fig. 3.7. It is the average over all distances on the surface according to the resolution of the detector and the physics of the radiative-transfer equation. The effect of this parameter is registered by the shadowing function $S(i, e, g, \bar{\theta})$ [55]. To define the effect of this function, some auxiliary ones are introduced,

$$\chi(\bar{\theta}) = \frac{1}{\sqrt{1 + \pi \tan^2(\bar{\theta})}}$$

$$E_1(x) = \exp\left(-\frac{2}{\pi \tan(\bar{\theta}) \tan(x)}\right)$$

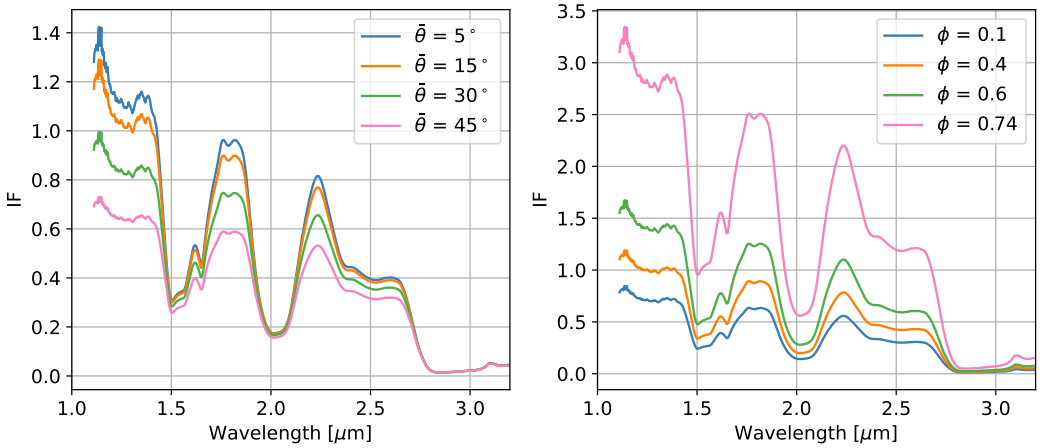

Figure 3.14: Effects of macroscopic texture parameters in radiance factor for different values of $\bar{\theta}$ (left) and ϕ (right).

$$E_2(x) = \exp\left(-\frac{2}{\pi \tan^2(\bar{\theta}) \tan^2(x)}\right)$$

$$f(\psi) = \exp(-2\tan(\frac{\psi}{2}))$$

$$\eta(y) = \chi(\bar{\theta})\left(\cos(y) + \sin(y)\tan(\bar{\theta})\frac{E_2(y)}{2 - E_1(y)}\right)$$

Then, two different formulations are given:

- if $i \leq e$:

$$\mu_{0e}(i,e,\psi) = \cos(i_e) \simeq \chi(\bar{\theta}_p)\left(\cos(i) + \sin(i)\tan(\bar{\theta}_p)\frac{\cos(\psi)E_2(e) - \sin^2(\psi/2)E_2(i)}{2 - E_1(e) - (\psi/\pi)E_1(i)}\right) \tag{3.17}$$

$$\mu_e(i,e,\psi) = \cos(e_e) \simeq \chi(\bar{\theta}_p)\left(\cos(e) + \sin(e)\tan(\bar{\theta}_p)\frac{E_2(e) + \sin^2(\psi/2)E_2(i)}{2 - E_1(e) - (\psi/\pi)E_1(i)}\right) \tag{3.18}$$

$$S(i,e,\psi) \simeq \frac{\mu_e}{\eta(e)}\frac{\mu_0}{\eta(i)}\frac{\chi(\bar{\theta}_p)}{1 - f(\psi) + f(\psi)\chi(\bar{\theta}_p)[\mu_0/\eta(i)]} \tag{3.19}$$

- if $e \leq i$:

$$\mu_{0e}(i,e,\psi) \simeq \chi(\bar{\theta})\left[\cos i + \sin i \tan\bar{\theta}\frac{E_2(i) - \sin^2(\psi/2)E_2(e)}{2 - E_1(i) - (\psi/\pi)E_1(e)}\right] \tag{3.20}$$

$$\mu_e(i,e,\psi) \simeq \chi(\bar{\theta})\left[\cos e + \sin e \tan\bar{\theta}\frac{\cos\psi E_2(i) + \sin^2(\psi/2)E_2(e)}{2 - E_1(i) - (\psi/\pi)E_1(e)}\right] \tag{3.21}$$

$$S(i,e,\psi) \simeq \frac{\mu_e}{\eta(e)}\frac{\mu_0}{\eta(i)}\frac{\chi(\bar{\theta})}{1 - f(\psi) + f(\psi)\chi(\bar{\theta})[\mu_0/\eta_e(e)]}. \tag{3.22}$$

Surface roughness varies ranges between $0 < \bar{\theta} \leq 45°$ and the effect it has in the I/F is shown in Fig. 3.14. The lower the surface roughness, the smoother the surface and the more light is reflected. Greater values of $\bar{\theta}$ entail a more pronounced steepness in the surface, favoring backscattering. When

reaches a surface with an angle, part of the radiation is reflected in a direction that collides again with the surface, yielding an overall decrease in the amount of reflected radiation. However, experiments show that surface roughness encapsulates the effects of particle-level structures to mm-level and that larger structures only represent a minor contribution to $\bar{\theta}$ [62].

The effects of surface roughness on reflectance spectra are convolved with the single-particle phase function. Among the Saturnian satellites, $\bar{\theta}$ ranges between $6°$ and $33°$, with a mean of $22° \pm 10°$ [1].

Multiple scattering function, H

The phase function shown in Eq. 3.14 represents the so-called single scattering, light that is immediately reflected from a granular medium. As light penetrates the medium, it is repeatedly scattered by several particles before being observed. This is called multiple scattering and the greater its effect the more isotropically distributed the direction of the light becomes [57].

The multiple scattering function is defined by

$$M(\mu_0, \mu, g) = H(\mu_0)H(\mu) - 1 \tag{3.23}$$

where the H-function can be approximated within a 1% of the exact solution [55]

$$H(x) \approx \frac{1}{1 - \bar{\omega}x\left[r_0 + \frac{1-2r_0x}{2}\ln\left(\frac{1+x}{x}\right)\right]} \tag{3.24}$$

where $r_0 = (1-\gamma)/(1+\gamma)$ and $\gamma = \sqrt{1-\bar{\omega}}$. As shown in Eq. 3.23, x can be either μ_0 or μ.

3.2.3. Opposition effects: CBOE and SHOE

Opposition effects describe the brightness growth observed at very small phase angles and it follows from two phenomena, the *Coherent Backscattering Opposition Effect* (CBOE) and the *Shadow-Hiding Opposition Effect* (SHOE).

Coherent Backscattering Opposition Effect (CBOE)

When radiation is scattered by an irregular medium, it tends to scatter in all directions. However, when the scattered light is measured as a function of the scattering angle, a peak or an increase in intensity is observed at the angle opposite to the incident direction. This phenomenon observed at very low phase angles is the *Coherent Backscattering Opposition Effect* (CBOE).

This effect arises due to interference between the multiple scattered waves. As shown in Fig. 3.16a, the waves that travel through different paths and scatter back towards the observer can interfere constructively or destructively, resulting in the observed peak in the backward direction [55].

Hapke (2002) [63] introduces the formulation of this effect, given by the function

$$B_{CB}(g) = 1 + B_{C0}B_C(g) \tag{3.25}$$

where B_{C0} is the amplitude of the CBOE and is constrained to be smaller than 1,

$$B_C(g) = \frac{1 + \frac{1-\exp\left(-\tanh\left(g/2\right)/h_C\right)}{\tan\left(g/2\right)/h_C}}{2\left[1 + \tan\left(g/2\right)/h_C\right]^2} \tag{3.26}$$

$$h_C = \frac{\lambda}{4\pi\Lambda}, \tag{3.27}$$

λ is the wavelength and Λ is the transport mean free path, which is the average distance a photon travels within a medium before its direction is randomized.

CBOE peaks at opposition and decreases rapidly. Fig. 3.15 shows how for values of $g \geq 3°$ this effect can be neglected [57].

Shadow-Hiding Opposition Effect (SHOE)

Shadow Hiding Opposition Effect (SHOE) is the main source of the opposition effect in a granular medium. Each particle is partially hidden by the shadows of other particles. When the phase angle becomes small enough, the shadows become hidden from the observer resulting in a general increase

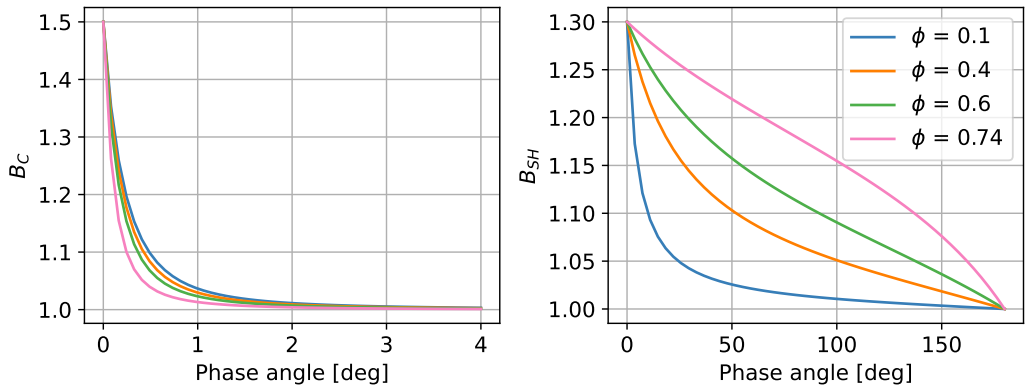

Figure 3.15: Magnitude of CBOE (at 2 μm with $B_{C0} = 0.5$ and $\Lambda = 33$ μm, left) and SHOE ($B_{S0} = 0.3$, right) for different phase angles and filling factors.

in brightness [57]. As represented by Fig. 3.16b, a larger phase angle means that part of the radiation that reaches one side of the particles does not have a suitable geometry to reach the observer. When the phase angle decreases, more illuminated regions become visible, increasing the overall brightness.

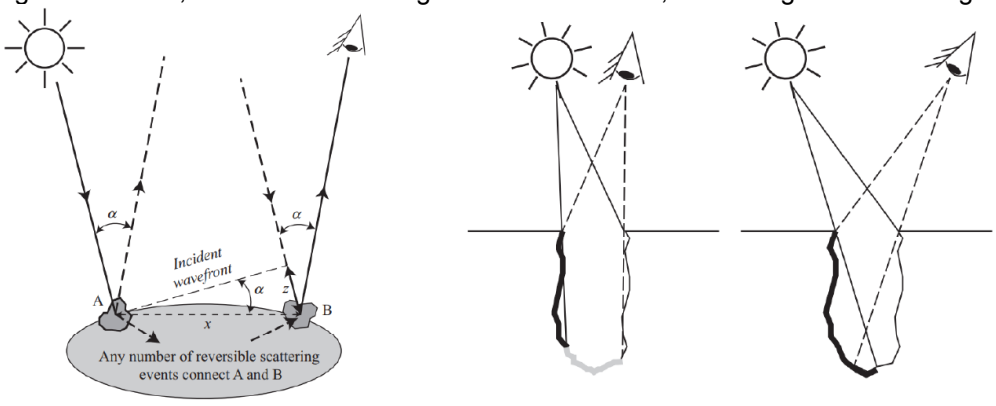

(a) Illustration of the CBOE [64].

(b) Illustration of the SHOE [64].

Figure 3.16: Opposition effect depiction.

The formulation of the SHOE can be found in Hapke (2012) [55],

$$B_{SH}(g) = 1 + B_{S0} B_S(g) \tag{3.28}$$

where B_{S0} is the amplitude of the SHOE, defined as

$$B_{S0} \approx \frac{S(0)}{\bar{\omega} P(0)} \tag{3.29}$$

where $S(0)$ is the fraction of incident light scattered and is given by the Fresnel reflection coefficient at normal incidence (Eq. 3.9). Notice that both $\bar{\omega}$ and $S(0)$ depend on wavelength. On the other hand,

$$B_S(g) = \frac{1}{1 + \tan(g/2)/h_S} \tag{3.30}$$

where h_S is the angular width of the SHOE and depends on the porosity parameter,

$$h_S = \frac{3}{8} K\phi = -\frac{3}{8} \frac{\phi \ln\left(1 - 1.209\phi^{2/3}\right)}{1.209\phi^{2/3}}. \tag{3.31}$$

The SHOE phenomenon is significant along a wider range of phase angles than CBOE. Fig. 3.15 shows that depending on the filling factor, it can be relevant up to phase angles of $100°$.

3.2.4. Intimate mixing formulation

When different particles with different compositions are present, they are referred to as *intimately mixed*. This homogeneous mixture can be modeled as a weighted average of the single scattering albedos of the different types of grains [65],

$$\bar{\omega}_{mix} = \left(\sum_j \frac{m_j \bar{\omega}_j}{\rho_j D_j} \right) / \left(\sum_j \frac{m_j}{\rho_j D_j} \right) \tag{3.32}$$

m_j is the mass fraction of the j-th material, ρ_j its density and D_j its particle diameter.

The SHOE terms are also affected by the presence of extra particles. The averaged B_{S0} coefficient is defined by,

$$B_{S0} = \left(\sum_j \frac{m_j S_j(0)}{\rho_j D_j} \right) / \left(\sum_j \frac{m_j \bar{\omega}_j P(0)}{\rho_j D_j} \right). \tag{3.33}$$

These two values are plugged in Eq. 3.5 to account for extra mixed material. This intimate mixing formulation will be used to study the crystallinity of the icy moons' regolith.

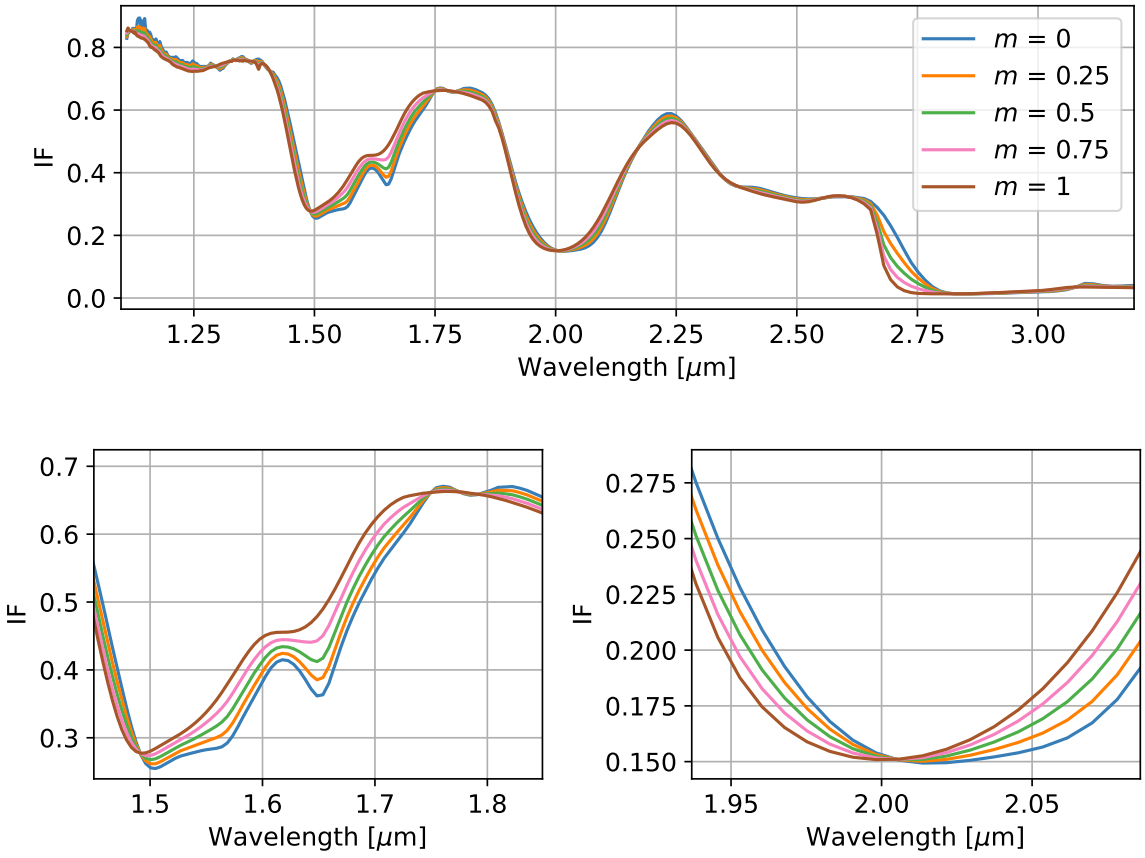

Figure 3.17: Simulated reflectance spectra of an intimate mix of crystalline and amorphous water ice for different mass fractions of amorphous ice. Hapke parameters are $e = g = 30°$, $i = 0°$, $\phi = 0.5$, $D = 70$ microns and close-up on the 1.65- and 2-micron features. Optical constants are taken from Mastrapa (2008 & 2009) at 120 K [61, 54].

Fig. 3.17 shows the variation in some of the features of water ice as the mass fraction of amorphous ice changes. Two relevant features for this work are also presented: the 1.65 and the 2-micron features. The 1.65-micron absorbance peak is present for pure crystalline ice and is completely absent for amorphous ice, as seen in Fig. 3.17 the intimate mixing model shows how a homogeneous mixture of amorphous and crystalline water ice falls in the middle of both extreme cases. On the other hand, the position of the 2-micron absorption feature shifts between 2.00 for amorphous ice and 2.035 μm

for pure crystalline ice. According to *G. Fillachione, et al. (2010)* [66], the 2-micron absorbance feature varies between 2 and 2.05 μm depending on the state of the water ice; yet, such amplitude is not appreciated in Mastrapa's optical constant data.

4

Data acquisition

This section delves into the different data that is used throughout this work. First, the optical constants necessary for the Hapke model are extracted from Mastrapa (2008 & 2009) [61, 54] and the data is presented in Section 4.1. Then, the data measured by Cassini's VIMS and a general description of the instrument are given in Section 4.2, together with a set of selection rules for the pixels. Finally, Section 4.3 shows the theory behind the fit performed to obtain the surface characteristics from the lab data and icy moons' surfaces and their corresponding uncertainties.

4.1. Optical constants

In Section 3.2 Hapke model was defined. The single scattering albedo ($\bar{\omega}$) depends on the Fresnel reflection coefficient, given by Eq. 3.9, that is calculated by using the optical constants of water ice. The fresnel reflection coefficient is then used to calculate the fraction of incident light that is reflected outwards (Eq. 3.8) and inwards (Eq. 3.10), used in the final value of $\bar{\omega}$ (Eqs. 3.7 and 3.6). They were measured by Mastrapa (2008 & 2009)[1] in the region between 1.1 to 22 μm [61, 54]. They utilized thin film samples to minimize contamination and scattering of the infrared spectrum, and the ice samples were deposited in a vacuum. A thin film approximation was utilized based solely on sample thickness, treating them as slabs. Given that the grain size of the samples remained undetermined, they were assumed to possess small grain sizes, and potential variations in grain size were neglected as they did not directly influence the calculation of optical constants.

The sample was formed via vapor deposition of H_2O, while concurrently monitoring the infrared spectrum and sample thickness. Crystalline samples were formed at 150 K, and amorphous samples were generated at temperatures below 100 K. The average thickness for optical constants determination was constrained to fall between 20 and 50 μm, within which the 3-μm H_2O fundamental was saturated, and the 1-μm band was not observed. Subsequently, the experiment involved heating the samples at a rate of approximately 1 K/min while recording spectra at 10 K intervals within the range of 20 to 150 K, ensuring spectral stability and consistency. The samples were left to stabilize once the target temperature was reached. The spectra are measured in transmittance, and by applying the formulas of the absorption coefficient of a plane-parallel absorbing film and the Kramers-Kronig relation, n, and k are calculated for each wavelength.

The main absorption bands of water ice are present in this region and fall under the wavelength region of Cassini's VIMS. They are located at 1.04, 1.25, 1.5, 1.65, 2.0, and 3.1 microns. The imaginary part of the optical constants, k, explains the strong absorption features. When the absorption coefficient is zero, the material is transparent at that particular wavelength.

Fig. 4.1a and Fig. 4.1b show the variation of the optical constants in the wavelength range of Cassini's VIMS. The optical constants vary depending on the temperature and ice morphology. Such variation appears in the simulated reflectance spectra (Fig. 4.2a and Fig. 4.2b), and can be used to infer both the crystallinity and temperature of a given water ice spectrum. The main differences due to crystallinity appear at the wavelengths of the Fresnel peak (3.1 microns) and the reflectance peak

[1] Data available in `https://iopscience.iop.org/article/10.1088/0004-637X/701/2/1347#references`

at 1.6 microns. Temperature produces a spectral shift on the continuum peak at 3.6 microns, which G. Filachione et al. (2016) used to map the daytime temperatures of the icy moons of Saturn [15].

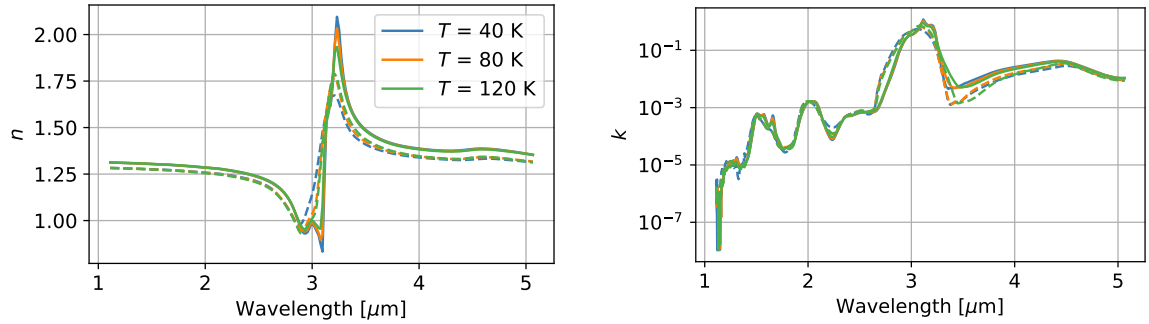

(a) Refractive index n of crystalline and amorphous ice at different temperatures.

(b) Extinction coefficient k of crystalline and amorphous ice at different temperatures.

Figure 4.1: Optical constants, index of refraction n and extinction coefficient of water ice for crystalline (solid) and amorphous (dashed) at different temperatures [61, 54].

R. N. Clark, et al. (2012) [67] found that Hapke-modeled spectra with Mastrapa's optical constants did not match laboratory reflectance data in the 3.2- to 5-μm range. However, they show good agreement with experimental measurements in the 1.1-3.2 microns region. Consequently, the application of Mastrapa's optical constants is confined to this spectral range.

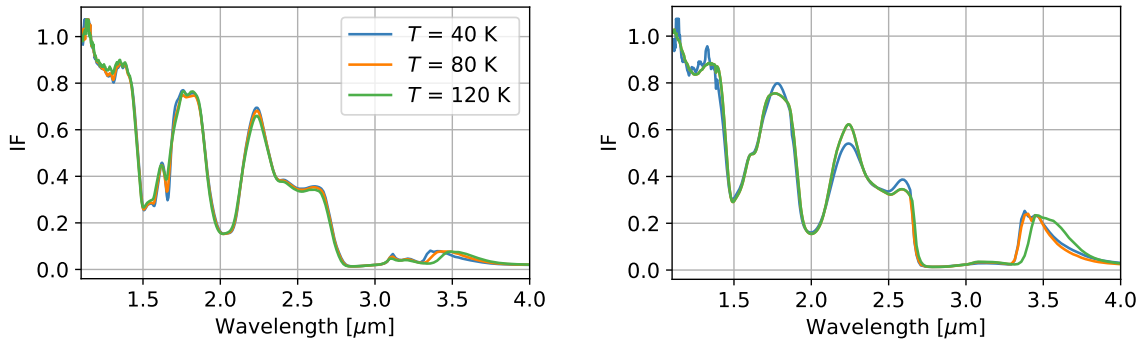

(a) Simulated reflectance spectra of crystalline water ice at different temperatures.

(b) Simulated reflectance spectra of amorphous water ice at different temperatures.

Figure 4.2: Reflectance spectra of water ice for crystalline and amorphous ice at different temperatures with $th\bar{e}ta = 20°$, $\phi = 0.15$, $b = 0.25$, $D = 60$ microns and $e = 30°$, $i = 0°$ and $g = 30°$ [61, 54].

4.2. Cassini data

The data used in this study has been retrieved from observations performed with Cassini's VIMS instrument [68, 69]. VIMS is an imaging spectrometer, composed of two channels: visible (V) and infrared (IR). Under nominal mode, the VIMS-V channel covers the wavelength region 0.35-1.05 μm in 96 spectral channels, with a maximum spectral resolution of 1.46 nm, a spatial resolution of 167 μrad, and a 3.6-degree field of view. VIMS-V is composed of two modules, the optical head and the electronics assembly. Likewise, the optical head (shown in Fig. 4.3a) has two units: a scanning telescope (front in the diagram) and a grating spectrometer (back), joined at the telescope focal plane where the entrance slit is located. The spectrometer is held by an optical bench, where the telescope mirrors are mounted.

Incoming radiation to the VIMS-V channel follows the path described in Fig. 4.3b: it is collected by the scanning telescope (f/3.2) and then focused onto the spectrometer slit. The image formed at the slit is dispersed by a diffraction grating and imaged onto the CCD matrix, where each pixel column records a monochromatic image, registering both spatial and spectral information. The sampling time for this channel totals 80 ms. Likewise, the incoming light to the VIMS-IR is collected by a 23-cm diameter Ritchey Cretien telescope (f/3.5). A secondary mirror allows the scanning in two directions, for a 64x64 mrad scene. A grating spectrometer, using an f/3.5 Dahl-Kirkham collimator, disperses the radiation

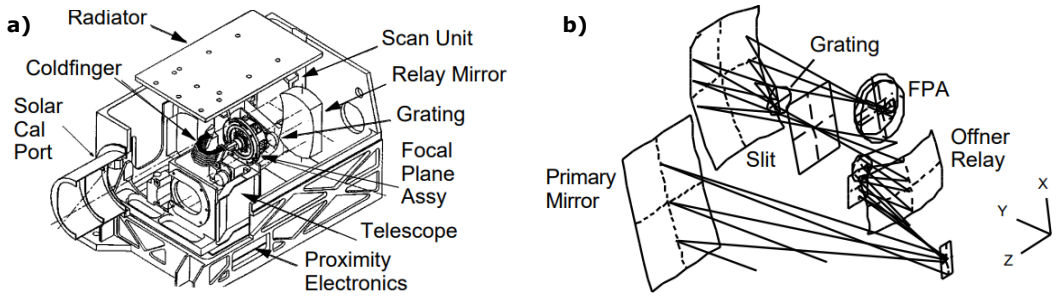

Figure 4.3: VIMS-V channel cutaway diagram (left) and optical ray trace diagram of the optical head (right) [70]. FPA stands for Focal Plane Assembly. The coldfinger is actively cooled to maintain the sensing elements at the required temperatures.

into the 256 channels of the InSb detector.

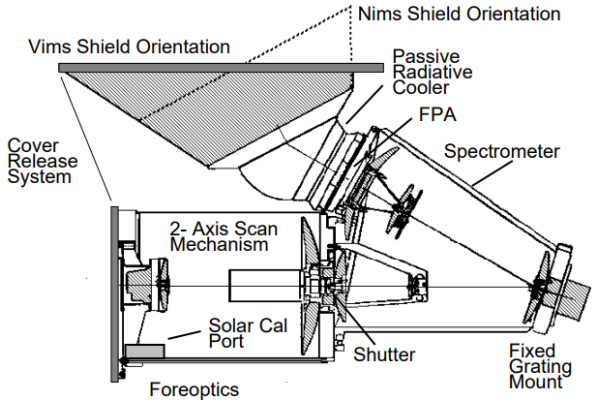

Figure 4.4: VIMS-IR channel diagram [70]. NIMS is a previous instrument from which the VIMS-IR channel was designed; hence, the modifications are noted in the diagram.

On the other hand, the VIMS-IR channel operates in the 0.85-5.1 μm region in 256 channels at a spectral resolution of 0.0166 μm, an angular resolution of 0.5 μrad and a 3.6-degree field of view. Fig. 4.4 shows the major VIMS-IR along with the light paths. The diagram shows the cover, which is activated on command to block light from entering the spectrometer to record the combined dark current and thermal background associated with a given measurement. Thermal isolation is particularly relevant for the IR channel because of the blackbody radiation of the spectrometer. The VIMS-V channel uses a push-broom scanning while the VIMS-IR uses a whisk-broom scanning and both cover an array of 64 x 64 pixel field of view. The push-broom scanning consists of covering the entirety of the pixel matrix by illuminating full rows, one after the other. On the other hand, a whisk-broom scanning covers the entire matrix by illuminating the pixels from left to right, top to bottom.

When VIMS took an image of the surface of an icy moon, it was stored in cubes. Each cube is composed of pixels, covering its entire field of view, and each one has an associated spectrum.

4.2.1. VIMS data cubes

The data acquired during the mission has been archived by NASA's Jet Propulsion Laboratory (JPL) within the Planetary Data System collection. The raw Cassini data is publicly accessible[2].

Inside this database, the unprocessed data from the Cassini mission, including VIMS data, is stored. Prior to its use in the present study, this data needs to be calibrated. This calibration procedure categorizes the data into two distinct sections: the visible and infrared segments. Subsequently, the digital count values associated with each pixel undergo transformation into physical radiometric intensity values (referred to as I/F). Furthermore, the calibration process effectively eliminates any sporadic pixel noise within the datasets.

The VIMS cubes data extracted from the Cassini mission, are presented by the Planetology and Geodynamics' team (LPG) at Nantes University[3]. The LPG VIMS data portal offers previews of the

[2]More info: `https://pds-imaging.jpl.nasa.gov/`
[3]More info: `https://vims.univ-nantes.fr/`

VIMS cubes, which can be directly downloaded from their website. These downloaded data cubes facilitate the extraction of valuable information such as spectra, coordinates on the icy moons' surfaces, observation angles, and resolution specific to user-defined locations. Each cube encapsulates an observation of the surface, comprising numerous individual pixels. The resolution of a pixel is determined as the diagonal distance from one corner to the opposite corner, and the center of each pixel, signifying the latitude and longitude, corresponds to the intersection point between lines connecting the opposing corners.

To enable the extraction of data from the downloaded cubes, LPG made available a Jupyter notebook[4], which gives examples of the main built-in functionalities of the PyVIMS library for treating cubes spectra in Python. A representation of a cube taken at VIMS' high-resolution mode is found in Fig. 4.5a. The spectra of three pixels at different locations are shown in Fig. 4.5b. Data taken from VIMS is generally noisier at wavelengths greater than 3 microns, due to a lower reflectance of the icy moons in this spectral range and lower instrumental sensitivity [71]. Besides, pixels from the same cube may have very different illumination conditions, then selection criteria may be applied at a pixel level.

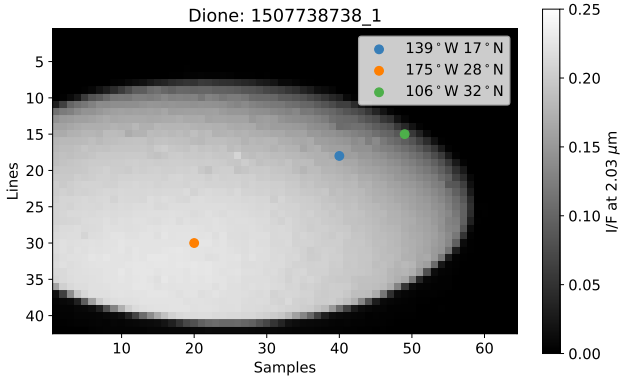

(a) Dione's cube 1507738738_1. Color represents the I/F at 2.03 microns.

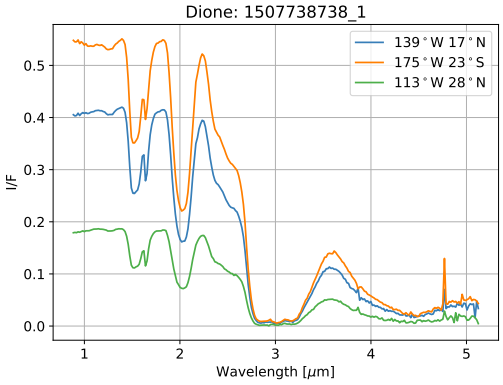

(b) Spectra of the selected pixels in Dione's cube 1507738738_1 taken during flyby D1.

Figure 4.5: Cube depiction and spectra of selected pixels of Dione's cube 1507738738_1.

4.2.2. 1-micron dip

A recurring pattern in the cubes found within various regions is the prominent dip observed at lower wavelengths. There is no discernible correlation between the pixel's location and the origin of this dip. This feature can be attributed to the raw data collected by the VIMS instrument, which is quantified in terms of data numbers (DN), representing the detector's counts. When the DN value exceeds 3500 counts, the data becomes saturated, leading to the dip in readings occurring around the 1-μm range [14]. Consequently, this saturation affects the spectra in the specified region, rendering them unusable. Fig. 4.6a illustrates a cube in which the 1-micron feature takes place, with its consequent spectra in Fig. 4.6b.

4.2.3. Selection rules for pixels

For each one of the cubes, a set of selection rules is developed so the results given by the fit are reliable and within its assumptions. They are the following:

- **Pixel is not at the limb**: the pixels at the limb of a moon's cube image are greatly distorted and can give misleading spectra that do not reflect the actual characteristics of the terrain.
- **Pixel area**: the area of the pixels should be below a $(R/7)^2$, being R the radius of the observed icy moon, for a greater resolution of the terrain.
- **Illumination conditions**: $e, i, g < 90°$ and $g > 5°$ to avoid great opposition surge effects.
- **Mean intensity**: the mean I/F of the spectrum should lay above 0.025. Spectra with low intensity are susceptible to greater errors and hinder the convergence of the fit.

[4]More info: `https://github.com/seignovert/pyvims/blob/main/notebooks/pyvims.ipynb`

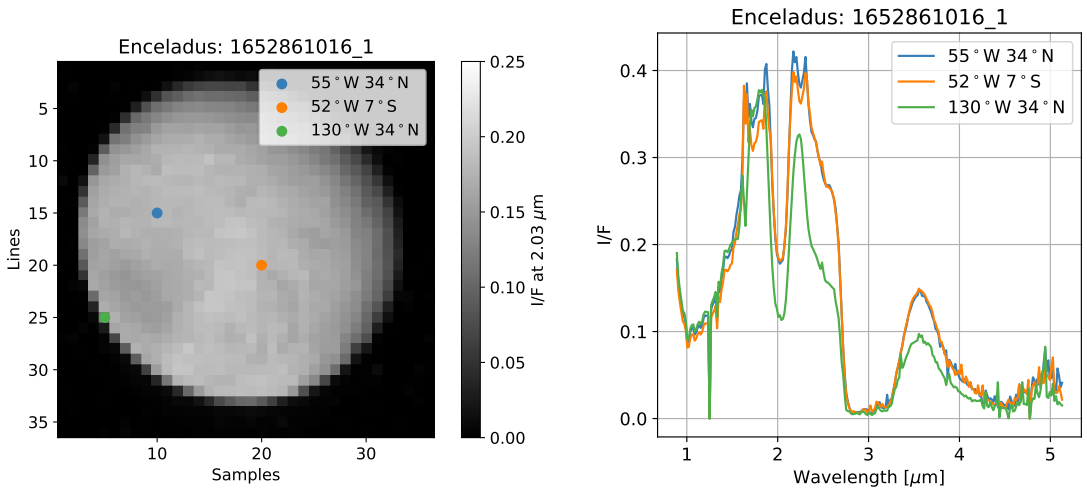

(a) Enceladus's cube 1652861016_1. Color represents the I/F at 2.03 microns.

(b) Spectra of the selected pixels in Enceladus's cube 1652861016_1 displaying 1-micron dips.

Figure 4.6: Cube depiction and spectra of selected pixels of Enceladus's cube 1652861016_1 showing 1-micron dip feature.

- **1-micron dip**: The 1-micron dip shows a particular decrease in I/F at 1.25 microns. To avoid cubes with this feature, spectra will be filtered by comparing the intensity at 1.25 microns with the data point immediately before.

4.3. Fit

The cross-relationships between the different Hapke parameters pose challenges in achieving good fits. The presented Hapke model involves ten parameters, namely surface roughness ($\bar{\theta}$), filling factor (ϕ), grain size (D), phase function parameters (b and c), CBOE coefficients (B_{C0} and h_C), SHOE parameters (B_{S0} and h_S) and the mass fraction (m). To reduce these links, certain parameters can be related to each other. The hockey-stick relation (Eq. 3.15) and the SHOE width parameter as a function of the filling factor (Eq. 3.31) are used for this purpose. Additionally, the influence of CBOE can be neglected for phase angles greater than 3 degrees, thus imposing constraints on the selection of VIMS data (Section 4.2.3). Moreover, the SHOE amplitude can be calculated using the definition given by *B. Hapke (2012)* in Eq. 3.29. This leaves five free parameters: $\bar{\theta}$, ϕ, D, b and m. Furthermore, the values of T are taken from the temperature study carried out by *G. Filacchione, et al. (2016)* [15]. They estimated temperature at a hemispherical scale, resulting in an average temperature <88 K for Enceladus, 98-118 K for Dione, and 108-128 K for Rhea. Then, Mastrapa's optical constants at 80 K are used for Enceladus, 100 K for Dione, and 120 K for Rhea.

To perform the fits, a least squares method has been deemed the best option due to its simplicity and implementation given in Python's library SciPy[5]. The Least Squares Method aims to find the parameter vector $\boldsymbol{\theta}$ that minimizes the sum of squared residuals, which is defined as:

$$\chi^2(\boldsymbol{\theta}) = \sum_{i=1}^{N} \left(y_i - f(x_i, \boldsymbol{\theta})\right)^2 , \tag{4.1}$$

where N is the number of data points, x_i are the independent variables, y_i are the observed data points, $f(x_i, \boldsymbol{\theta})$ is the non-linear model (Hapke Model in this case), and $\boldsymbol{\theta}$ is the parameter vector to be optimized (Hapke parameters). The goal is to find the $\boldsymbol{\theta}$ that minimizes χ^2.

The optimization algorithm, typically a gradient-based method, iteratively adjusts the parameters to minimize χ^2. The algorithm progresses towards the minimum of the residuals by computing the gradient of χ^2 with respect to $\boldsymbol{\theta}$ and updating the parameter vector in the direction of the steepest descent until the variation becomes minimal. This has an issue of getting stuck in a local minimum

[5]More information: `https://docs.scipy.org/doc/scipy/reference/generated/scipy.optimize.least_squares.html`

instead of converging to the real solution. Therefore, 20 combinations of initial parameters will be selected for each fit, following Sato, et al. (2014) practice [72].

Fig. 4.7 shows the sum of the residuals response surfaces of a simulated spectrum for the different pairs of parameters. Two parameters are allowed to vary on a grid while the rest are set constant. For each pair of free parameters, the residuals are plotted. These surfaces are the ones in which the least squares method moves to find the minimum in residuals, following the direction of the steepest decrease. Note that the mass fraction is not included, as it is studied on its own later in this work. Furthermore, in SciPy's implementation, the residuals are given by a cost function, that is taken as an input in the algorithm. As a first step, the measured I/F is compared to the modeled Hapke reflectance.

$\bar{\theta}$, ϕ, and b yield a shift in I/F, as seen in Section 3.2, implying a high correlation between these three parameters. The response surfaces of these pairs show areas with vanishing residuals and no clear minimum. For example, two values of b yield the same spectrum (Fig. 4.7 top left) and $\bar{\theta}$ and ϕ (Fig. 4.7 bottom right) give an entire line of minima. From these results, great uncertainty in the values of $\bar{\theta}$, ϕ, and b can be expected, while D can be estimated with greater certainty. The definition of the cost function can be varied to give greater importance to different regions of the data. In the case of Hapke model fitting, it is widespread to utilize a normalized cost function, which can be expressed as

$$\chi^2_{norm}(\boldsymbol{\theta}) = \sum_{i=1}^{N} \left(\frac{y_i - f(x_i, \boldsymbol{\theta})}{y_i} \right)^2. \tag{4.2}$$

This normalized cost function gives greater weight to the absorption features of the spectra, as they present lower I/F values. Section 5.1.2 explores the use of both cost functions aiming to find the one better suited for the problem.

4.3.1. Uncertainties and correlations

The information presented in this section is extracted from *J. Nocedal and S.J. Wright (1999)* [73] and explains how the uncertainties in the fitted Hapke parameters are found. Estimating parameter errors is a crucial part of understanding the reliability of the fitted Hapke parameters. Parameter uncertainties are calculated using the Jacobian matrix, J. It is a matrix of partial derivatives that describes how changes in each parameter affect the residuals. For a problem with N data points and M parameters, the Jacobian is

$$J_{ij} = \frac{\partial r_i}{\partial \theta_j}, \tag{4.3}$$

where, J_{ij} is the element of the Jacobian matrix, $r_i(\boldsymbol{\theta})$ represents the residuals for the i-th data point and θ_j is the j-th parameter.

One more matrix needs to be defined, the Hessian matrix H, which represents the second derivative of the parameters with respect to the cost function. Note that this is a square matrix. In order to estimate it, the Gauss-Newton method is used. It approximates the Hessian matrix using the Jacobian matrix J, as

$$\hat{H} \approx J^T J. \tag{4.4}$$

The key idea is to simplify the optimization process by avoiding the costly computation of the full Hessian matrix. This approximation is reasonable when the cost function behaves approximately quadratically near the solution. The standard errors of the estimated parameters, $\Delta\theta_i$, are obtained by taking the square root of the diagonal elements of the covariance matrix, Σ, which is the inverse of the Gauss-Newton-approximated Hessian matrix,

$$\Delta\theta_i = \sqrt{\Sigma_{ii}} \tag{4.5}$$

SciPy's non-linear least-squares method provides a numerical estimation of the Jacobian matrix at the solution. It is calculated by evaluating the function at two points, slightly perturbing each parameter, and obtaining the gradient value for each data point.

Once the standard errors have been found, the correlation matrix, R, can be calculated:

$$\hat{R}_{ij} = \frac{\Sigma_{ij}}{\Delta\theta_i \Delta\theta_j}. \tag{4.6}$$

The correlation matrix is a squared MxM matrix where each element $\hat{R}_{ij}$ represents the correlation between parameters i and j. The entries of this matrix vary from 1 (linear relation) to -1 (negative linear relation). If two or more parameters are correlated, they tend to change together in response to changes in the data, leading to parameter estimates that are interdependent. As a result, the uncertainties of the estimations grow.

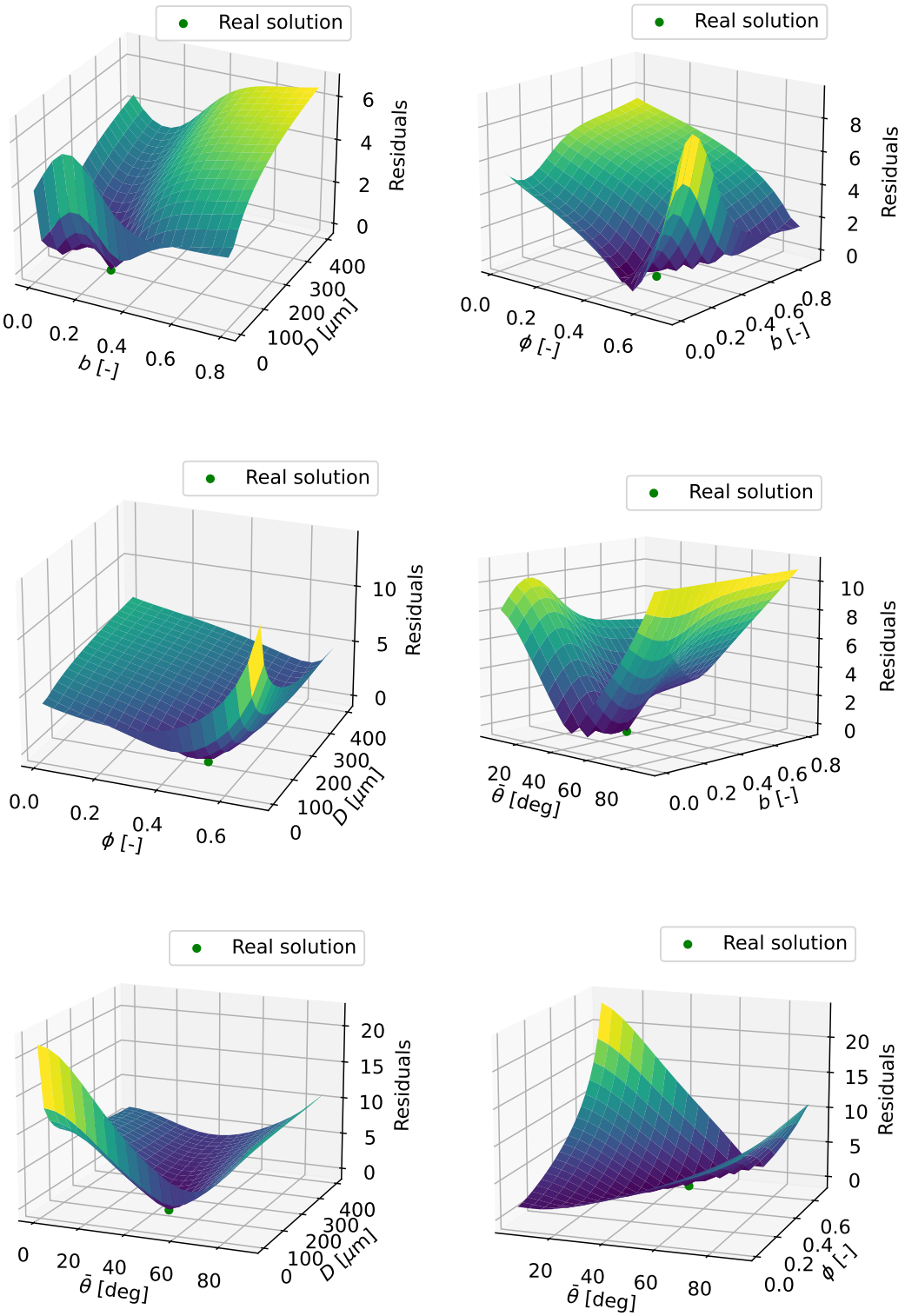

Figure 4.7: Response surface of the cost function for the combinations of the free Hapke parameters (ϕ, b, D, and $\bar{\theta}$). The characteristics of the solution spectrum are: Hapke parameters are $e = g = 30°$, $i = 0°$, $\phi = 0.5$, $D = 70$ microns, $b = 0.25$, $\bar{\theta} = 50°$ and $T = 120$ K.

5

Experimental data fit and crystallinity estimation

In this chapter two main aspects are tackled: the use of experimental data to tune the fitting procedure of the Hapke model and the investigation of different techniques for crystallinity estimation.

First, experimental data from the Solid Spectroscopy Hosting Architecture of Databases and Expertise (SSHADE) of reflectance spectra of water ice is used. This data will be fitted by the Hapke model using the algorithm described in Section 4.3. Along this section, two parts of the fitting procedure are investigated: the use of a normalized or standard cost function and fixing parameters to improve the reliability of the results.

Then, since SSHADE's experiments use fully crystalline samples, the study of crystallinity will be carried out using Mastrapa's data of optical constants. Crystallinity is assessed by four techniques: mass fraction fit through the intimate mixing formulation, the location of the 2-micron feature (through a Gaussian fit), the partial and full area of the 1.65-micron feature, and the 1.2-1.65 ratio.

As a result, a robust fitting procedure is developed to estimate the Hapke parameters and crystallinity, highlighting the caveats that should be considered when interpreting the solutions, especially when the data from VIMS is considered.

5.1. Surface characteristics: test scenario

To find the best fitting procedure, three main aspects are tackled. First, the experimental data is fitted making use of normalized and non-normalized cost functions with the aim to reduce uncertainties in the

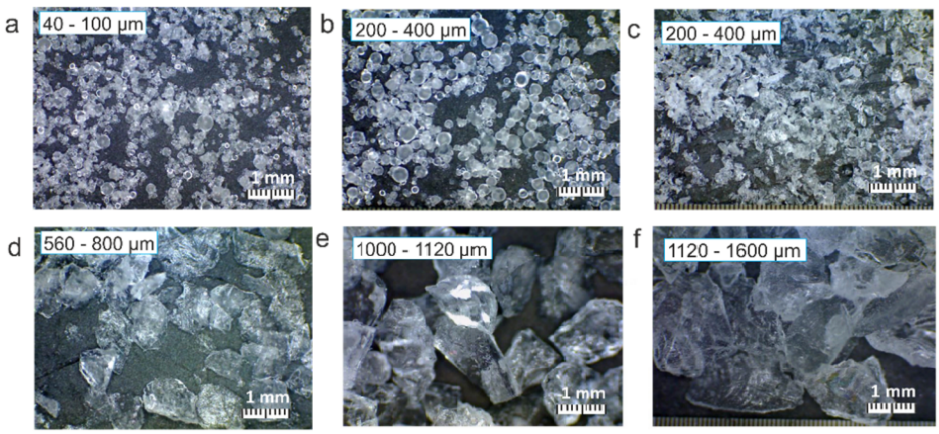

Figure 5.1: Water ice samples' optical images of (a) ∼70 μm, (b) regular ∼300 μm, (c) irregular ∼300 μm, (d) ∼680 μm, (e) ∼1060 μm and (f) ∼1360 μm [74].

estimated parameters. Then, two different fitting strategies are compared: determining all parameters (done during the normalization study) and fixing some parameters to determine the rest. Finally, the robustness of the fits is tested for variations in the parameters that are fixed and at different temperatures.

5.1.1. Experimental dataset: reflectance spectra of icy grains

The experimental data used in this section is the one developed by K. Stephan, et al. (2019) [1]. To obtain the reflectance measurements, icy particles were generated through two methods: one involved the creation of spherical water droplets, which were then frozen in liquid nitrogen, while the other method entailed crushing and sieving ice within a freezer, as illustrated in Fig. 5.1.

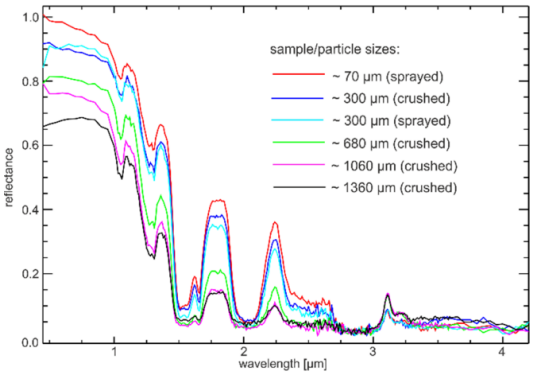

Figure 5.2: Reflectance spectra of the samples for the different grain sizes [74].

Spherical ice particles of 70 $\pm$m 30 μm were obtained using a specialized setup called the Icy Planetary Analog Producer—B (SPIPA-B), enabling consistent and precise production of spherical water ice particles. Larger spherical particles were also generated using a garden sprayer, and particles formed through crystallization in liquid nitrogen underwent sieving using 200 and 400 $\pm$m mesh screens. The size of all other particles was controlled by sieving in the freezer using a range of sieve sizes, including 200, 400, 560, 800, 1000, 1120, and 1600 μm. Following sieving, the samples were further purified by rinsing with liquid nitrogen to remove any remaining smaller ice particles. The particles were then poured into a cylinder so enough thickness was achieved to perform the reflectance measurements. After deposition on the cylinder, the reflectance spectra of the icy grains were measured at $g = e = 30^\circ$ and $i = 0^\circ$, avoiding any big opposition surge effects.

The resulting spectra are shown in Fig. 5.2. As predicted during Section 3.2, the intensity of the absorbance features decreases and particle size increases. Furthermore, subtle differences are appreciated between the different temperatures. In the following study the experimental data of 70 microns and irregular 300 microns particles at 120 K are used for the fits and the best found fitting practice is used for 300-micron spherical particles and 680-micron samples at 120 K. The resulting spectra from the experiments are shown in Fig. 5.2.

5.1.2. Free parameters: Hapke fit and cost function

Performing a non-linear least squares fit to the data described in Section 5.1.1 requires the definition of a cost function, which is to be minimized by altering the input parameters. Two different cost functions are studied: standard and normalized.

The standard cost function is the one given in Eq. 4.1, which minimizes the norm of the difference between the simulated Hapke spectrum and the experimental data. This approach gives greater weight to the part of the spectrum with a higher I/F, as the difference between the model and data is greater.

The normalized cost function is given by Eq. 4.2 and takes the relative difference between all data points. Differences at smaller values of I/F are given greater weight, providing a better fit of the lows of the spectrum: the absorption features. Particularly, as the data approaches zero, its weight in the cost function increases greatly. The effect of choosing one cost function or the other is shown in Fig. 5.3. The normalized cost shows stronger performance in the lows of the distribution and around the 1.65-micron feature, while the standard cost yields smaller residuals at greater I/F, especially in the region between 1 and 1.5 microns. When the fitted data is the 300 μm sample with irregular particles, the standard cost function shows a greater reduction of residuals at the reflectance peaks at 1.75 and 2.25 microns.

The results of the fits are found in Table 5.1. The errors associated with each value were calculated following the procedure followed in Section 4.3.1. First, the uncertainties associated with each parameter are too large to trust any of the estimated values. Consequently, it can already be concluded that

[1] For more information: `https://www.sshade.eu/data/EXPERIMENT_OP_20201223_001`

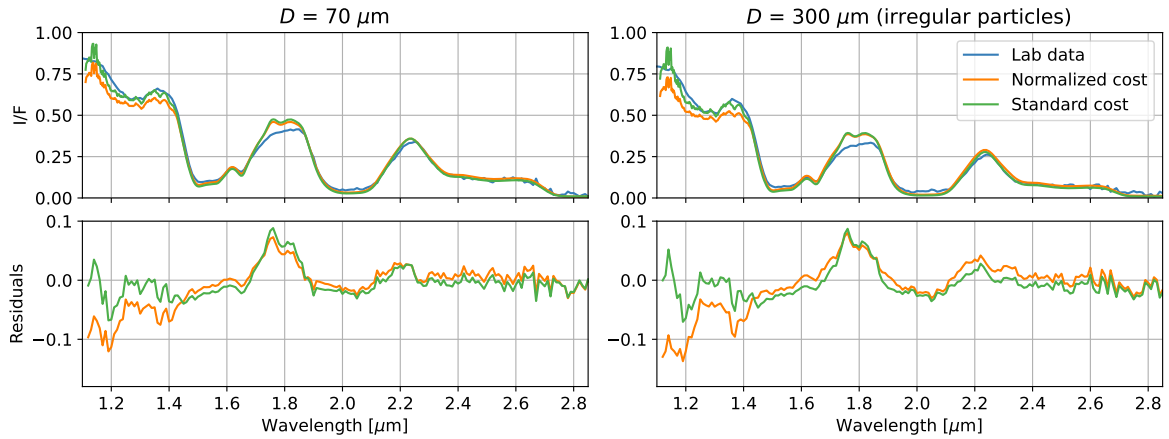

Figure 5.3: Hapke fits of the reflectance spectra of samples with grain sizes 70 and 300 μm (irregularly shaped particles) with normalized and non-normalized cost functions. The bottom row shows the residuals, namely, the difference between the modeled spectra and the experimental data. The results of the fits are presented in Table 5.1.

Table 5.1: Fitted Hapke parameters of the experimental data for different grain sizes with normalized and non-normalized cost functions. The resulted spectra is displayed in Fig. 5.3.

Expt.	Normalized Cost	b	$\bar{\theta}$ [rad]	ϕ	D [μm]
70	Y	0.3 ± 1.8	0.3 ± 1.2	0.00 ± 0.00	200 ± 900
70	N	0.3 ± 9.5	0.2 ± 10.4	0.00 ± 0.00	200 ± 7200
300	Y	0.15 ± 6000	0.6 ± 1.5	0.00 ± 0.00	400 ± 400
300	N	0.3 ± 8.2	0.2 ± 10	0.00 ± 0.00	400 ± 10000

fitting all the Hapke parameters at once is not a viable strategy, regardless of which cost function is utilized. Such high errors can be attributed to the correlation between the Hapke parameters, as stated in Section 4.3. The estimated values of ϕ are of the order of 10^{-22} while its error is of the order of 10^{-6}, which does not represent the physical reality of the sample, as the experimentalist estimated the porosity of the sample to be around 0.5.

However, the uncertainties associated with the estimated parameters using a normalized cost function present a decrease of one order of magnitude. This improvement in accuracy can be associated with giving greater weight to the absorbance features of the spectrum, as has been used for similar studies [65]. For that reason, **the normalized cost function is deemed more suitable for the problem.**

The found errors are too high to trust any of the estimated parameters. This is related to the cross-relationships between different parameters, namely the correlation between them. In particular, the correlation matrices of the fitted samples with normalized cost functions are

$$\begin{array}{c} \\ b \\ \bar{\theta} \\ \phi \\ D \end{array} \begin{array}{c} \begin{array}{cccc} b & \bar{\theta} & \phi & D \end{array} \\ \begin{pmatrix} 1.00 & -0.35 & 0.56 & -0.99 \\ & 1.00 & 0.56 & 0.48 \\ & & 1.00 & -0.43 \\ & & & 1.00 \end{pmatrix} \end{array} \quad \text{and} \quad \begin{array}{c} \\ b \\ \bar{\theta} \\ \phi \\ D \end{array} \begin{array}{c} \begin{array}{cccc} b & \bar{\theta} & \phi & D \end{array} \\ \begin{pmatrix} 1.00 & 0.79 & 0.94 & -0.79 \\ & 1.00 & 0.94 & -0.27 \\ & & 1.00 & -0.54 \\ & & & 1.00 \end{pmatrix} \end{array},$$

for 70 and 300 microns, respectively. The parameters are presented in the following order: b, $\bar{\theta}$, ϕ and D. For example, the correlation coefficient between b and $\bar{\theta}$ is -0.35. First, correlation matrices vary depending on the analyzed spectrum, as can be seen by comparing the matrices associated with each experiment. The smaller the correlations between parameters, the better their estimations. D shows an overall smaller correlation with the other parameters; yet, it is highly correlated to b, with values of up to -0.99. ϕ is correlated to b and $\bar{\theta}$, especially in the fit of the 300-micron sample, where the correlation parameters reach 0.94. $\bar{\theta}$ exhibits the second lowest correlation with all other parameters, after D.

Due to the high correlations, some parameters will be fixed with educated guesses, while others will be allowed to vary. The following section dives into the selection of which parameters should be fixed.

5.1.3. Fixed parameters

The fixed parameters approach aims to simplify the problem by giving educated guesses/ranges for some parameters to reduce the dimensions of the fit. As discussed in Section 3.2, b can be used to infer the amount of internal scatterers and impurities that are in the samples. Figs. 3.12 and 4.7 show two different regions for the values of b: below and above 0.149. By giving different initial guesses of b, the optimizer finds different solutions, as can be seen in Fig. 5.4. The fact that two different solutions are found does not represent the physical reality of the sample experiments. Given the experimental method of ice deposition by crushing and spraying, a low amount of internal scatterers can be expected. For that reason and its high correlation with D, b is fixed to 0.3, following the depiction given in Fig. 3.10 and results found in similar studies of the icy moons [65]. After fixing b to 0.3, the solutions that are found by the optimizer are unique for all experimental data.

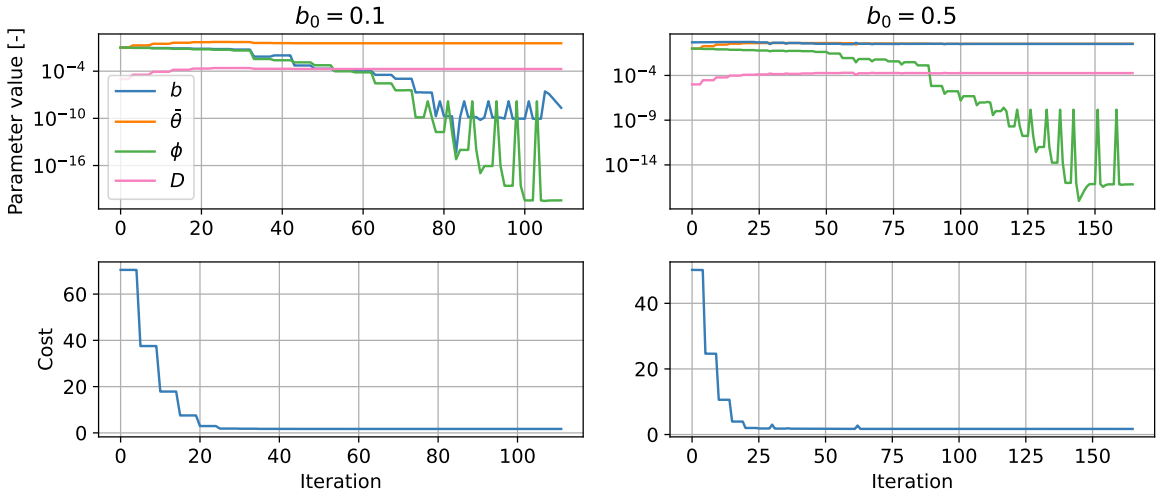

Figure 5.4: Evolution of the Hapke parameters through the optimizer iterations while fitting the 70-micron data for two different initial values of b. The bottom plots show the evolution of the total cost through the iterations.

Determining 3 parameters: $\bar{\theta}$, ϕ and D

The results of the fits for a fixed b are found in Table 5.2. The uncertainties are still too high to trust any of the presented values, yet the errors of each estimated parameter have decreased concerning the previously fitted parameters. Still, the found value of ϕ is of the order of 10^{-22}, that the porosity is close to one and there is barely any material in the sample, only empty space. This does not relate to the physical reality shown in Fig 5.1, although the images depict a high porosity sample. Fig. 5.5 shows how the parameters and cost evolve through the iterations of the algorithm. Both initial values of ϕ lead to the same estimations and uncertainties of ϕ, $\bar{\theta}$ and D.

Table 5.2: Fitted Hapke parameters of the experimental data for different grain sizes with normalized cost function and fixed b to 0.3.

Expt.	$\bar{\theta}$ [rad]	ϕ	D [μm]
70	0.3 ± 1.0	0.00 ± 0.00	200 ± 150
300	0.4 ± 1.0	0.00 ± 0.00	300 ± 150

The correlation matrices of both fits are

$$\begin{array}{c} \\ \bar{\theta} \\ \phi \\ D \end{array} \begin{array}{c} \begin{array}{ccc} \bar{\theta} & \phi & D \end{array} \\ \begin{pmatrix} 1.00 & 0.98 & 0.95 \\ & 1.00 & 0.99 \\ & & 1.00 \end{pmatrix} \end{array} \quad \text{and} \quad \begin{array}{c} \\ \bar{\theta} \\ \phi \\ D \end{array} \begin{array}{c} \begin{array}{ccc} \bar{\theta} & \phi & D \end{array} \\ \begin{pmatrix} 1.00 & 0.99 & 0.84 \\ & 1.00 & 0.87 \\ & & 1.00 \end{pmatrix}, \end{array}$$

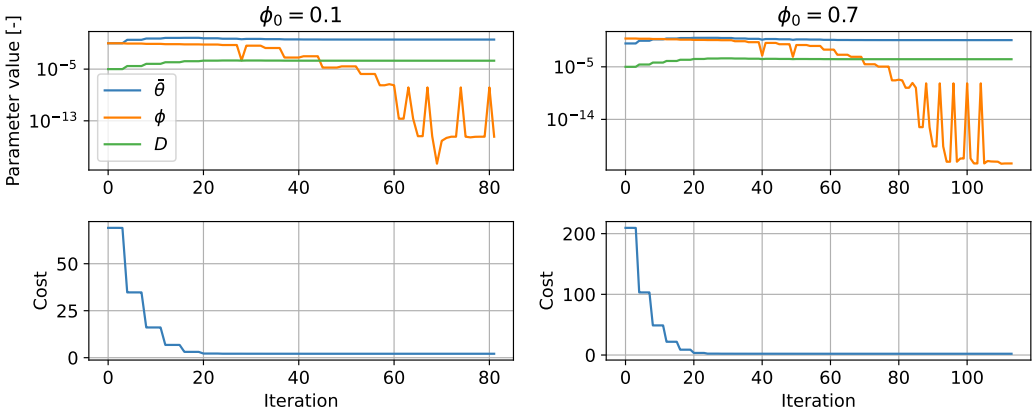

Figure 5.5: Evolution of the Hapke parameters through the optimizer iterations while fitting the 70-micron data for two different initial values of ϕ. The bottom plots show the evolution of the total cost through the iterations. The results of both initial values are identical and are shown in Table 5.2.

where the first one is associated with the 70-micron fit while the second one is the correlation at the solution of the 300-micron experiment. Correlations are higher than in the previous case and ϕ has the greatest correlation values with D and $\bar{\theta}$ (>0.98). Together with the lack of physical meaning of ϕ, this parameter will be fixed for the next step. The experimenters found the porosity of the samples to be 0.5. Estimates for the icy moons find the porosity of the regolith to be between 40 and 90%, associated with a filling factor between 0.10 and 0.60 [75, 1]. For that reason, an in-between value is selected: $\phi = 0.40$.

Determining 2 parameters: $\bar{\theta}$ and D

The results of the fits with fixed values of b and ϕ are shown in Table 5.3. The errors are below 20% of the values, representing a big accuracy improvement compared to previous steps. $\bar{\theta}$ reaches 0.79 radians (or 45 degrees), which is its upper bound in the optimization algorithm. By fixing b and ϕ, their effects are now encapsulated in the roughness. Then, its interpretation is not only linked to the definition given by Hapke but also includes the effects of these two parameters, giving an effective roughness. Next, $\bar{\theta}$ is allowed to vary between 0 and 90 degrees to account for this effect. The results are shown in Table 5.4 and they show how a better solution is found for values of effective roughness above 45 degrees. Fig. 5.6 shows how the parameters and cost evolve through the iterations of the algorithm. Both initial values of D and $\bar{\theta}$ lead to the same estimations and uncertainties.

Table 5.3: Fitted Hapke parameters of the experimental data for different grain sizes calculated by fixing b to 0.3 and ϕ to 0.4.

Expt.	$\bar{\theta}$ [rad]	D [μm]
70	0.79 ± 0.14	300 ± 40
300	0.79 ± 0.16	430 ± 50

The correlation matrices of the found solutions are

$$\begin{array}{c} \\ \bar{\theta} \\ D \end{array} \begin{array}{c} \begin{array}{cc} \bar{\theta} & D \end{array} \\ \begin{pmatrix} 1.00 & -0.69 \\ & 1.00 \end{pmatrix} \end{array} \quad \text{and} \quad \begin{array}{c} \\ \bar{\theta} \\ D \end{array} \begin{array}{c} \begin{array}{cc} \bar{\theta} & D \end{array} \\ \begin{pmatrix} 1.00 & -0.70 \\ & 1.00 \end{pmatrix}, \end{array}$$

for the 70 and 300 microns fit, respectively. Both parameters show a relatively high correlation; yet, it is a mayor improvement with respect to the previous steps.

In order to investigate the behavior of ϕ and be certain that a better set of fixed parameters is not overseen, $\bar{\theta}$ will be fixed. The experimentalists did not provide an estimation of the surface roughness of the samples; however, typical values in the icy moons of Saturn are between 20 and 30 degrees [1]. The optical images of the samples depict a big difference between both considered experiments

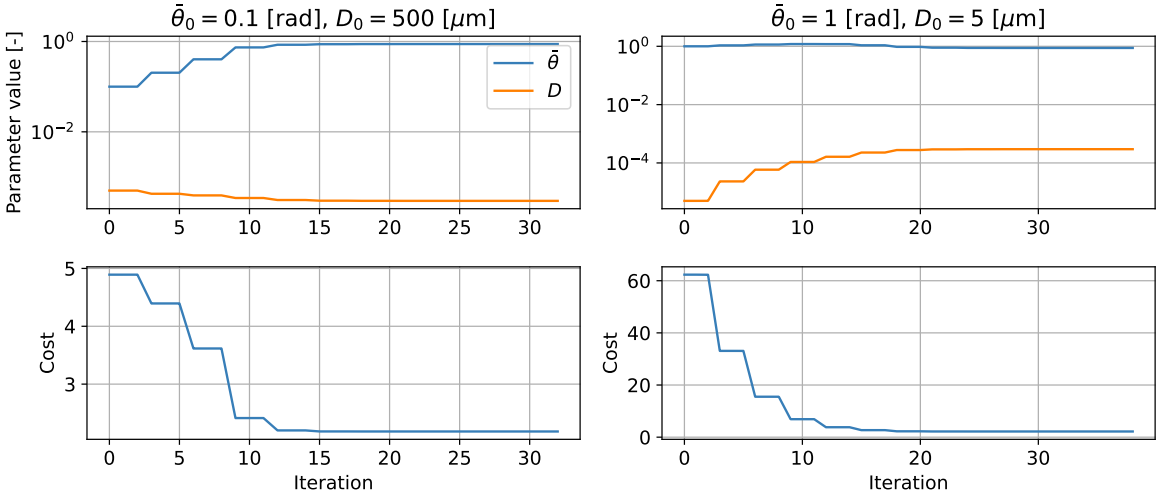

Figure 5.6: Evolution of the Hapke parameters through the optimizer iterations while fitting the 70-micron data for two different initial values of $\bar{\theta}$ and D. The bottom plots show the evolution of the total cost through the iterations. The results of both initial values are identical and are shown in Table 5.3.

Table 5.4: Fitted Hapke parameters of the experimental data for different grain sizes calculated by fixing b to 0.3, ϕ to 0.4 and letting $\bar{\theta}$ vary between 0 and 90 degrees.

Expt.	$\bar{\theta}$ [rad]	D [μm]
70	0.89 ± 0.13	300 ± 40
300	0.90 ± 0.14	400 ± 60

(Fig. 5.1). The irregular grains of the 300-micron sample have sharp angles that are related to a rough surface; while the spherical grains of the 70-micron sample show a smoother texture. Thus, roughness is fixed to 25 degrees (0.44 rad), as an in-between value between rough and smooth and significative for the surfaces of the icy moons. The results of fitting D and ϕ are found in Table 5.5. Again, the results of the filling factor do not reproduce the physical reality of the sample and the uncertainties associated with the values are too high to be trusted. In particular, the found value of ϕ for the 300-micron sample is of the order of 10^{-22} while its error is of the order of 10^{-7}. The correlation matrices of these two fits are,

$$\begin{array}{c} \\ \phi \\ D \end{array} \begin{array}{c} \begin{array}{cc} \phi & D \end{array} \\ \begin{pmatrix} 1.00 & 0.88 \\ & 1.00 \end{pmatrix} \end{array} \quad \text{and} \quad \begin{array}{c} \\ \phi \\ D \end{array} \begin{array}{c} \begin{array}{cc} \phi & D \end{array} \\ \begin{pmatrix} 1.00 & 0.89 \\ & 1.00 \end{pmatrix}, \end{array}$$

for the 70 and 300-micron spectra, respectively. The fact that both fits display a high correlation between D and ϕ may explain the poor performance of the optimization method to find the filling factor. Furthermore, this is a greater correlation than exhibited in the fits of D and $\bar{\theta}$. The fits together with their residuals are shown in Fig. 5.7a and 5.7b. The effect of fixing one parameter or the other does not yield a considerable difference in the residuals or fits. Consequently, the definition of an effective roughness by moving the upper bound of $\bar{\theta}$ to 90 degrees encapsulates the effect of the filling factor.

Table 5.5: Fitted Hapke parameters of the experimental data for different grain sizes calculated by fixing b to 0.3 and $\bar{\theta}$ to $35°$.

Expt.	ϕ	D [μm]
70	0.01 ± 0.08	200 ± 50
300	0.00 ± 0.00	270 ± 60

According to the results, the best discussed fitting strategy is fixing b and ϕ, and fitting $\bar{\theta}$ and

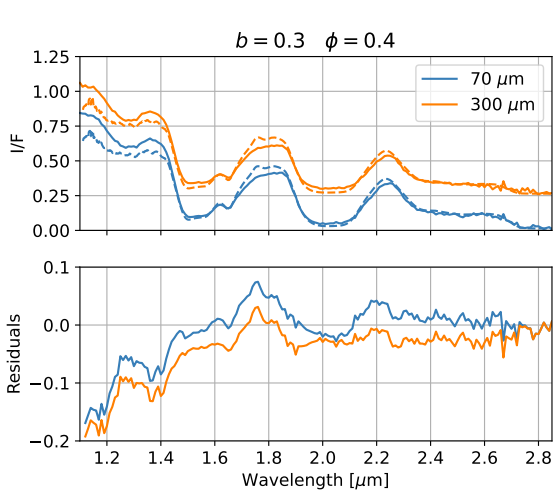

(a) Experimental data of 70 and 300 microns samples and fitted Hapke spectra (dashed), fixing b to 0.3 and ϕ to 0.4. Each spectrum is separated by an offset of 0.25. The bottom plot shows the residuals of each fit.

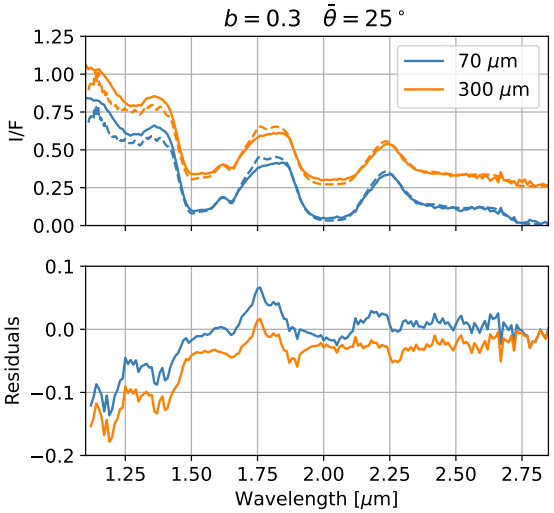

(b) Experimental data of 70 and 300 microns samples and fitted Hapke spectra (dashed), fixing b to 0.3 and $\bar{\theta}$ to 25°. Each spectrum is separated by an offset of 0.25. The bottom plot shows the residuals of each fit.

Figure 5.7: Fitted spectra of the 70 and 300 microns fitted samples and associated residuals for different fixed parameters.

Table 5.6: Fitted Hapke parameters of the experimental data with 300 microns spherical particles and 680 microns calculated by fixing b to 0.3 and ϕ to 0.4.

Expt.	$\bar{\theta}$ [rad]	D [μm]
300 (sph)	0.95 ± 0.14	440 ± 60
680	1.22 ± 0.08	620 ± 110

D. As mentioned before, surface roughness cannot be completely taken as a measure of macrotexture, but it includes the effects of forward scattering and internal scatterers (as it absorbs the action of b) and the filling factor. Both the filling factor and forward scattering nature of the samples are related to exogenic processes taking place in the Saturnian system, for that reason this new special roughness estimator can serve as an indicator of the action of surface processes shaping the icy moons. Then, this fitting procedure is applied to the spectra of experimental samples with 300 microns spherical grains and 680 microns. The results and fit can be found in Fig. 5.8 and Table 5.6. The first thing that can be noticed is the increase in roughness between the samples as grain sizes increase. By looking at the experimental images of the ice shown in Fig. 5.1, the irregularities of the samples increase as grain size increases; thus, an increase in $\bar{\theta}$ is expected. Grain size also increases as experimental particle size increases, reaching values within the estimations given by the experimentalists. However, the 70 microns sample, lead to a predicted value of around 200 μm. Hapke model is believed to overestimate the values of D by up to a factor of 2.5 in the Mie scattering region; which is associated with particles whose sizes are of the same order as the incoming radiation [55]. On the other hand, Fig. 5.8 shows an increase in residuals for greater grain sizes, particularly at lower wavelengths. This points toward a decrease in the accuracy of the Hapke model to simulate the reflectance spectra of larger grains; yet, the fitted Hapke parameters reflect the physical reality of the particles.

Finally, Fig. 5.9 shows the effect of varying b ad ϕ in the values found by the optimizer. In particular, regardless of the values of the fixed parameters, the trends are sustained. As seen by the correlation matrices, b is greatly correlated to D while it has a lower correlation with ϕ. Conversely, both ϕ and b are correlated to $\bar{\theta}$. Variations in the fixed parameters lead to differences of up to 400 microns (particularly for larger particles) and 25 degrees (for smaller grains). The grain sizes of the icy moons are believed to be below 200 microns [25, 76]. This smaller grain size range is where the influence of b is smaller. On the other hand, the filling factor has been found to vary little within each moon, varying between 0.35

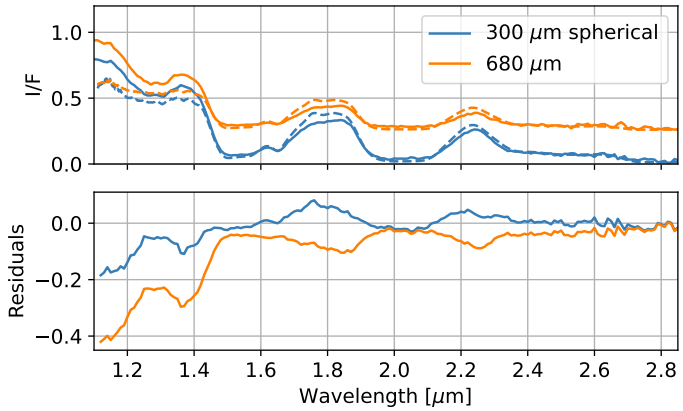

Figure 5.8: Experimental data of 300 microns with spherical grains and 680 microns samples and fitted Hapke spectra (dashed), fixing b to 0.3 and ϕ to 0.4. Each spectrum is separated by an offset of 0.25. The bottom plot shows the residuals of each fit.

and 0.3 in Enceladus, 0.6 and 0.55 in Dione, and 0.2 and 0.05 in Rhea [1]. As ϕ varies little between the terrains of the moons, the found value of roughness serves as a relative comparator between the terrains of each moon. Moreover, an increase in effective roughness is correlated with greater values of ϕ, showing how this effective roughness encapsulates its effect.

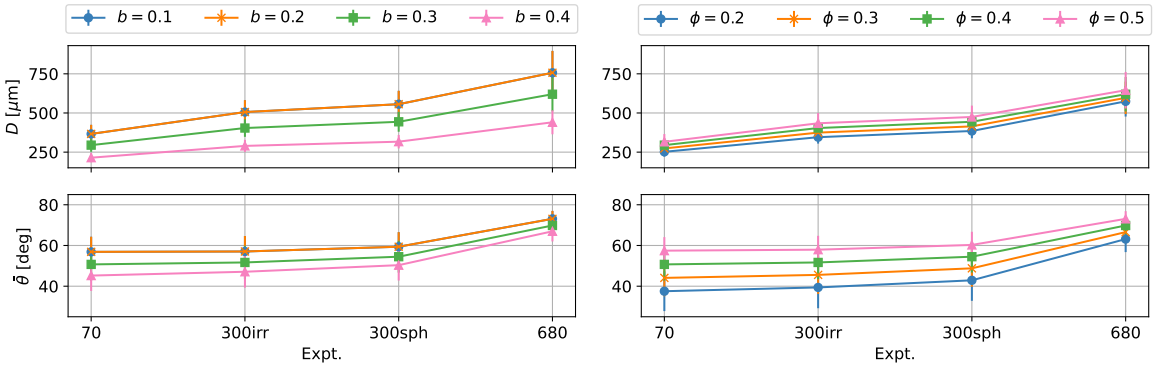

Figure 5.9: Fitted values and errors of $\bar{\theta}$ and D for the different experiments. The left plot shows variations in the value of b with a constant value of $\phi = 0.4$ and the right plot shows variations in ϕ with a constant $b = 0.25$.

What happens when the temperature of the studied sample is not known? Fig. 5.10 shows the results of the fits of the experimental data of 70 and 300 microns at 120 K, using Hapke-modeled spectra with the optical constants of Mastrapa at temperatures of 80, 100, 120, 140, and 150 K. These results show variations in D of less than 50 microns and smaller than 1 degree in roughness. This means that the differences in the fitted values due to disparities in temperature between the optical constants used in the model and the actual samples are smaller than the uncertainties of the fitted values of D and $\bar{\theta}$. Thus, the effect of temperature can be neglected.

5.2. Crystallinity estimation

Crystallinity is another parameter that can be inferred from a given spectrum. Four different approaches are studied: **the mass fraction fit through the intimate mixing formulation, the location of the 2-micron feature, the partial and full area of the 1.65-micron feature, and the 1.2-1.65 ratio**. The ice samples used in the experiments are expected to be fully crystalline, not allowing to use of the data as a validation method for the estimation techniques. Then, the experimental data is used when a value of m can be directly obtained, as it is known it should approach 0 to match the physical reality of the samples. For all methods simulated Hapke spectra with Mastrapa's optical constants is used.

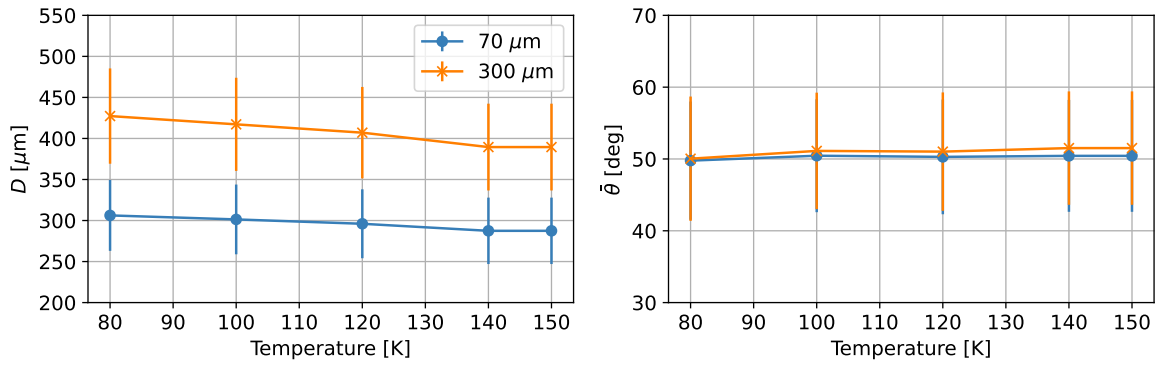

Figure 5.10: Fitted values of D and $\bar{\theta}$ of the 70-micron and irregular 300-micron samples using different temperature values of the optical constants.

5.2.1. Intimate mix fit

As presented in Section 3.2.4, Hapke intimate mixing formulation can be used to infer the abundance of different species in a given spectrum. By using Mastrapa's amorphous and crystalline optical constants, a fit following a least-squares optimization can be performed to find the mass fraction of amorphous ice, m. As seen in Section 3.2 and Fig. 3.17, several spectral features are influenced by the morphology of the ice, especially at 1.65, and 3.1 microns, being the 1.65 absorption feature being the strongest; yet the variations are subtle are localized when compared with the entire spectrum.

Fitting the mass fraction together with D and $\bar{\theta}$ over the spectral range of the 70 and 300 irregular particle experiments gives values of 0.1 ± 0.3 and 0.2 ± 0.4 of m. The values of $\bar{\theta}$ and D do not vary compared to the presented results in Table 5.4, which is consistent with low correlation coefficients (<0.01) of m with these values. However, the errors of the estimated values of m mean that the mass fraction cannot be found by a total fit of the spectrum.

The mass fraction produces changes in the cost that are much smaller than the change produced by D and the effective roughness over the entire spectrum; leading to small gradients of m in the solution and big errors. For that reason, a new approach is followed: first, a fit is performed to find D and $\bar{\theta}$ with a fixed value of $m = 0$ (crystalline fit), then, D and $\bar{\theta}$ are fixed to their found values and m is fit in the vicinity of the 1.65-micron absorption feature, particularly in the range 1.45-1.8 μm. This approach should amplify the effect of m by constraining the optimizer to the area in which m has the greatest influence. The results are 0.0 ± 0.7 and 0.1 ± 0.6, respectively.

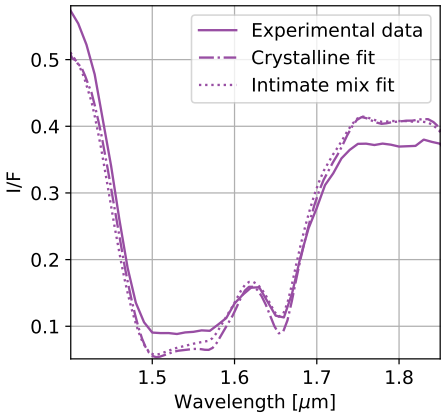

(a) Intimate mixing model fit of the 300-micron sample with irregular particles at 120 K. The fit gives an estimated amorphous ice mass fraction of 0.1 ± 0.6.

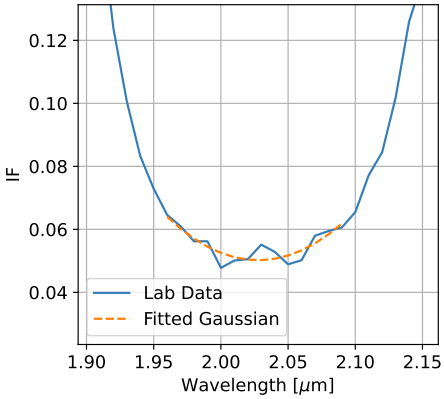

(b) Gaussian fit of the 2-μm feature of the 300-micron sample with irregular particles at 120 K. The fit gives 2.0306 ± 0.0018 μm as the position of the minimum.

Figure 5.11: Fits for crystallinity estimation: intimate mix Hapke formulation around the 1.65 absorbance feature and determination of the 2-micron feature's location.

An example of the fit is seen in Fig. 5.11a. The crystalline fit provides a solution whose I/F lays below the 1.5-micron minimum and later over the 1.8-micron, giving an incorrect fit of the mass fraction. Second, the intimate mixing model is formulated for a homogeneous mixture of amorphous and crystalline ice, which is not necessarily the case for these crushed ice particles. This leads to uncertainties and errors in the estimations that are incompatible with the experimental values. In light of these results, **mass fraction determination through an intimate mix fit will not be used for the study**.

5.2.2. Location of the 2-micron feature

As stated in Section 3.2.4 and Fig. 3.17, the location of the 2-μm feature can be used as an estimator of crystallinity [61, 14]. Fig. 5.12 shows the findings of *Mastrapa (2008)* regarding the shift between the location of the 2-micron feature depending on the crystallinity state. They recorded a position of 2.022 μm for Ic ice at 80 K, compared to 2.001 μm for low-density amorphous ice.

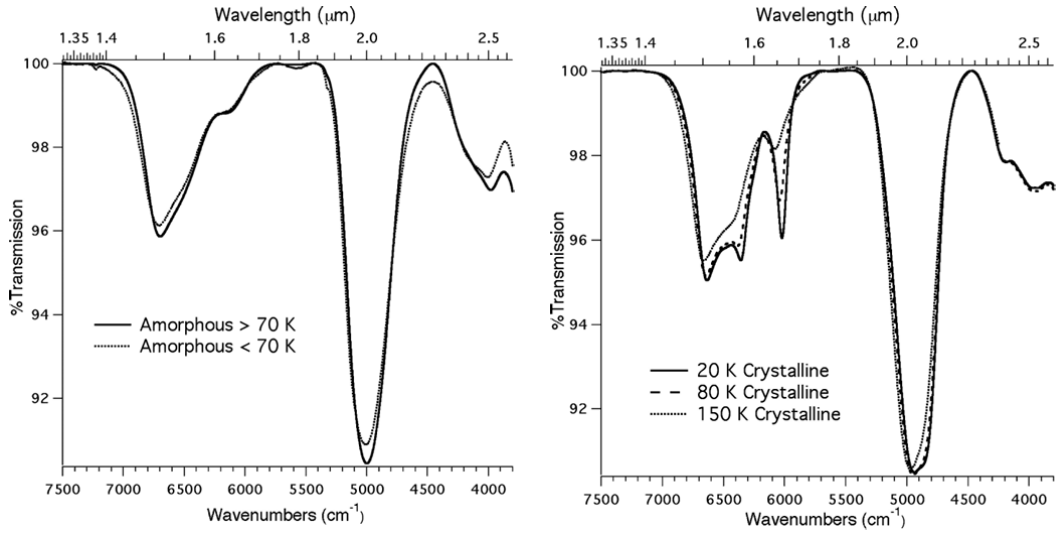

Figure 5.12: Experimental transmittance spectra of amorphous ice (left) and crystalline (right) at different temperatures [61].

To find its position in a given spectrum, a Gaussian fit is performed around the 2-micron feature. Particularly, the fitted function goes as,

$$f(x) = Ae^{-(x-\mu)^2/(2\sigma^2)} + f_0$$

where A is the amplitude, μ is the distribution's center location, σ is the standard deviation and f_0 is the baseline. To find the parameters of the distribution, another non-linear least squares method is implemented, as given by SciPy's curve_fit function[2]. By fitting the parameter μ and its uncertainty, as given in Section 4.3.1, the location of the 2-micron feature can be determined. The fit is then performed between 1.91 and 2.14 microns, as this range was found to give the best results when applying it to particularly noisy data from the icy moons. The fit for the 300 microns irregular particle sample is shown in Fig. 5.11b, giving a location of the minimum at 2.0306 $\pm$ 0.0018 μm.

To study the effect of different ice characteristics, the location of the 2-micron feature is calculated for simulated Hapke spectra with varying T and D and $\bar{\theta}$. The results of such variations are shown in the top row of Fig. 5.14. For the top middle plot, the temperature of Mastrapa's optical constant measurements is varied randomly for each point between 60, 80, 100, and 120 K. The points in the right plot are calculated for 100 K and random values of D and $\bar{\theta}$, between 10 and 200 microns, and 0.4 and 1.4 radians, respectively. Both ranges were selected based on typical values of the icy moons' surfaces. Notably, the location of the 2-micron feature follows a linear trend for all cases, making it a strong technique for crystallinity estimation. In experimental data, a gradual shift depending on amorphous ice content was observed [61]. For that reason, a linear fit can be performed to find the associated values of m as a first approximation,

$$\mu = (2.0296 \pm 0.0001) - (0.01735 \pm 0.00018)m,$$

[2]More information: `https://docs.scipy.org/doc/scipy/reference/generated/scipy.optimize.curve_fit.html`

where μ represents the location of the minimum and the errors are the standard deviations of the parameters. From this equation, the value of m can be found for a given location as,

$$m = \frac{2.0296 - \mu}{0.01735}, \tag{5.1}$$

and its uncertainty is calculated following the quadratic error propagation [73],

$$\Delta m = \sqrt{\left(\frac{\Delta\mu}{-0.01735}\right)^2 + \left(\frac{2.0294 - \mu}{(-0.01735)^2}\right)^2 0.00018^2 + \left(\frac{0.0001}{-0.01735}\right)^2}. \tag{5.2}$$

Applying this formula to the fit performed in Fig. 5.11b gives a value of $m = -0.07 \pm 0.10$. The fact that m takes a negative value shows that the range found in Mastrapa's optical constants does not fully cover the full range the location of the 2-micron peak can take; yet, it provides a value of m close to a purely crystalline ice, as expected by the experimentalist. Another point is the uncertainty, which is greater than the estimated value of m. However, errors of the order of 0.1 are acceptable when dealing with ice whose values of m are about 0.3, as is expected in the terrains of the icy moons [13]. From these results, **the location of the 2-micron feature is deemed to be a robust crystallinity estimator and will be used further in this work**.

5.2.3. Area study of the 1.65-micron feature

The 1.65-μm absorbance feature is sensitive to crystallinity, as discussed in Section 3.2, but also to grain size and temperature.

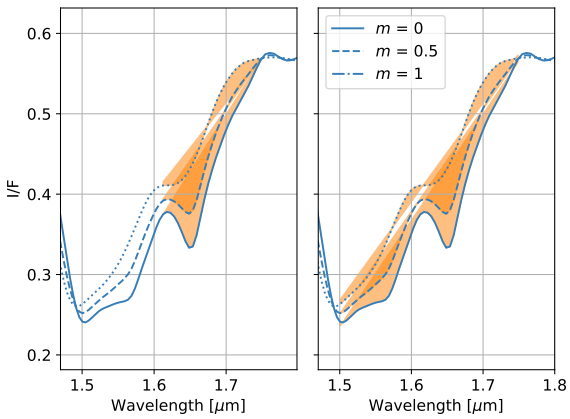

Figure 5.13: Hapke simulated spectrum for different mass fractions of amorphous ice and representation of the partial and full area around the 1.65-micron feature.

To try to isolate the effect of crystallinity, two areas are studied. First, the partial area of the 1.65-micron peak is calculated as the area between a linear fit of the values at 1.61 and 1.75 microns (Fig. 5.13 left) and the I/F distribution. Then, the full area is calculated as the area between a linear fit of the values at 1.5 and 1.75 microns (Fig. 5.13 right) and the I/F distribution.

Hapke simulated spectra with Mastrapa's optical constant show how both areas decrease linearly as the mass fraction of amorphous ice increases. To study the effect of the different parameters on the spectra between 1.5 and 1.75 microns, random values of temperature and D and $\bar{\theta}$ roughness are selected, as previously done for the location of the 2-micron peak. The results are reported in the bottom row of Fig. 5.14.

If temperature, grain size, and roughness are constant, both the partial and full area vary linearly with crystallinity, as it shows a high correlation coefficient of up to 0.98. When noise is introduced in the value of T, the linear trend is still sustained with correlation coefficients around 0.92. However, introducing random values of T, D, and $\bar{\theta}$ breaks the correlation between the areas and mass fraction, with associated correlation coefficients around 0.8. While the location of the 2-micron feature is consistently correlated to crystallinity for every scenario, both areas are not a consistent measurement of crystallinity, as different grain sizes and roughness break the linear correlation.

To break the dependency with T, D, and $\bar{\theta}$, the found areas are normalized by the area of a purely crystalline Hapke spectrum. Figs. 5.16a and 5.16b show an example of the normalization for both

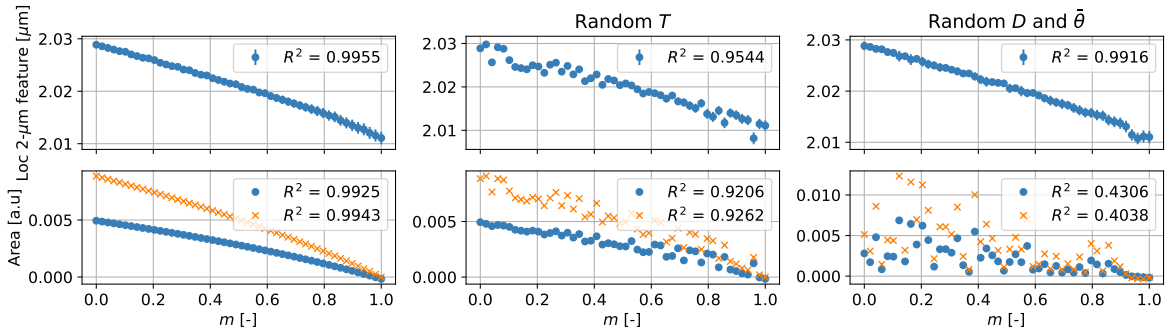

Figure 5.14: Location of the 2-μm feature and partial (blue) and full area (orange) of simulated spectra with varying m with constant D, $\bar{\theta}$ and T (left), random T and random D and $\bar{\theta}$. Uncertainty in the location of the 2-micron feature is smaller than the points.

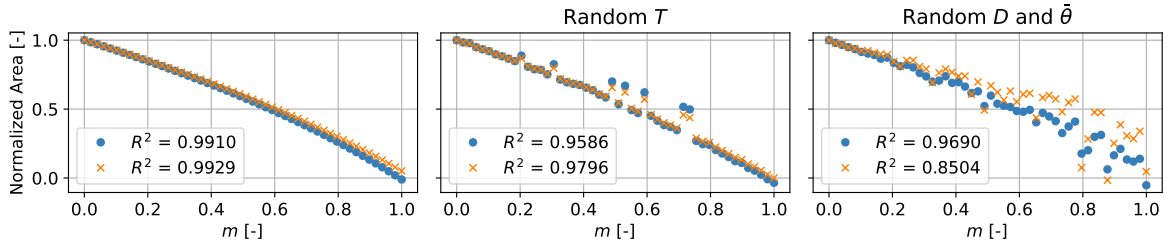

Figure 5.15: Normalized partial (blue) and full area (orange) of simulated spectra with different amorphous ice mass fractions for constant parameters, random T, and random Hapke parameters.

a Hapke-modeled spectrum and experimental data. The partial area is calculated, then the spectra is fitted assuming it is crystalline ($m = 0$) and the area of the simulated spectrum is calculated. The ratio of both areas gives the normalized partial area. The effect of this normalization is shown in Fig. 5.15, which recovers the linear trend for both cases of random T and random D and $\bar{\theta}$. Therefore, normalizing by the area of a crystalline spectrum with the same temperature, grain size, and roughness greatly isolates the influence of mass fraction. However, Fig. 5.16b shows how different the areas may be compared to Hapke-modeled spectra. This may affect the reliability of the normalized area when applied to real spectra.

The normalized partial area (Fig. 5.13 left) shows a greater correlation (0.97) with the mass fraction of amorphous ice than the normalized full area. For that reason, **the normalized partial area will be used as a technique for crystallinity estimation**.

5.2.4. Crystalinity ratio: 1.2-1.65

The 1.2-1.65 ratio consists of calculating the quotient between the I/F values at 1.2-μm continuum and 1.65-μm. It was used for crystallinity estimation on Enceladus by Brown, et al. (2006) [26]. The same study as the one performed for the location of the 2-micron feature and the areas is carried out for the ratio to analyze its sensitivity to variations in T, D, and $\bar{\theta}$. When T, D and $\bar{\theta}$ are kept constant, there is a linear relation between the ratio and m. However, there is no correlation when D and $\bar{\theta}$ are varied. For that reason, **the 1.2-1.65 ratio will not be used further as a crystallinity estimation technique**.

5.3. Summary

In this chapter, two main aspects have been tackled: the use of experimental data to tune the fitting procedure and the investigation of different techniques for crystallinity estimation.

First, by fitting spectral data of water ice grains from SSHADE, a fitting strategy for the Hapke model has been developed: **fixing** $b = 0.3$ **and** $\phi = 0.4$**, and fitting** D **and** $\bar{\theta}$. Surface roughness was first allowed to vary only between 0 and 45°. After fixing the parameters, $\bar{\theta}$ is allowed to vary between 0

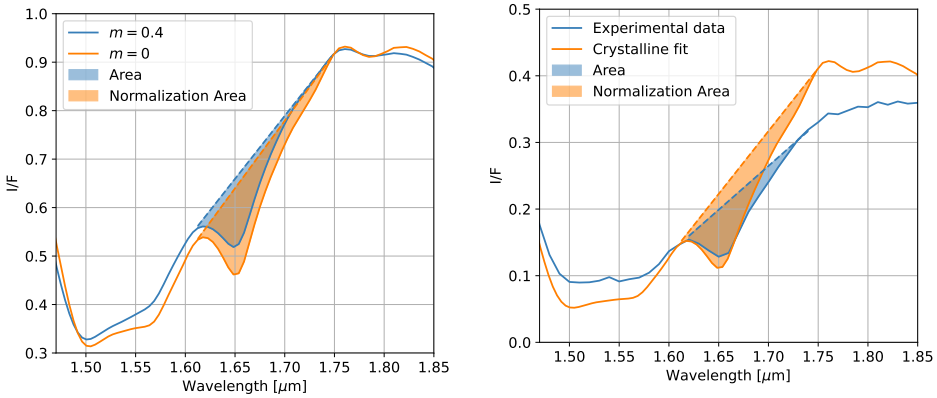

(a) Hapke simulated spectra of crystalline ice and intimate mixture with 40% amorphous water ice. The crystalline partial area is 0.0099 while the mixture's is 0.0066, giving a normalized area of 0.67.

(b) Experimental data of irregular 300-micron grains and Hapke simulated crystalline fit. The partial area of the experimental data is 0.0040 while the Hapke-modeled spectrum's area is 0.0071, giving a normalized area of 0.56.

Figure 5.16: Area calculation procedure for Hapke simulated spectra and experimental data.

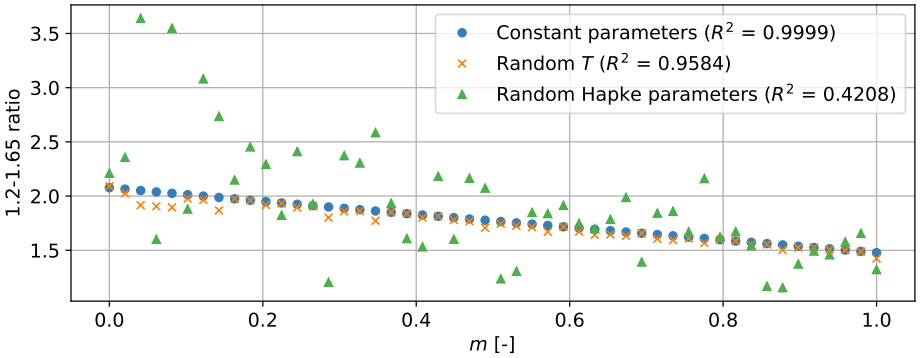

Figure 5.17: 1.2-1.65 micron ratio for different amorphous ice mass fractions and constant T and Hapke parameters, random T, and random Hapke parameters (D and $\bar{\theta}$).

and 90° to account for the different values of b and ϕ. $\bar{\theta}$ is now referred to as effective roughness, as it does not only encapsulate the smoothness of the surface. Variations in b affect the estimations of D; yet, this effect is smaller for lower values of D, which are expected in the surfaces of the icy moons. Furthermore, the effect of temperature in the estimated values of D and effective roughness can be neglected.

Since the experimental spectra are fully crystalline, the crystallinity estimation techniques have been studied using simulated Hapke spectra. The different approaches of crystallinity estimation are the 1.2-1.65 ratio, the mass fraction fit through the intimate mixing formulation, the partial and full area of the 1.65-micron feature, and the location of the 2-micron feature (located through a Gaussian fit). Normalizing the values of the area by one of purely crystalline Hapke spectra with the estimated values of D and $\bar{\theta}$ has been found to isolate the effect of crystallinity in simulated spectra; however, due to a lack of experimental data with amorphous ice, this technique could not be tested. Then, **the normalized partial area of the 1.65-micron feature and the location of the 2-micron feature** will be used for the icy moons to assess the amount of amorphous ice on the icy moons.

6

Applications on icy moons: Rhea, Dione, and Enceladus

To determine the surface characteristics of the icy moons, the model described in Section 3.2 and developed in Section 5.1 is used, obtaining estimations of grain size (D) and effective surface roughness ($\bar{\theta}$). Furthermore, the morphology of the ice is investigated following the methods described in Section 5.2: the mass fraction of amorphous ice (m) determined through the location of the 2-micron feature and the normalized partial area of the 1.65-micron feature.

For Rhea, Dione, and Enceladus, three studies are carried out. First, cubes with well-resolved terrain units are analyzed to study local features. Second, pixels are analyzed along longitudinal lines for selected latitudes. Finally, the main areas subjected to the various exogenic processes (Sartunian, anti-Saturnian, trailing, and leading hemispheres at the equator, north, and south poles) are studied for a comparative study. To summarize, this analysis ranges from the smallest scales resolved by the VIMS instrument to the planetary level.

6.1. Methodology

The surface characteristics (D and $\bar{\theta}$) are obtained through a Hapke fit from the spectra of the pixels fulfilling the selection criteria stated in Section 4.2.3. Each spectrum's fit is performed using the temperature of the moon found by *G. Filacchione, et al. (2016)* [15] and fixing the parameters b and ϕ to 0.3 and 0.4, as discussed in Section 5.1.3. The estimation of D depends on the values of b, while it is independent of ϕ. However, the influence of b is smaller for smaller grain sizes. Grain size on the icy moons is expected to be below 200 microns [65, 1]. In this region, the influence of b on D is small (Fig. 5.9); hence, the estimations of D can be interpreted as real grain size. On the other hand, $\bar{\theta}$ strongly depends on b and ϕ, and therefore it represents a special roughness that takes into account the effect of these two characteristics of the surface. It will be referred to as *effective roughness*. To account for the influence of these two parameters, $\bar{\theta}$ is now allowed to vary between 90° and 0°, as done in Section 5.1.3, instead of constraining the upper bound to 45°. For all studies, 20 fits with random initial conditions are performed to avoid finding a local minimum in the cost function, instead of the absolute one.

Ice morphology is estimated through two different techniques. First, the location of the 2-micron feature is calculated through a Gaussian fit, from which m and its associated error can be estimated following Eqs. 5.1 and 5.2. Furthermore, the normalized partial area of the 1.65-micron region is used as a crystallinity estimation technique, as described in Section 5.2.3.

Statistical considerations and uncertainties

When dealing with the longitudinal and areal study of the main areas of the moons, pixels coming from different flybys are considered. To ensure that the different pixels of the same terrain represent the same physical reality, the Shapiro-Wilk test for normality is performed on the results of each location (Appendix A.1). If the estimated values through the Hapke fit and crystallinity indicators of each pixel in

the same region follow a Gaussian distribution, they are averaged to find a representative value with a reduced uncertainty. There are several reasons why the values may not follow a Gaussian distribution:

- **Size**: Different flybys may have different pixel sizes. While one pixel may be small enough to represent the edge of a crater, another may be too large; representing different terrains with different characteristics.
- **Noise and convergence**: Some particularly noisy pixels or features affecting the spectra may lead to high uncertainties in the fits and results that could fall outside of normality. This is especially the case for the crystallinity estimators, as noise in the 1.65 or 2-micron ranges can greatly affect the estimation. Furthermore, particularly oblique illumination conditions may give spectra with little intensity that may lead to non-representative values of D and $\bar{\theta}$.
- **Diurnal changes**: Different flybys may record pixels in the same area at different local times. Depending on the time of exposure to solar radiation, changes in crystallinity may occur.

Thus, when the fitted values of an area fail the Wiki-Shapiro test, a further investigation is carried out to discern the reason, as a single outlier is enough to lead to a rejection of the normality hypothesis. If the failed hypothesis comes from differences in size, the averaged procedure is still performed, as the given value would represent the influence of local terrain as well as the general trend. If the reason is noisy data, those pixels are removed.

In the case of D, ϕ, and m, each pixel's value has an associated uncertainty coming from the fit, while the normalized area of the 1.65-μm area does not. To account for the uncertainty of each value, the mean and error of the first three are calculated following an inverse-variance weighting, where the data with smaller errors are given a greater weight. This way, estimations with high uncertainties, due to noisy data or oblique illumination conditions, have a smaller influence on the averaged value. On the other hand, the mean of the area is calculated following a standard average procedure, and its error is estimated by dividing the standard deviation of the sample by the square root of the sample size. A description of both averaging procedures is presented in Appendix A.2. As mentioned before, oblique illumination conditions may yield faulty values of the fit, with low uncertainties in either roughness or grain size. For that reason, the estimations of each pixel are analyzed to discard the possibility of obtaining a biased average.

Test case

An example of the different pixel characteristics of one particular area is shown in Fig. 6.2b and each spectrum is shown in Fig. 6.1. The results of each pixel are shown in Fig. 6.2a, giving averages of $D = 97 \pm 5$ μm, $\bar{\theta} = 56 \pm 2$ deg, $m = 0.21 \pm 0.01$ and area of 0.64 ± 0.03. When applying the Wiki-Shapiro test to the data, all results fulfill the hypothesis of following a Gaussian distribution but the area, whose pixels 17 and 18 show outlying values. These pixels do not have any particular characteristic that could explain the difference observed with the others, especially considering that no change in crystallinity is appreciated in the values of m. The presence of these outliers can be attributed to noise, as the 1.65-micron area feature is represented by only 3 VIMS points, making it particularly sensitive. Discarding those two pixels, the normality hypothesis turns positive, giving a new value of the area of 0.60 ± 0.01. This represents an example of the approach to averaging the results from different pixels, and it is carried out for all presented results.

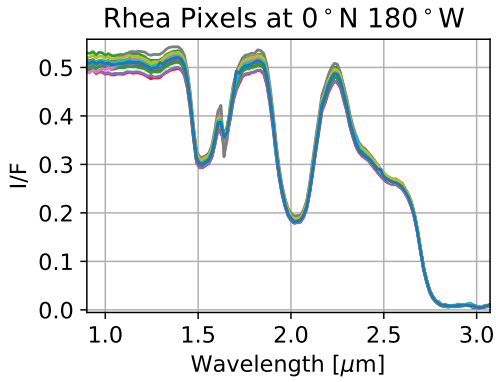

Figure 6.1: Reflectance spectra of Rhea's anti-Saturnian hemisphere. The estimated surface characteristics are found in Fig. 6.2a.

Spectra from pixels that fall under the same area of interest are studied to obtain the relevant terrain characteristics. Each pixel comes from a different cube, and each cube has a particular viewing geometry, that determines the shape and size of the pixel. The terrain depicted in the image shows craters of different sizes. For that reason, it is important to analyze the results obtained by each fit to conclude the overall terrain characteristics rather than localized features. The pixels are selected using a built-in functionality of PyVIMS that gives the pixel of a cube that contains a given location. Cubes

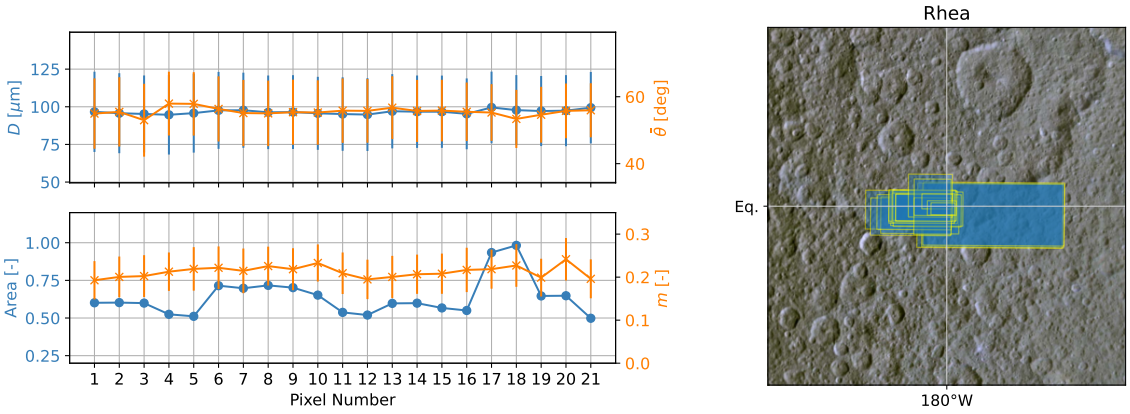

(a) Fitted values (D and $\bar{\theta}$) and crystallinity estimators (area and m) for each Rhea's pixel fulfilling the selection rules from Section 4.2.3 at 0° N 180° W.

(b) Pixel close-up of Rhea's at 0° N 180° W. Blue patches represent the extent of the different pixels taken by VIMS that fulfill the selection rules (21). The image expands from 15° N to 15° S and 195° to 165° W.

Figure 6.2: Estimated values and pixel extend at Rhea's anti-Saturnian hemisphere. Each pixel is taken from a different cube from flyby R1 and the spectrum of each pixel is shown in Fig. 6.1.

from different moons are organized according to the flyby. For Rhea, the considered flybys and the amount of cubes, in brackets, are R1 (129) and R2 (51). Dione's are D1 (122), D2 (66), D3 (33), D4 (10) and D5 (58). Finally, Enceladus' cubes are taken from E0 (23), E1 (11), E2 (30), E5 (7), E6 (14), E8 (31), E10 (72), E11 (38), E12 (10), E13 (63), E14 (68), E16 (64), E17 (10), E20 (25), E21 (28) and E22 (21). Data from a total of 984 cubes are used for this study.

6.2. Terrain units

Terrain units were selected for the three studied moons according to the region's data availability and scientific interest. Particularly, one cube for Rhea (1511726125_1), two for Dione (1649318884_1 and 1507745050_1), and two for Enceladus (1829241298_1 and 1500061286_1) are presented in this section. The relative errors of the estimated values of each pixel can be found in Appendix B.

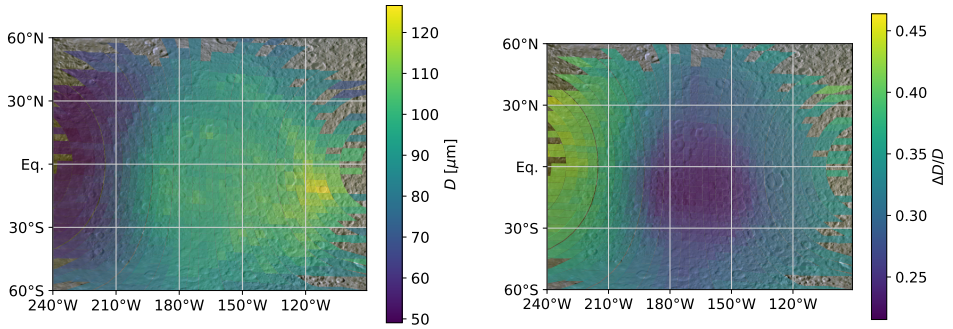

Figure 6.3: Terrain unit of Rhea and found values of D and its relative error ($\Delta D/D$). The cube is 1511726125_1, with a pixel average size of 39 km/pixel.

Only the errors of D, $\bar{\theta}$ and m are presented, as they are obtained through the Jacobian matrix of the fit. Furthermore, the errors have the same behavior in all terrains: the lower the parameter, the higher the relative error. This entails that regions with low estimated values do not have a reliable value; yet, the trends that they represent can be trusted. Typical relative errors of D are below 40%, but they can reach up to 90% in regions with very small grains. $\bar{\theta}$ has smaller relative errors, less than 30% and $\Delta m/m$ can reach up to 70% in very crystalline regions. The error coming from the fits is mostly in the same range of values, giving greater relative errors to the estimations with smaller parameter values. An example of Rhea's cube and the associated relative error is shown in Fig. 6.3, showing

errors that reach up to 45%. Note that the regions with the smallest values of D are the ones exhibiting the greatest relative errors.

As a reminder, 0° longitude is located in the Saturnian hemisphere. In the western direction, there is the leading hemisphere, at 90°W, which always faces the moon's direction of motion. After it comes to the anti-Saturnian hemisphere, facing away from the planet at 180°W, and the trailing hemisphere, opposite to the direction of motion at 270°W.

6.2.1. Rhea

The analyzed terrain of Rhea corresponds to cube 1511726125_1, taken during R1. This cube shows wide coverage in latitude, expanding from 60° N to 60° S, as well as in longitude, from 240° to 90° W. It expands into the beginning of the darker terrain that dominates the trailing hemisphere to the leading crater-full side, going through an in-between region with fewer impact craters and brighter terrain. Each one of the parameters is shown in Fig.6.4.

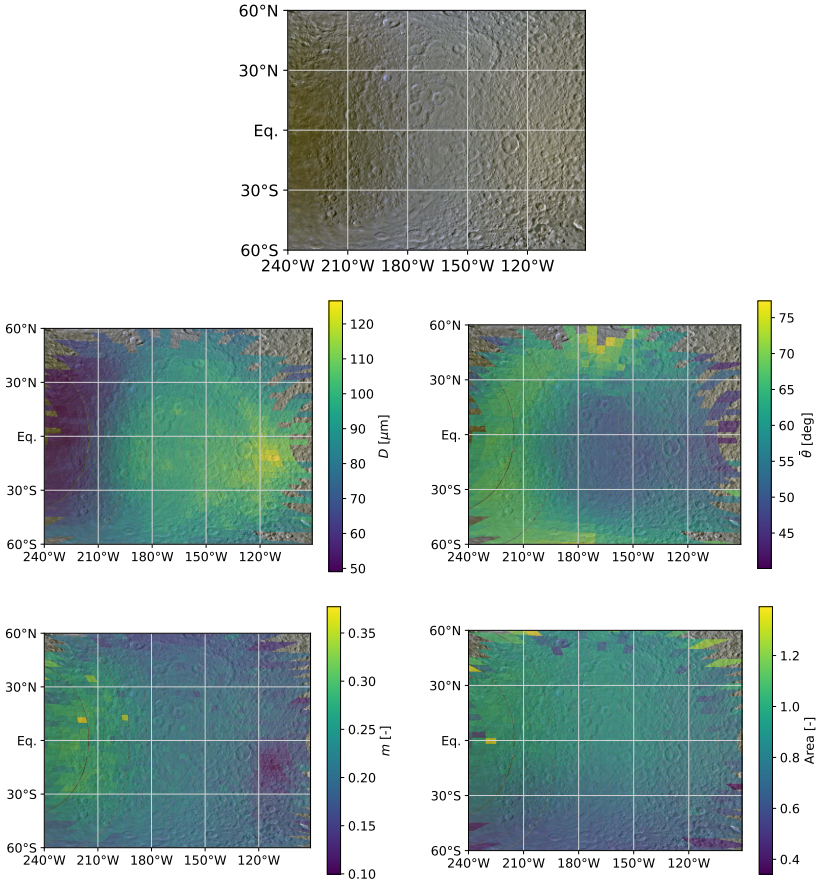

Figure 6.4: Terrain unit of Rhea and found values of D, $\bar{\theta}$, location of the 2-μm feature and normalized area of the 1.65-μm characteristic. The cube is 1511726125_1, with a pixel average size of 39 km/pixel.

The greatest values of D and smallest m correspond to the Inktomi crater, situated at 14°S 112°W. Due to its prominent ray pattern, Inktomi is likely to be the youngest crater in the Saturnian system [10]. It displays the greatest grain sizes, with values reaching up to 120 μm in the crater and 100 μm on its ray pattern. Furthermore, it displays the lowest values of mass fraction of amorphous ice, with up to 90% crystalline ice, which is not consistent with other estimations that give a maximum value of 67% [13]. The heat released during an impact vaporizes and melts the icy regolith, triggering the re-crystallization of amorphous ice [41]. This process competes with the fall of vaporized material that flash-freezes forming an amorphous lattice. The result of Fig. 6.4 suggests that the crystallization due to the release of thermal energy dominates over the deposition of solidified amorphous ice. Moreover, the vaporized material that falls again on the surface is likely to be warmer than the nearby terrain, as the only way it can lose thermal energy is through radiation. Once it falls on the surface, sintering may

be triggered, as thermal energy is transmitted between the deposited grain and the settled regolith, increasing grain size on the top layers. A slight reduction of surface roughness is also observed in the ray pattern. The deposition of ejecta may have softened the terrain, leading to lower values of $\bar{\theta}$.

The central region of the cube is located in Rhea's anti-Saturnian hemisphere. This region is characterized by densely cratered plains and more degraded material and displays in-between values of D and m, and smoother terrain. Particularly, 20% of the icy regolith is expected to be amorphous. The grain size distribution shows larger grains in some particular craters. Impact craters in this region are older, suggesting a possible relation between grain size and age compared to Inktomi.

Rhea's trailing hemisphere is dominated by dark terrain, produced by the impact of energetic electrons and the bombardment of exogenic material. This region displays the lowest values of D and the greatest estimations of $\bar{\theta}$ and m. The amorphization of ice in this region may be due to the lattice disruptions due to the chemical reactions triggered by the impact of plasma and energetic electrons [38]. This causes an overall increase in the amount of amorphous ice, reaching mass fractions of up to 35%. Furthermore, the overall reduction in the albedo of the region may cause an increase in $\bar{\theta}$ and a reduction in D.

The normalized area does not display crystallinity alterations around Inktomi. Greater values of the normalized area are related to a greater presence of crystalline ice; however, an increase in its value is observed toward the dark terrain.

6.2.2. Dione

Two terrain units are analyzed for Dione, cube 1649318884_1 and 1507745050_1, taken during flybys D2 and D1 respectively. These cubes cover areas of Dione with different terrains.

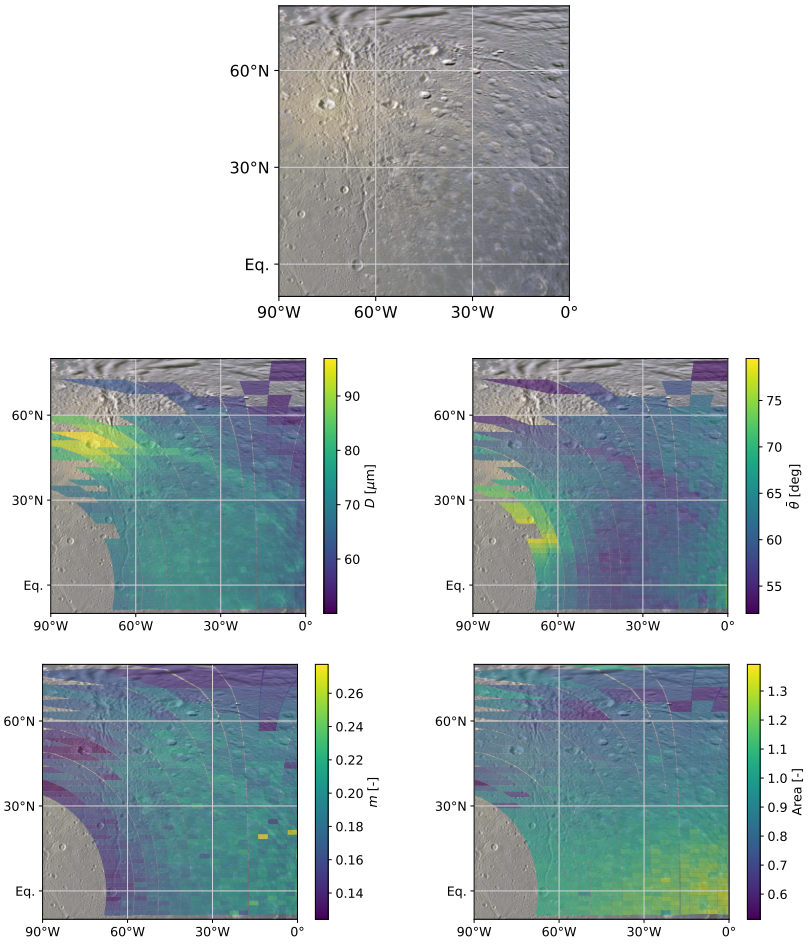

Figure 6.5: Terrain unit of Dione and found values of D, $\bar{\theta}$, m and normalized area of the 1.65-μm feature. The cube is 1649318884_1, with a pixel average size of 30 km/pixel.

Fig. 6.5 shows Creusa, an impact crater that leaves bright ray patterns across the moon. It also

features the less cratered plain of Dione in the Saturnian hemisphere. The second cube (Fig. 6.6) depicts a close-up of the wispy darker terrain that dominates the trailing hemisphere.

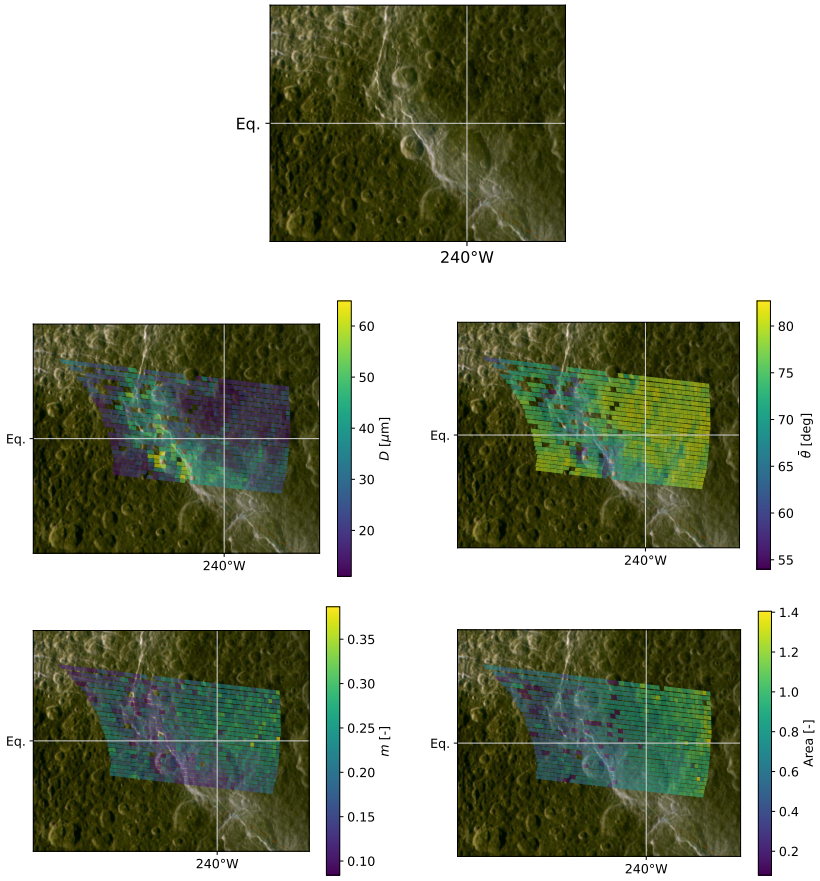

Figure 6.6: Terrain unit of Dione and found values of D, $\bar{\theta}$, m, and normalized area of the 1.65-μm feature. The cube is 1507745050_1, with a pixel average size of 4 km/pixel. The image expands from 230° to 260° W and from 12° S to 12° N.

The impact crater Creusa can be seen in the upper left of the first cube (Fig. 6.5). As the case with Inktomi, Creusa is a young crater that displays an increased value of D and a greater abundance of crystalline ice ($\sim$95%). The crater's ray pattern expands to the East, exhibiting greater grain size than the surrounding terrain. Nevertheless, a lower value of surface roughness is observed on the ray pattern than at the crater. This was also observed for Inktomi; yet, it is more prominent for Creusa.

The cube expands into the Saturnian side of Dione, formed by densely cratered plains. This region displays an intermediate value of grain size, roughness, and a greater value of m. This region has some highly degraded craters that may explain the reduction in roughness and greater abundance of amorphous ice, as the material has been exposed to cosmic radiation for a longer time.

The terrain displays the greatest value of $\bar{\theta}$ toward the leading hemisphere. The pixels at the left of the cube fall on a fracture that may explain this increase. In this region, ice becomes more crystalline. The leading hemisphere is more prone to impacts and E-ring deposition. Ejected material from the impact of E-rings particles may be related to the increase in crystallinity and surface roughness, due to the alteration of surface texture.

Once again the area does not show any variations at Creusa and appears to be correlated with m. Furthermore, roughness and grain size appear to be anti-correlated, as was the case for Rhea's cube.

The results of the second cube's analysis are presented in Fig. 6.6. This cube features a prominent brighter chasma with surrounding craters in the dark terrain of the trailing hemisphere.

The fractures display a brighter terrain with larger grains, smoother terrain, and more crystalline ice. These fractures are a consequence of tectonic movements that expose ice from deeper layers, not as affected by the processes taking place in the region. As this material is brighter, the results show smaller values of $\bar{\theta}$, not necessarily connected to the topography and texture of the terrain. However,

the edged and central peaks of the craters display smoother features and greater values of D, while the in-between depression does not. Furthermore, the fractures and crater's edges and central peaks have an abundance of amorphous ice around $\sim$15%, while it raises to 35% in the surroundings. A possibility may be that due to the inclination of these features (crater's central peaks and edges, and ridges), dark material does not settle as much as in other regions, and impacts or tectonic movements shake the dark material toward the center of the craters and fractures.

The dark terrain is a consequence of chemical reactions due to plasma impact and implantation of ions; leading to a greater presence of carbon [15]. Chemical alterations of water ice can lead to the disruption of crystalline lattices, leading to a greater abundance of amorphous ice in the top layers of the regolith. Moreover, an increased value of surface roughness in the dark terrain is consistent with previous studies pointing toward a negative correlation between albedo and $\bar{\theta}$ [62].

Along the entire cube, the anti-correlation between grain size and effective roughness is evident, following *M. K. Shepard and P. Helfenstein (2007)* [62] results. According to the experimentalists, surface roughness may be more influenced by mm-level structures and the smallest grains often form cohesive surface structures of up to a few millimeters. Furthermore, the area displays an overall gradient in the eastern direction, but it does not represent any of the terrain features.

6.2.3. Enceladus

Two cubes of Enceladus are analyzed: 1829241298_1 and 1500061286_1, taken in E22 and E2 respectively. The first represents a craterless plain in the Saturnian hemisphere, while the second is a close-up of the Tiger Stripes in the Enceladean southern region.

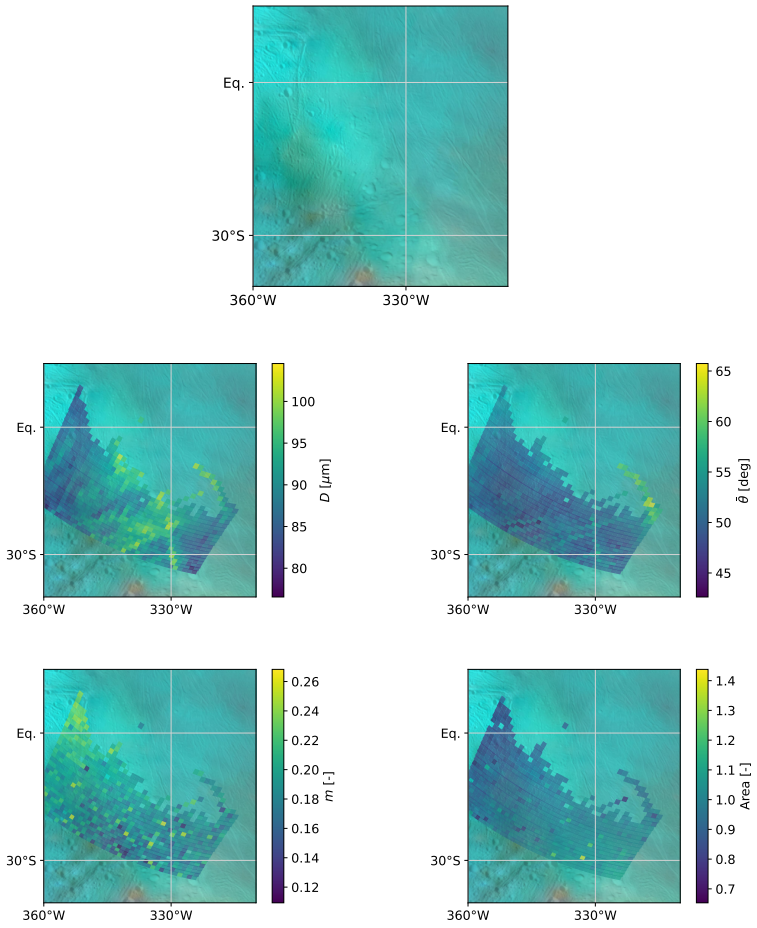

Figure 6.7: Terrain unit of Enceladus and found values of D, $\bar{\theta}$, m and normalized area of the 1.65-μm feature. The cube is 1829241298_1, with a pixel average size of 5 km/pixel.

The terrain in Fig. 6.7 shows a fracture at approximately 30° S 330° W with a greater associated grain size than its surroundings. The ridge is caused by tectonic activity, that may have led to a localized

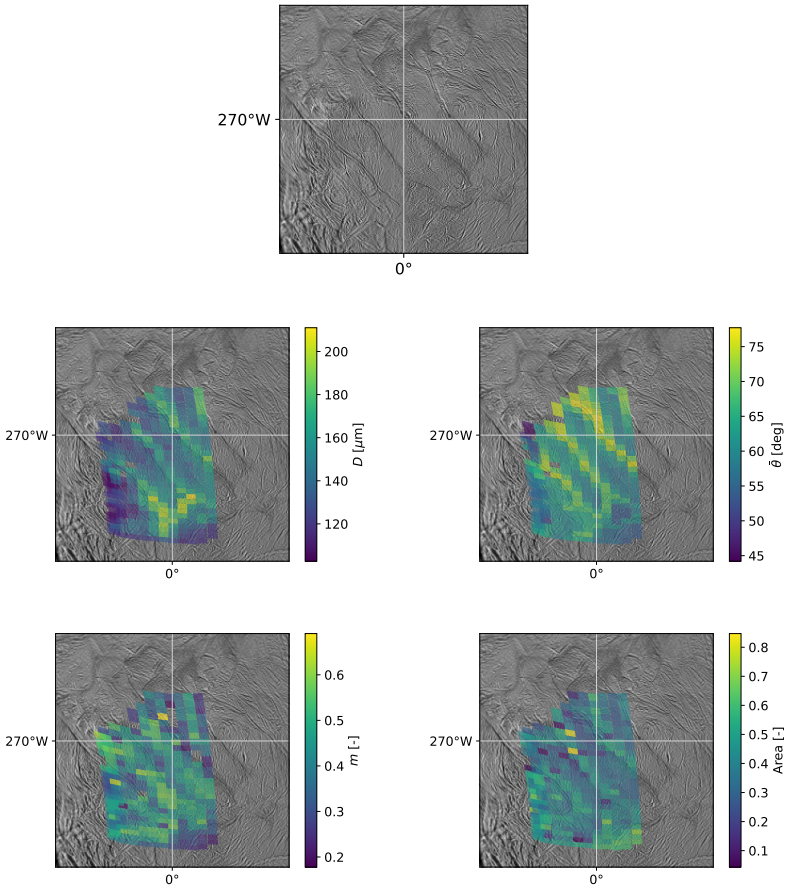

Figure 6.8: Terrain unit of Enceladus and found values of D, $\bar{\theta}$, m and normalized area of the 1.65-μm feature. The cube is 1500061286_1, with a pixel average size of 9 km/pixel. The image expands from 230° to 260° W and from 12° S to 12° N.

release of thermal energy that triggers sintering among grains and increases D. The overall increase in grain size in the cube compared to the previous ones can be attributed to plume deposition, as larger particles do not have enough kinetic energy to escape Enceladus. $\bar{\theta}$ shows a subtle correlation with grain size, contrary to previous cubes. Surface roughness also exhibits little variation across the cube ($\sim$20°), denoting a similar terrain texture along the entire cube. Once again this may be related to the deposition of plume particles, that give a more uniform texture.

In terms of crystallinity, m does not show any correlation with the local ridges. However, a gradient can be seen, representing a small increase in the abundance of amorphous ice towards the West and North. This is also supported by the value of the area, as it decreases in this direction.

The tiger stripes are shown in Fig. 6.8. They display larger grains in the Sulci from which the plumes emanate, reaching values of up to 200 microns. In between the regions, there is a decrease in D, reaching values of 160 microns. The estimations of grain size in this terrain represent the greatest out of all analyzed terrains. This increase may be caused by two reasons: the largest plume particles fall in this area and the stripes are known to be a hotspot, producing sintering. The effective roughness displays a greater value at the sulci while the terrain in between the fractures has a smoother terrain, correlated with D. However, while D reaches its maximum at the bottom pixels, $\bar{\theta}$ is maximum at the top of the cube. The fractures are known to be particularly steep, as they connect the subsurface ocean with the surface, then a high roughness was expected. Furthermore, the constant addition of new particles may alter the regolith structure on the mm level, leading to a more irregular texture than in their surroundings. The region also has the greatest abundance of amorphous ice, reaching values up to 60% in between the sulci. As the sulci are warmer, constant recrystallization may be taking place, while this process is less strong in between the sulci.

Moreover, the wide coverage and amount of flybys performed on Enceladus allow the study of

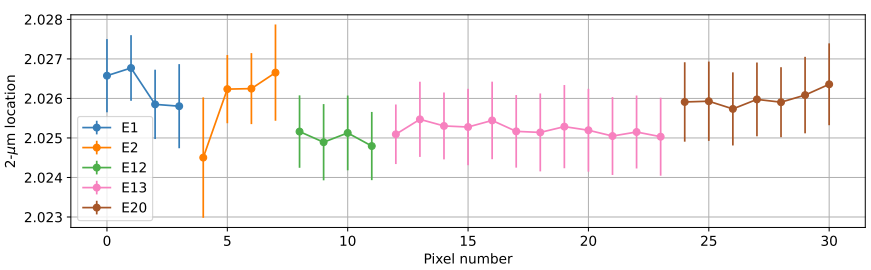

(a) Location of the 2-micron feature for different cubes taken in different flybys of the anti-Saturnian hemisphere (0° N 180° W).

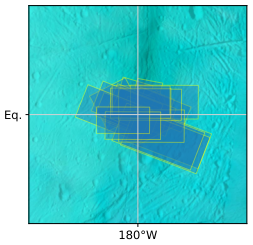

(b) Close-up of Enceladus pixels and terrain used for the study of diurnal variations in crystallinity. The image expands from 15° S to 15° N and 165° to 195° W.

Figure 6.9: Estimated amorphous ice mass fraction and pixel extent at Enceladus's anti-Saturnian hemisphere.

the same terrain at different times over its diurnal cycle. Fig. 6.9a shows how the anti-Saturnian hemisphere (0°N 180°W) exhibits changes in crystallinity during the Enceladean orbit. PyVIMS library does not offer a direct way to infer local time from a given pixel; hence, the observation angles and sub-solar point (point on the surface where the sun is at zenith) are used as a qualitative measure of irradiation time. Flybys E1 and E2's cubes were taken at similar local times (the deviation observed at the first point of E2 is attributed to noise in the data) during sunset (Sub-solar point at around 22° S 240° W), meaning that the terrain has been irradiated for several hours. On the other hand, pixels from flybys E12, E13, and E20 were taken closer to midday, as the incidence angle reached values as low as 10°. Particularly, pixels of E12 and E13 were taken during the same local time, while E20 represents the terrain a few hours later. During these flybys, ice is irradiated for less than 5 hours. A trend of increased crystallinity with irradiation time can be attributed to the result, as flybys E1, E2, and E20 (taken at later local times) show a greater degree of crystallinity. The used pixels and terrain can be observed in Fig. 6.9b. An important consideration following this is that the pixels vary in area from 119 to 1235 km^2; yet, most pixels are between 200 and 700 km^2. Furthermore, within each flyby the pixel area, i.e. E13's pixels ranges from 160 to 1235 km^2 and does not present significant differences in the location of their 2-micron feature. This supports recent findings about diurnal crystallinity variations in Ganymede [77].

6.3. Longitudinal study

This section shows the results from the study of different pixels along longitudinal lines at fixed latitudes. A total of 763 pixels from flybys R1 and R4 were utilized for Rhea, 1,100 pixels from 5 flybys for Dione, and 1,883 pixels from 16 flybys for Enceladus.

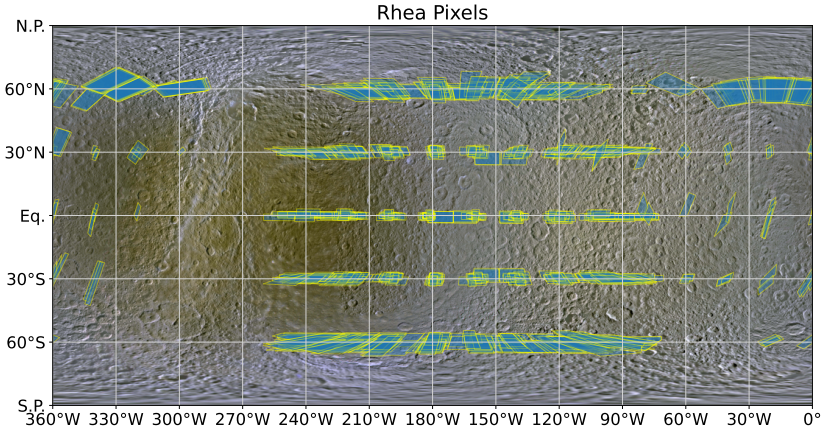

Figure 6.10: Analysed pixels of Rhea along the longitudinal lines. Results are shown in Fig. 6.13. Background image: NASA/JPL-Caltech/Space Science Institute/Lunar and Planetary Institute.

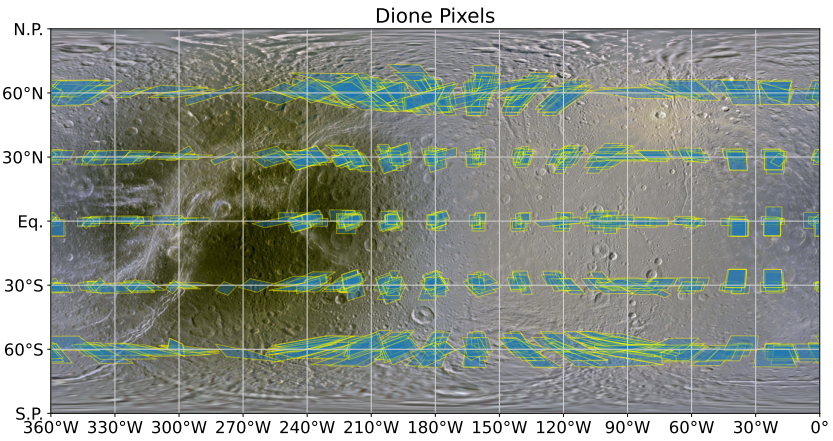

Figure 6.11: Analysed pixels of Dione along the longitudinal lines. Results are shown in Fig. 6.14. Background image: NASA/JPL-Caltech/Space Science Institute/Lunar and Planetary Institute.

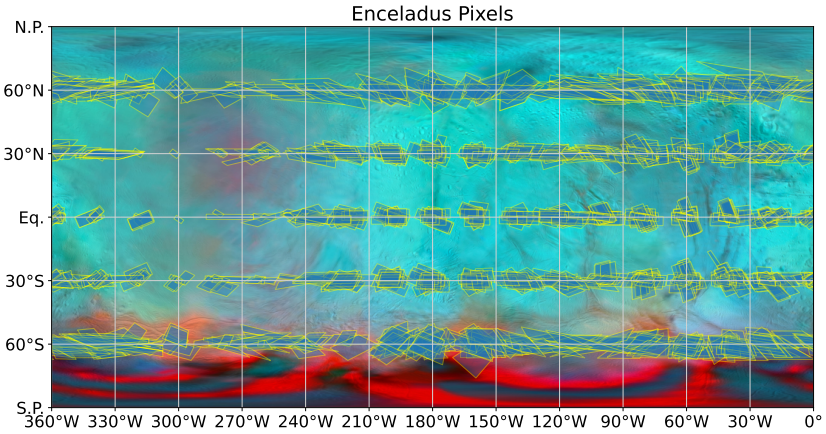

Figure 6.12: Analysed pixels of Enceladus along the longitudinal lines. Results are shown in Fig. 6.15. Background image: NASA/JPL-Caltech/Space Science Institute/Lunar and Planetary Institute.

The coverage for each moon is shown in Figs. 6.10, 6.11 and 6.12. The estimated parameters at each location together with the coverage and pixels are presented in Appendix C.

6.3.1. Rhea

Cassini's coverage of Rhea carries two caveats that should be considered: the trailing hemisphere has less coverage and because of the shapes of the pixels and proximity between locations at high latitudes there may be overlap between pixels.

In Fig. 6.13, the averaged values of the parameters at each location and the associated errors are reported.

The observed trends are generally smooth for all parameters, showing an overall anti-correlation between D and $\bar{\theta}$, consistent with previous studies [62]. Grain sizes range between 6 ± 4 and 114 ± 8 microns, and surface roughness varies between 46 ± 8 and 89.9 ± 0.1 degrees, with a clear distinction between the different areas of Rhea. The mass fraction of amorphous ice varies between 0.36 ± 0.04 and 0.05 ± 0.02.

Grain size peaks at the anti-Saturnian side of Rhea, while it displays an in-between value of m and a minimum for $\bar{\theta}$. The processes taking place at the trailing and leading hemispheres increase grain size and decrease surface roughness. The deposition of E-ring particles in Rhea's leading hemisphere leads to a decrease in grain size, alterations in the terrain's texture, and a decrease in the abundance of amorphous ice. Notably, m shows an abrupt decrease at 80°W, followed by a sudden increase as it approaches the Saturnian hemisphere. D also exhibits this behavior, but not as pronounced. This may be due to a localized area of E-ring deposition, expanding only 20°W, which correlated with brighter terrain.

On the other hand, the trailing hemisphere is affected by the bombardment of co-rotating plasma,

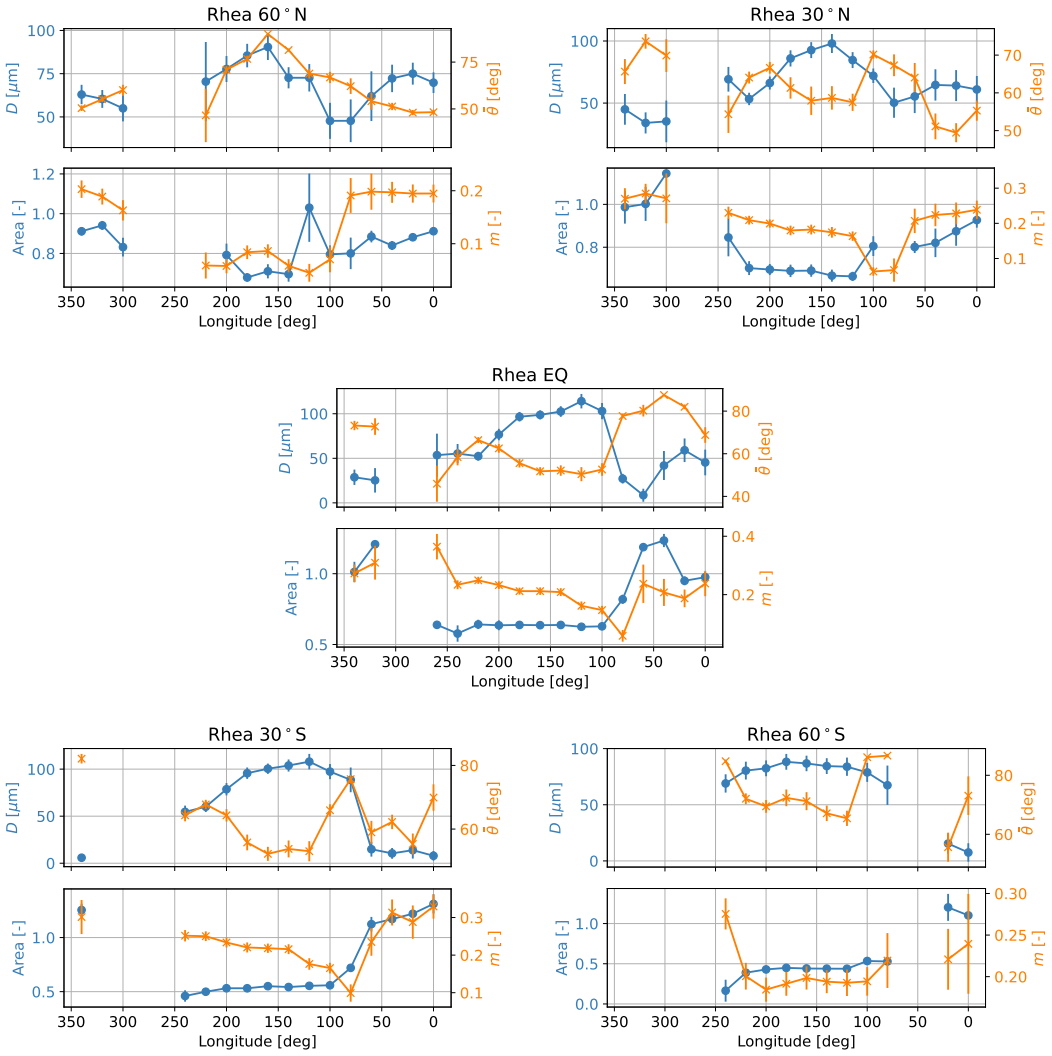

Figure 6.13: Averaged values of D, $\bar{\theta}$ normalized area of the 1.65-micron feature and m for the different longitudinal lines represented in Fig. 6.10. Fit data is presented in Appendix C.

which triggers chemical reactions that disrupt crystalline lattices and alter the regolith's structure. The results on the Saturnian hemisphere suggest that the region is affected by the processes taking place at both leading and trailing; yet, to a lesser extent.

A peculiarity is that effective roughness reaches a maximum at the anti-Saturnian side at 60°N, contrary to all other latitudes. This increase in effective roughness may be linked to local features, as this area displays two considerably large and degraded impact craters. However, further analysis is needed to assess this hypothesis.

6.3.2. Dione

The available data offers a greater coverage of Dione's surface than the one of Rhea, presenting also fewer pixels in the trailing hemisphere. The results are presented in Fig. 6.14.

Grain size and effective roughness are anti-correlated for all latitudes. Two overall regions of larger D are observed, an area of larger grains between 0 and 200°W, and a region of smaller values between 200 and 360°W. $\bar{\theta}$ reaches a clear maximum at 100°W and a minimum at anti-Saturnian. The dark terrain has the greatest value of $\bar{\theta}$ and m, and the lowest of D, which is consistent with the results of Rhea.

Dione experiences a greater flux of E-ring bombardment than Rhea, which translates into an abrupt

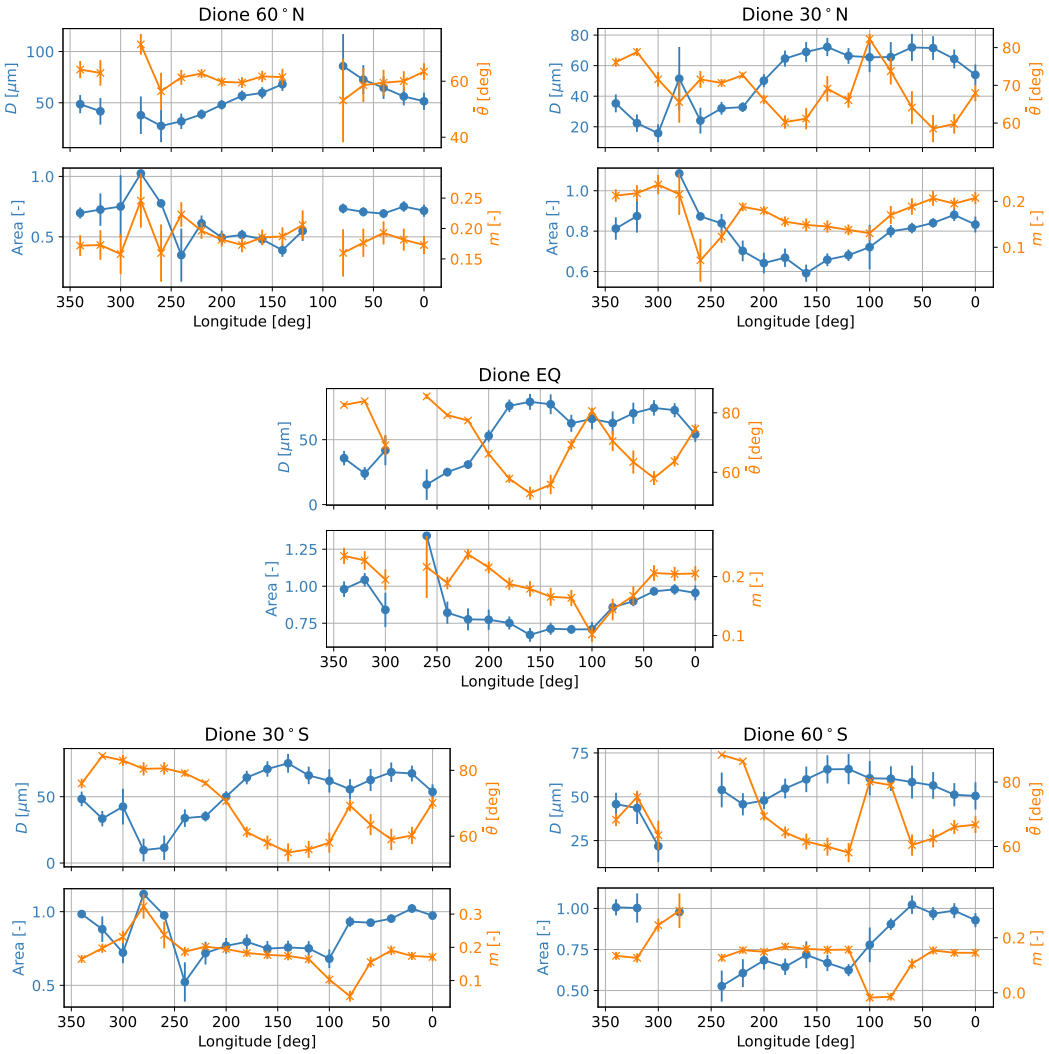

Figure 6.14: Averaged values of D, $\bar{\theta}$ normalized area of the 1.65-micron feature and m for the different longitudinal lines represented in Fig. 6.11. Fit data is presented in Appendix C.

increase in $\bar{\theta}$ and a reduction of m and D at the leading hemisphere. The differences between the minimum reached trailing and leading in D show how E-ring particle deposition does not have as strong an influence in reducing grain size as the impact of plasma.

Notably, m reaches a minimum at 30° N 260° W, which shows a few impact craters and bright ridges despite being in the dark terrain, which presents an overall greater presence of amorphous ice. At greater latitudes, the surface is more crystalline, with some longitudes of 60°S even displaying negative values of m, as was the case with pure crystalline experimental data analyzed in Section 5.2.2.

6.3.3. Enceladus

The coverage of the surface of Enceladus is much higher than in Dione and Rhea. As is the case for the rest of the icy moons, there are fewer pixels in the trailing hemisphere. The results are shown in Fig. 6.15.

As shown in Section 2.2.3, particle deposition rates from the plumes depend on grain size. According to numerical models, plume ejecta fall mostly on the southern region, and smaller particles reach higher particles between 0 and 90°W and at around 200°. This is consistent with the observed increase in D and m in the leading hemisphere. However, this behavior is not observed at 200°W; yet, at 240°,

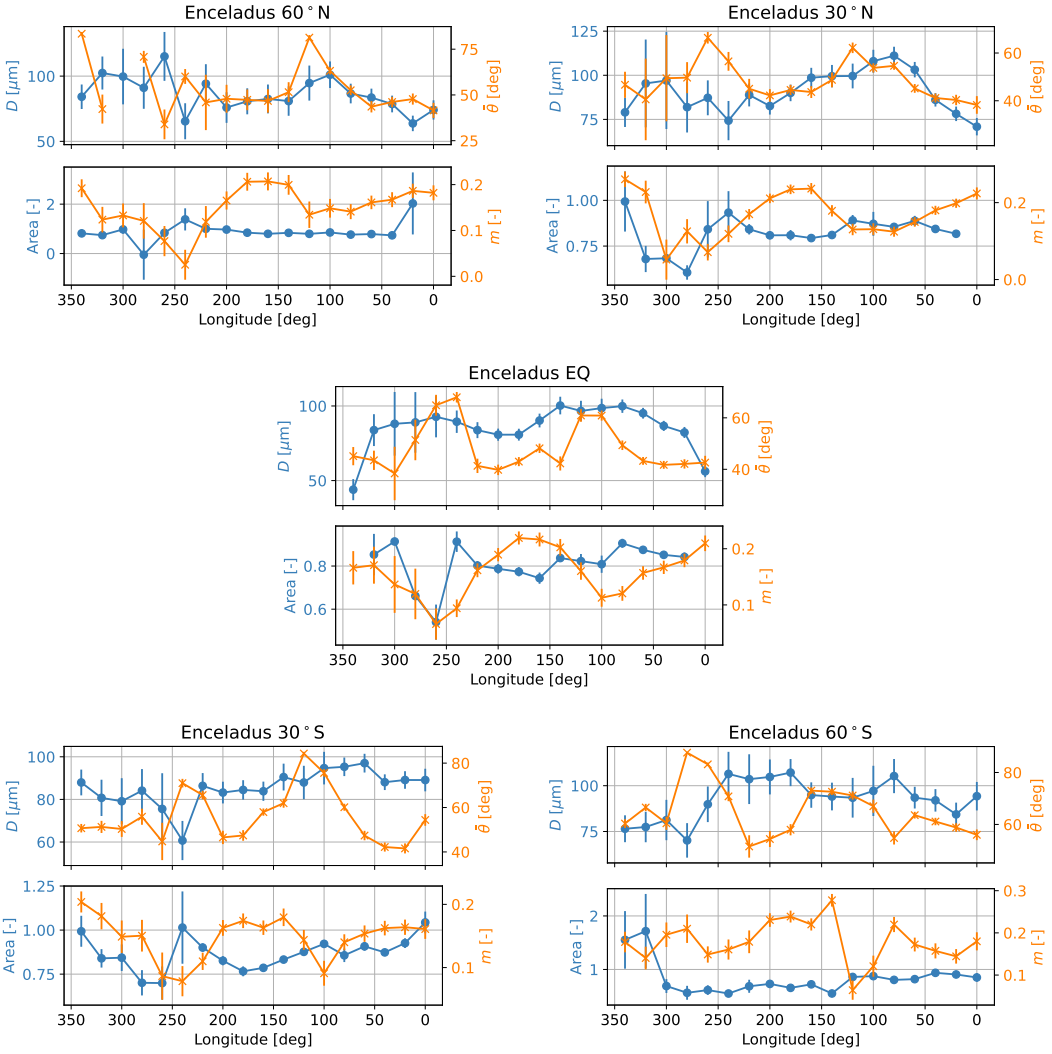

Figure 6.15: Averaged values of D, $\bar{\theta}$ normalized area of the 1.65-micron feature and m for the different longitudinal lines represented in Fig. 6.12. Fit data is presented in Appendix C.

especially at southern latitudes.

Enceladus' trailing hemisphere is also affected by plasma impacts; however, results show a greater presence of crystalline ice, contrary to the other moons. This may be a result of constant resurfacing and tectonics, as this region shows prominent ridges and fractures. The southern terrain of Enceladus shows the greatest presence of amorphous ice, in agreement with the terrain study.

6.4. Comparative study

In this section, the different hemispheres and poles of the different moons are compared. Note that for Rhea there are no pixels at 90° S, for Dione there are none for either 90° S or 90° N, and for Enceladus, there are none at 90° N. In these cases, the latitudes closest to the poles with a significant amount of pixels are selected. Then, the areas selected to represent the poles are the following: Rhea 70° S 180° W with 11 pixels; Dione 70° N 0° with 6 pixels and 70° S 180° W with 9 pixels; and Enceladus 80° N 0° W with 6 pixels. Furthermore, no pixels are located in the trailing hemisphere of Rhea; hence, 260° W is selected for trailing with one pixel. The obtained parameters (D, $\bar{\theta}$, m and area) along the equatorial lines are shown in Fig. 6.16, while the values of the poles are shown in Fig. 6.17. The estimated values can be found in Appendix C together with their associated uncertainties.

The trends within moons that were observed in the longitudinal study are also observed in Fig. 6.16:

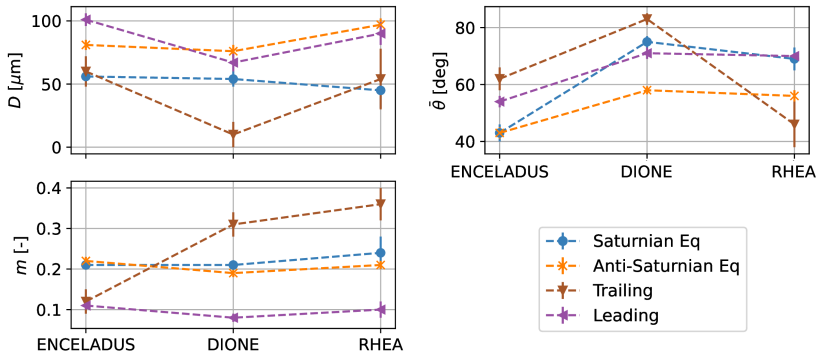

Figure 6.16: Averaged values of D, $\bar{\theta}$ and m for different terrains of Enceladus, Dione, and Rhea. The data is presented in Appendix C.

anti-correlation between D and $\bar{\theta}$, larger grains and smoother terrain at leading and greater abundance of amorphous ice at trailing.

As expected, the leading hemisphere of Enceladus displays the largest grains due to plume deposition. Dione's leading hemisphere exhibits smaller grains than Rhea's, as it orbits closer to Enceladus and experiences a greater flux of E-ring particles [37]. A subtle increase in m can be seen between Dione and Rhea in their leading hemispheres. This increase in amorphous ice abundance can be related to a smaller flux of E-ring particles.

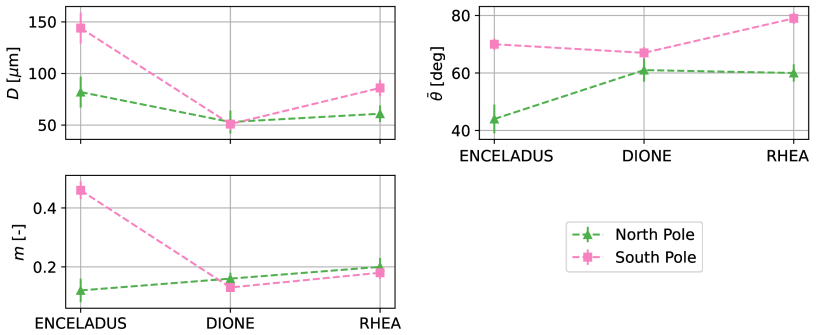

Figure 6.17: Averaged values of D, $\bar{\theta}$ and m of the northern and southern terrain of Enceladus, Dione, and Rhea. The data is presented in Appendix C.

Furthermore, trailing hemispheres should be less affected by rotating plasma and energetic particles as the moons orbit further away from Saturn. There is a clear trend of increasing m as moons orbit further away. Two phenomena are associated with the formation of dark terrain: plasma impacts and exogenic dark material coming from Phoebe [4]. The fact that m increases in the trailing hemisphere as the moon orbits further away supports the bombardment of dust coming from Phoebe. This finding is consistent with previous results pointing toward a greater abundance of tholins in Rhea than in Dione [14].

The behavior presented in Fig. 6.17 of the moons' northern hemispheres' is comparable to those of the Saturnian or anti-Saturnian hemispheres, as in-between regions with no dominant exogenic process. However, their south poles show a unique trend of $\bar{\theta}$ and m, especially due to the active southern terrain of Enceladus.

7

Conclusions

In light of the results presented in previous chapters, the research questions are revisited to evaluate how they have been answered throughout this work. First, answers to the research subquestions are presented to then provide an answer to the main research question.

A. *What are the challenges and limitations of applying the Hapke model to icy moon regolith?*

The primary challenge lies in the existing correlations between the considered Hapke parameters (grain size, D, surface roughness, $\bar{\theta}$, filling factor, ϕ, and the phase function asymmetry parameter, b). This directly impacts the convergence of the fitting process, leading to greater uncertainties when attempting to fit more than two parameters. Additionally, an overestimation of grain size for the sample with the smallest particles is observed, aligning with findings from prior studies [55, 65]. This indicates that the values of D cannot be considered an absolute predictor of particle grain size, but rather as an estimator of the trend in grain size evolution across different terrains.

On a different note, when the filling factor is treated as a constant parameter, $\bar{\theta}$ encompasses the impact of changes in porosity. Consequently, it is interpreted as an effective surface roughness.

B. *Which techniques can be used to estimate the degree of crystallinity using VIMS data?*

To evaluate the crystallinity of a given sample, four different approaches are examined using experimental data and simulated spectra: the mass fraction of amorphous ice fit using the Hapke model's intimate mixing formulation, the location of the 2-micron feature, an area analysis of the 1.65-micron feature, and the 1.2-1.65 ratio.

The mass fraction fit did not yield accurate estimations of ice morphology due to the model's assumptions and the minimal impact this parameter has on the spectrum. On the other hand, the location of the 2-micron feature appears as a reliable estimator of crystallinity. Previous studies demonstrated a gradual shift in this feature, pointing toward a new method for estimating the percentage of amorphous ice in a given sample [61, 3].

Numerical simulations indicated that after normalization using a purely crystalline spectrum with the same characteristics, the area around the 1.65-micron feature becomes an estimator of the amount of amorphous ice. However, this approach lacks VIMS data points around the feature, limiting its insights into the crystallinity state of the icy regolith. More experimental data including mixtures of amorphous and crystalline ice are necessary to address the performance of this technique beyond numerical simulations. Lastly, despite its use in prior studies [26], the 1.2-1.65 micron ratio was considered too sensitive to other regolith characteristics to be a reliable indicator of crystallinity.

C. *What are the regolith characteristics of different terrain units within the icy moons?*

Fig. 7.1 encapsulates the effects of recent impacts like Inktomi in Rhea and Creusa in Dione, compared to nearby terrain. The craters and ray patterns show an increase in grain size and crystallinity. This suggests that the dominant effect on these features is crystallization resulting from the release of thermal energy after the impact. In particular, Inktomi, being more crystalline and having larger particles than Creusa, supports the utilization of crystallinity and grain size as age indicators of craters.

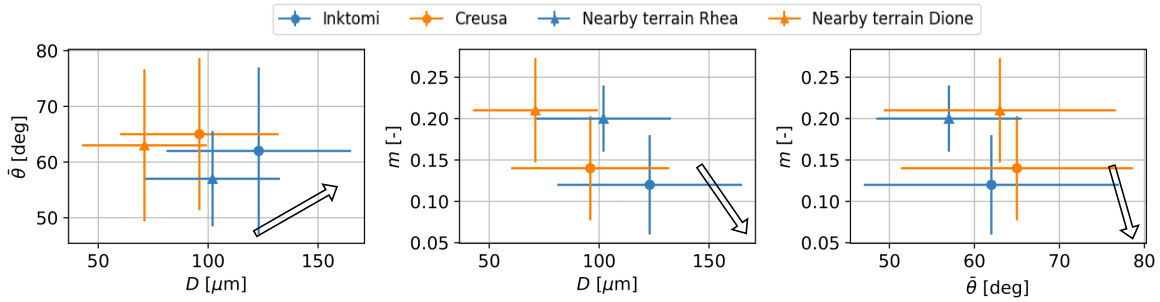

Figure 7.1: Regolith characteristics of impact craters Inktomi and Creusa compared with nearby terrain. The black arrow represents the effect of the impact on the icy terrain.

In Rhea and Dione's trailing hemisphere, rougher terrains with more amorphous and smaller grains are observed. Fractures and craters in Dione's wispy terrain exhibit an increase in grain size, smoother terrain, and more crystalline ice. This is attributed to new material emerging from deeper layers that have not been altered by prolonged exposure to plasma.

Examining Enceladus, ridges in its Saturnian hemisphere show an increase in grain size and roughness without any observed significant difference in crystallinity. Conversely, Enceladus' tiger stripes display the largest observed grains and roughest terrain, following the stripes' geologic activity. Additionally, there is a greater abundance of crystalline ice observed in the sulci, correlating with the increased temperatures recorded in those areas [15].

***D.** How do regolith characteristics vary across different regions of icy moons?*

Across the different moons, similar trends are observed. Particularly, an overall anti-correlation between grain size and effective surface roughness, as has been reported in previous studies [62].

In the case of Rhea and Dione, the anti-Saturnian side stands out with a peak in grain size, while the leading hemisphere undergoes changes that can be attributed to E-ring particle deposition, reducing grain size and altering the texture of the terrain. The trailing hemisphere is affected by co-rotating plasma bombardment, disrupting crystalline lattices and increasing the abundance of amorphous ice. Such dichotomy is shown in Fig. 7.2. The Saturnian hemisphere experiences the effect effects that take place at the leading and trailing processes but to a lesser extent. Their anti-Saturnian hemisphere showcases a maximum grain size, a minimum surface roughness, and an in-between value for the abundance of amorphous ice.

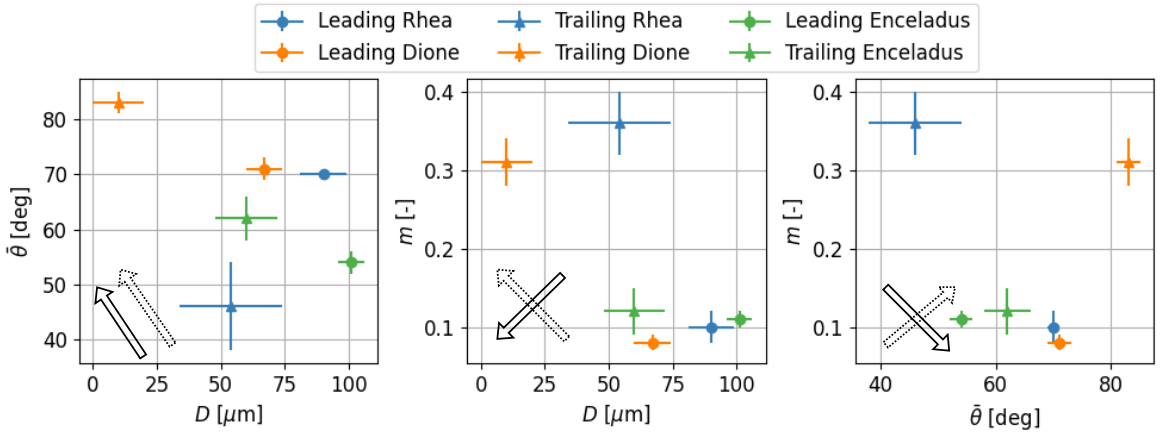

Figure 7.2: Regolith characteristics of the trailing and leading hemispheres of Dione, Rhea and Enceladus. The solid arrow represents the effect of plume deposition and E-ring bombardment, while the dotted line represents the effect of plasma.

In the case of Enceladus, plume deposition models in Enceladus align with the observed increase in grain size and the abundance of amorphous ice in the leading hemisphere. Notably, Enceladus' trailing hemisphere exhibits a greater presence of crystalline ice, possibly due to continuous resurfacing and tectonic activity, evident in prominent ridges and fractures. Fig. 7.2 also represents the geologic uniqueness of Enceladus, compared to the rest of the icy moons.

E. *How do the regolith characteristics change between different icy moons?*

Despite being closer to Enceladus, Dione's leading side has smaller grains than Rhea's. The higher presence of amorphous ice in the leading hemispheres of Dione and Rhea can be linked to E-ring particles spending more time in orbit. As moons orbit farther from Saturn, their trailing hemispheres are less affected by rotating plasma and energetic particles. Consequently, there is a noticeable pattern of increasing amorphous ice abundance with distance. However, the results also support the exogenic origin of Dione's and Rhea's dark material, as this pattern aligns with earlier observations of higher tholin abundance in Rhea than in Dione [4].

How do exogenic surface processes affect the regolith characteristics on the icy moons?

In light of the results displayed throughout this work and the answers provided to the subquestions, the main research question of this work can be tackled. The influence of the processes is summarized in Table 7.1.

Meteoroid impacts are associated with increased grain size and crystallinity in the crater and ray pattern of fresh material. This material is exposed to space weathering from cosmic rays and other exogenic processes depending on where it is situated, increasing the abundance of amorphous ice and reducing the grain size. E-ring deposition and plasma bombardment increase the effective roughness of the surfaces and decrease their grain size, especially plasma bombardment. Terrain affected by the impact of corotating plasma has a greater abundance of amorphous ice while E-ring bombardment acts in the opposite direction. Resurfacing caused by tectonic movement in Enceladus is associated with the exposition of uncovered material, leading to an increase in grain size, and crystallinity and a decrease in surface roughness. Furthermore, crystallinity estimations of the same terrain point toward a possible change in the abundance of amorphous ice due to solar irradiation during Enceladus' rotation.

Table 7.1: Effect of the main exogenic processes on the icy regolith characteristics.

	Grain size D	Surface roughness $\bar{\theta}$	Mass fraction of amorphous ice m
E-ring bombardment	$\downarrow$	$\uparrow$	$\downarrow$
Meteroid impacts	$\uparrow$	-	$\downarrow$
Plasma bombardment	$\downarrow\downarrow$	$\uparrow$	$\uparrow$
Ridges	$\uparrow$	$\downarrow$	$\uparrow$

7.1. Recommendations and future work

The results presented in this thesis open the door for several areas of further research that would serve to improve our understanding of regolith characteristics and surface processes taking place in the icy moons, especially to prepare the ground for the results of JUICE. They can be divided into two fields: the development of experimental data and the expansion of the study of VIMS data.

First, measuring reflectance spectra of icy regolith samples with different crystallinity states is essential to assessing how crystallinity can be inferred. Furthermore, developing spectral measurements of icy samples at a non-vanishing phase angle with grain sizes comparable to the ones found in the icy moons would further the understanding of the Hapke model's limitations. To see what happens with the regolith after an impact, a thermodynamics study of the vaporized material should be carried out.

Regarding VIMS data cubes, this work could be extended to cover more Saturnian satellites. Iapetus in particular shows a prominent dichotomy between its hemispheres, more pronounced than the ones in Rhea and Dione. By extracting the surface characteristics of its dark terrain and comparing them to the ones found in Rhea and Dione, light could be shed on the origin of this material and how the effect of plasma interactions is paired with the deposition of exogenic material. Extending the data source from Nantes' portal would be beneficial, as it does not include the cubes with the highest resolutions. Cubes used in previous studies [13] resolve the crater edges and central peak. Analyzing the regolith characteristics to such a level would help in understanding the importance of the two phenomena taking place after an impact: the melting of material and the vaporization (and later deposition) of the uppermost layers. Furthermore, the area study around the 1.65-micron feature for crystallinity was hindered due to the lack of sensitivity of VIMS. James Webb Space Telescope has a better spectral resolution; hence, the area method for crystallinity estimation could be applied to James Webb Space

Telescope observations of icy moons. Moreover, the variation in amorphous ice at the Enceladean anti-Saturnian side should be studied further. Using Spice kernels, the actual irradiation time could be obtained. This could assess the hypothesis of these changes in crystallinity.

References

[1] Anne J Verbiscer et al. “Surface properties of Saturn’s icy moons from optical remote sensing”. In: *Enceladus and the Icy Moons of Saturn* 10 (2018).

[2] VJ Bray, T Öhman, and H Hargitai. “Central Peak Crater”. In: *), Encyclopedia of planetary landforms* (2014), p. 44.

[3] Gianrico Filacchione et al. “Saturn’s icy satellites investigated by Cassini-VIMS. V. Spectrophotometry”. In: *Icarus* 375 (2022), p. 114803.

[4] Amanda R Hendrix et al. “Icy Saturnian satellites: Disk-integrated UV-IR characteristics and links to exogenic processes”. In: *Icarus* 300 (2018), pp. 103–114.

[5] Jack J Lissauer and Imke De Pater. *Fundamental planetary science: physics, chemistry and habitability*. Cambridge University Press, 2013.

[6] Linda Spilker. “Cassini-Huygens’ exploration of the Saturn system: 13 years of discovery”. In: *Science* 364.6445 (2019), pp. 1046–1051.

[7] DG Mitchell et al. “The dynamics of Saturn’s magnetosphere”. In: *Saturn from Cassini-Huygens*. Springer, 2009, pp. 257–279.

[8] Matija Ćuk and Maryame El Moutamid. “Three-body Resonances in the Saturnian System”. In: *The Astrophysical Journal Letters* 926.2 (2022), p. L18.

[9] Katrin Stephan et al. “The Saturnian satellite Rhea as seen by Cassini VIMS”. In: *Planetary and Space Science* 61.1 (2012), pp. 142–160.

[10] Paul Schenk et al. “The anatomy of fresh complex craters on the mid-sized icy moons of Saturn and self-secondary cratering at the rayed crater Inktomi (Rhea)”. In: *Meteoritics & Planetary Science* 55.11 (2020), pp. 2440–2460.

[11] Roger N Clark et al. “Compositional mapping of Saturn’s satellite Dione with Cassini VIMS and implications of dark material in the Saturn system”. In: *Icarus* 193.2 (2008), pp. 372–386.

[12] F Scipioni et al. “Spectroscopic classification of icy satellites of Saturn II: Identification of terrain units on Rhea”. In: *Icarus* 234 (2014), pp. 1–16.

[13] Cristina M Dalle Ore et al. “Impact craters: An ice study on Rhea”. In: *Icarus* 261 (2015), pp. 80–90.

[14] Gianrico Filacchione et al. “Saturn’s icy satellites and rings investigated by Cassini–VIMS: III–Radial compositional variability”. In: *Icarus* 220.2 (2012), pp. 1064–1096.

[15] Gianrico Filacchione et al. “Saturn’s icy satellites investigated by Cassini-VIMS. IV. Daytime temperature maps”. In: *Icarus* 271 (2016), pp. 292–313.

[16] Katrin Stephan et al. “Dione’s spectral and geological properties”. In: *Icarus* 206.2 (2010), pp. 631–652.

[17] F Scipioni et al. “Spectroscopic classification of icy satellites of Saturn I: Identification of terrain units on Dione”. In: *Icarus* 226.2 (2013), pp. 1331–1349.

[18] Naoyuki Hirata and Hideaki Miyamoto. “Rayed craters on Dione: Implication for the dominant surface alteration process”. In: *Icarus* 274 (2016), pp. 116–121.

[19] John R Spencer and Francis Nimmo. “Enceladus: An active ice world in the Saturn system”. In: *Annual Review of Earth and Planetary Sciences* 41 (2013), pp. 693–717.

[20] Michael T Bland et al. “Enceladus’ extreme heat flux as revealed by its relaxed craters”. In: *Geophysical Research Letters* 39.17 (2012).

[21] John R Spencer et al. “Enceladus: An active cryovolcanic satellite”. In: *Saturn from Cassini-Huygens* (2009), pp. 683–724.

[22] G Wesley Patterson et al. “The geology of Enceladus”. In: *Enceladus and the icy moons of Saturn* (2018), p. 95.

[23] Jean-Philippe Combe et al. “Nature, distribution and origin of CO2 on Enceladus”. In: *Icarus* 317 (2019), pp. 491–508.

[24] Carolyn C Porco et al. “Cassini observes the active south pole of Enceladus”. In: *science* 311.5766 (2006), pp. 1393–1401.

[25] R Jaumann et al. “Distribution of icy particles across Enceladus’ surface as derived from Cassini-VIMS measurements”. In: *Icarus* 193.2 (2008), pp. 407–419.

[26] Robert H Brown et al. “Composition and physical properties of Enceladus’ surface”. In: *Science* 311.5766 (2006), pp. 1425–1428.

[27] Benjamin Ou-Yang and RM Mastrapa. “Ammonia on Enceladus”. In: *American Astronomical Society Meeting Abstracts# 215*. Vol. 215. 2010, pp. 448–17.

[28] S Andersson and EF Van Dishoeck. “Photodesorption of water ice-A molecular dynamics study”. In: *Astronomy & Astrophysics* 491.3 (2008), pp. 907–916.

[29] Frank Postberg et al. “Plume and surface composition of Enceladus”. In: *Enceladus and the icy moons of Saturn* (2018), pp. 129–162.

[30] Ben S Southworth, Sascha Kempf, and Joe Spitale. “Surface deposition of the Enceladus plume and the zenith angle of emissions”. In: *Icarus* 319 (2019), pp. 33–42.

[31] CJ Hansen et al. “The composition and structure of Enceladus’ plume from the complete set of Cassini UVIS occultation observations”. In: *Icarus* 344 (2020), p. 113461.

[32] Edwin S Kite and Allan M Rubin. “Sustained eruptions on Enceladus explained by turbulent dissipation in tiger stripes”. In: *Proceedings of the National Academy of Sciences* 113.15 (2016), pp. 3972–3975.

[33] JR Spencer et al. “Plume origins and plumbing: from ocean to surface”. In: *Enceladus and the icy moons of Saturn* (2018), pp. 163–174.

[34] N Khawaja et al. “Low-mass nitrogen-, oxygen-bearing, and aromatic compounds in Enceladean ice grains”. In: *Monthly Notices of the Royal Astronomical Society* 489.4 (2019), pp. 5231–5243.

[35] Sascha Kempf, Uwe Beckmann, and Jürgen Schmidt. “How the Enceladus dust plume feeds Saturn’s E ring”. In: *Icarus* 206.2 (2010), pp. 446–457.

[36] Andrew P Ingersoll and Shawn P Ewald. “Total particulate mass in Enceladus plumes and mass of Saturn’s E ring inferred from Cassini ISS images”. In: *Icarus* 216.2 (2011), pp. 492–506.

[37] Anne Verbiscer et al. “Enceladus: Cosmic graffiti artist caught in the act”. In: *Science* 315.5813 (2007), pp. 815–815.

[38] Raúl A Baragiola. “Water ice on outer solar system surfaces: Basic properties and radiation effects”. In: *Planetary and Space Science* 51.14-15 (2003), pp. 953–961.

[39] G Strazzulla et al. “Primordial comet mantle: Irradiation production of a stable organic crust”. In: *Icarus* 91.1 (1991), pp. 101–104.

[40] Marla H Moore and Reggie L Hudson. “Far-infrared spectral studies of phase changes in water ice induced by proton irradiation”. In: *Astrophysical Journal, Part 1 (ISSN 0004-637X), vol. 401, no. 1, p. 353-360.* 401 (1992), pp. 353–360.

[41] Sarah T Stewart, Achim Seifter, and Andrew W Obst. “Shocked H2O ice: Thermal emission measurements and the criteria for phase changes during impact events”. In: *Geophysical Research Letters* 35.23 (2008).

[42] Barbara H Stuart. *Infrared spectroscopy: fundamentals and applications*. John Wiley & Sons, 2004.

[43] KM Smith and DA Newnham. “Near-infrared absorption spectroscopy of oxygen and nitrogen gas mixtures”. In: *Chemical physics letters* 308.1-2 (1999), pp. 1–6.

[44] Ely Eugene Bell. “Optical constants and their measurement”. In: *Light and Matter Ia/Licht und Materie Ia*. Springer, 1967, pp. 1–58.

[45] RM Waxler and CE Weir. “Effect of pressure and temperature on the refractive indices of benzene, carbon tetrachloride, and water”. In: *Journal of research of the National Bureau of Standards. Section A, Physics and chemistry* 67.2 (1963), p. 163.

[46] WRM Rocha and S Pilling. “Determination of optical constants n and k of thin films from absorbance data using Kramers–Kronig relationship”. In: *Spectrochimica Acta Part A: Molecular and Biomolecular Spectroscopy* 123 (2014), pp. 436–446.

[47] Thomas C Hansen. “The everlasting hunt for new ice phases”. In: *Nature Communications* 12.1 (2021), pp. 1–3.

[48] Thorsten Bartels-Rausch et al. “Ice structures, patterns, and processes: A view across the icefields”. In: *Reviews of Modern Physics* 84.2 (2012), p. 885.

[49] J Stern and T Loerting. “Crystallisation of the amorphous ices in the intermediate pressure regime”. In: *Scientific reports* 7.1 (2017), pp. 1–10.

[50] Akira Kouchi and Toshio Kuroda. “Amorphization of cubic ice by ultraviolet irradiation”. In: *Nature* 344.6262 (1990), pp. 134–135.

[51] GA Baratta et al. “The 3.1 microns feature in ion-irradiated water ice”. In: *Astronomy and Astrophysics (ISSN 0004-6361), vol. 252, no. 1, Dec. 1991, p. 421-424. Research supported by ASI.* 252 (1991), pp. 421–424.

[52] P Jenniskens and DF Blake. “Crystallization of amorphous water ice in the solar system”. In: *The Astrophysical Journal* 473.2 (1996), p. 1104.

[53] Stephen G Warren. “Optical properties of ice and snow”. In: *Philosophical Transactions of the Royal Society A* 377.2146 (2019), p. 20180161.

[54] RM Mastrapa et al. “Optical constants of amorphous and crystalline H2O-ice: 2.5–22 μm (4000–455 cm- 1) optical constants of H2O-ice”. In: *The Astrophysical Journal* 701.2 (2009), p. 1347.

[55] Bruce Hapke. *Theory of reflectance and emittance spectroscopy*. Cambridge university press, 2012.

[56] Antoine Pommerol et al. “Experimenting with mixtures of water ice and dust as analogues for icy planetary material”. In: *Space science reviews* 215.5 (2019), pp. 1–68.

[57] Ines Belgacem. “Etude photométrique des lunes glacées de Jupiter”. Theses. Université Paris Saclay (COmUE), Nov. 2019. URL: `https://theses.hal.science/tel-02421378`.

[58] Louis G Henyey and Jesse Leonard Greenstein. “Diffuse radiation in the galaxy”. In: *Astrophysical Journal, vol. 93, p. 70-83 (1941).* 93 (1941), pp. 70–83.

[59] O. Fryer. “Spectral modeling of Cassini-VIMS data to investigate the surface properties of Enceladus”. MA thesis. TU Delft, 2021.

[60] Audrey F McGuire and Bruce W Hapke. “An experimental study of light scattering by large, irregular particles”. In: *Icarus* 113.1 (1995), pp. 134–155.

[61] RM Mastrapa et al. “Optical constants of amorphous and crystalline H2O-ice in the near infrared from 1.1 to 2.6 μm”. In: *Icarus* 197.1 (2008), pp. 307–320.

[62] Michael K Shepard and Paul Helfenstein. “A test of the Hapke photometric model”. In: *Journal of Geophysical Research: Planets* 112.E3 (2007).

[63] Bruce Hapke. “Bidirectional reflectance spectroscopy: 5. The coherent backscatter opposition effect and anisotropic scattering”. In: *Icarus* 157.2 (2002), pp. 523–534.

[64] Michael K Shepard. *Introduction to planetary photometry*. Cambridge University Press, 2017.

[65] M Ciarniello et al. “Hapke modeling of Rhea surface properties through Cassini-VIMS spectra”. In: *Icarus* 214.2 (2011), pp. 541–555.

[66] G Filacchione et al. “Saturn’s icy satellites investigated by Cassini–VIMS: II. Results at the end of nominal mission”. In: *Icarus* 206.2 (2010), pp. 507–523.

[67] Roger N Clark et al. “The surface composition of Iapetus: Mapping results from Cassini VIMS”. In: *Icarus* 218.2 (2012), pp. 831–860.

[68] Robert H Brown et al. “The Cassini visual and infrared mapping spectrometer (VIMS) investigation”. In: *Space Science Reviews* 115.1 (2004), pp. 111–168.

[69] NASA/JPL. *CASSINI FINAL MISSION REPORT: Visible and Infrared Spectrometer*. https://atmos.nmsu.edu/~itrejo/Cassini/Cassini/Cassini_Final_RPT/Cassssini%20Final%20Rpt%202019_Vol%201%20-%20VIMSsdpdf%20%5bpreview%5d.pdf. Accessed: 10/10/2023. 2019.

[70] R.H. Brown et al. “The Cassini Visual Infrared Mapping Spectrometer.” In: vol. 2803. Jan. 1996, pp. 19–20.

[71] Rozenn Robidel et al. “Photometrically-corrected global infrared mosaics of Enceladus: New implications for its spectral diversity and geological activity”. In: *Icarus* 349 (2020), p. 113848.

[72] H Sato et al. “Resolved Hapke parameter maps of the Moon”. In: *Journal of Geophysical Research: Planets* 119.8 (2014), pp. 1775–1805.

[73] Jorge Nocedal and Stephen J Wright. *Numerical optimization*. Springer, 1999.

[74] Katrin Stephan et al. “VIS-NIR/SWIR spectral properties of H2O ice depending on particle size and surface temperature”. In: *Minerals* 11.12 (2021), p. 1328.

[75] CJA Howett et al. “Thermal properties of Rhea’s poles: Evidence for a meter-deep unconsolidated subsurface layer”. In: *Icarus* 272 (2016), pp. 140–148.

[76] Amanda R Hendrix et al. “Mimas’ far-UV albedo: Spatial variations”. In: *Icarus* 220.2 (2012), pp. 922–931.

[77] I. Boshuizen. “James Webb Space Telescope observations to study Ganymede’s surface properties”. MA thesis. TU Delft, 2023.

[78] S Shaphiro and MBJB Wilk. “An analysis of variance test for normality”. In: *Biometrika* 52.3 (1965), pp. 591–611.

[79] Nornadiah Mohd Razali, Yap Bee Wah, et al. “Power comparisons of shapiro-wilk, kolmogorov-smirnov, lilliefors and anderson-darling tests”. In: *Journal of statistical modeling and analytics* 2.1 (2011), pp. 21–33.

[80] J Royston. “A remark on algorithm AS-181-The W test for normality (Algorithm R94)”. In: *J Appl Stat* 44.4 (1995), pp. 547–551.

A

Statistics

A.1. Shapiro-Wilk test for data normality

The Shapiro-Wilk test is a statistical test used to assess whether a given dataset follows a Gaussian (normal) distribution [78, 79]. The null hypothesis (H_0) of the Shapiro-Wilk test assumes that the data is normally distributed, while the alternative hypothesis (H_1) suggests that the data significantly deviates from a normal distribution. The test statistic is calculated based on the sample data and is compared to a critical value to make a decision about the data's distribution. If the test statistic is significantly different from the expected value under the assumption of a normal distribution, the null hypothesis is rejected.

The Shapiro-Wilk test is based on the following test statistic:

$$W = \frac{\left(\sum_{i=1}^{n} a_i x_{(i)}\right)^2}{\sum_{i=1}^{n}(x_i - \bar{x})^2}, \tag{A.1}$$

where n is the sample size, $x_{(i)}$ represents the ordered sample values, $\bar{x}$ is the sample mean, and a_i are constants that depend on the sample size. The test statistic W is compared against critical values from tables or calculated p-values to determine the statistical significance. If the p-value is less than the chosen significance level $\alpha = 0.05$ for this study), the null hypothesis is rejected, indicating that the data does not follow a Gaussian distribution. Conversely, if the p-value is greater than α, the null hypothesis is not rejected, suggesting that the data may be approximately normally distributed.

However, the Shapiro-Wilk test has limitations and caveats when interpreting the results. The most relevant ones when interpreting the results from the icy moons' fits are [80]:

1. **Sample size**: The Shapiro-Wilk test is most effective for small to moderately-sized samples ($N < 2000$). With very large sample sizes, the test can become highly sensitive to minor deviations from normality.
2. **Outliers**: The test can be overly sensitive to outliers falling in the tails of the distribution. Then, the presence of a single outlier can lead to a rejection of the normality hypothesis.
3. **Uncertainty in data**: The Shapiro-Wilk test does not take into account the uncertainty in the data. Data points that fall outside normality, but whose errors lay within normality can lead to a p-value that rejects the hypothesis of normality.

A.2. Means and uncertainties

The average values of a dataset, $\bar{x}$, is computed as the sum of all data points divided by the number of data points in the set:

$$\bar{x} = \frac{1}{N}\sum_{i=1}^{N} x_i, \tag{A.2}$$

where N is the sample size (the number of data points), and x_i represents each individual data point. The standard error of the mean is calculated as the standard deviation, σ, of the dataset divided by the square root of the sample size,

$$SE = \frac{\sigma}{\sqrt{N}} \tag{A.3}$$

The standard error quantifies the spread of the data and provides an estimate of the precision of the mean.

A.2.1. Weighted average for data with associated uncertainty

In situations where each data point in a dataset has an associated uncertainty, calculating a weighted average provides a more accurate representation of the central tendency. The weighted average uses the inverse of each data point's uncertainty as weight. It is calculated as:

$$\bar{x}_w = \frac{\sum_{i=1}^{N} \frac{x_i}{\sigma_i^2}}{\sum_{i=1}^{N} \frac{1}{\sigma_i^2}}, \tag{A.4}$$

where $\bar{x}_w$ represents the weighted average, N is again the sample size, x_i represents each individual data point, and σ_i is the uncertainty associated with each data point.

The inverse-variance weighting takes into account the precision of each data point, giving more weight to data points with smaller uncertainties. The uncertainty associated with the weighted average is given, once again, by the standard error of the weighted mean. The standard error is expressed as,

$$SE = \sqrt{\frac{1}{\sum_{i=1}^{N} \frac{1}{\sigma_i^2}}} \tag{A.5}$$

B

Terrain study errors

In this appendix, the relative errors of the estimated parameters (D, $\bar{\theta}$ and m) from the terrain study (Section 6.2) are presented. The way uncertainties are calculated for the parameters coming from the Hapke model (D and $\bar{\theta}$) is described in Section 4.3.1 and the error of m is calculated following the method described in Section 5.2.2.

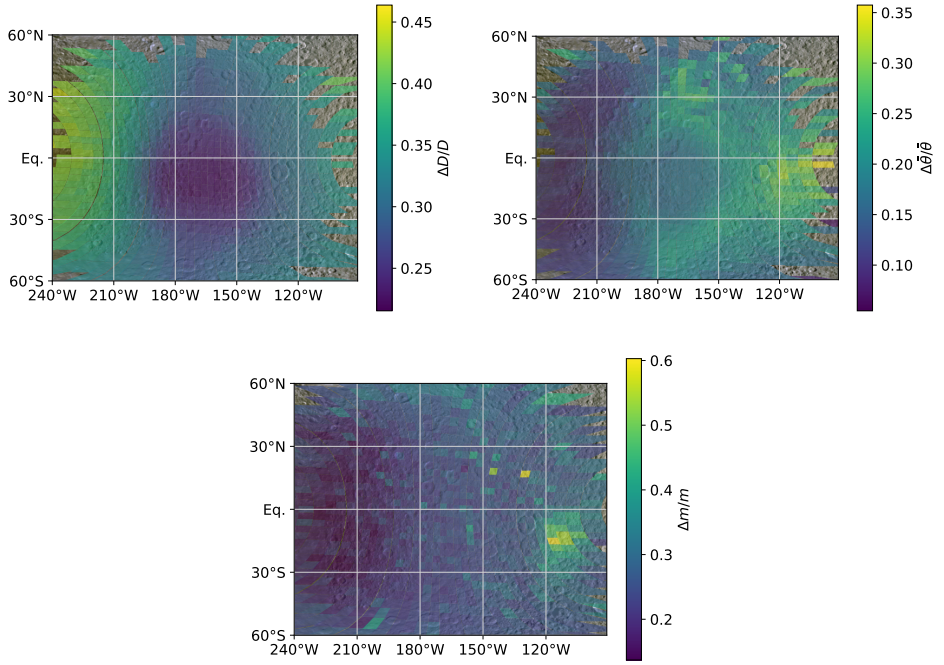

Figure B.1: Relative errors of D, $\bar{\theta}$ and m of Rhea's cube 1511726125_1, whose estimated values are shown in Fig. 6.4.

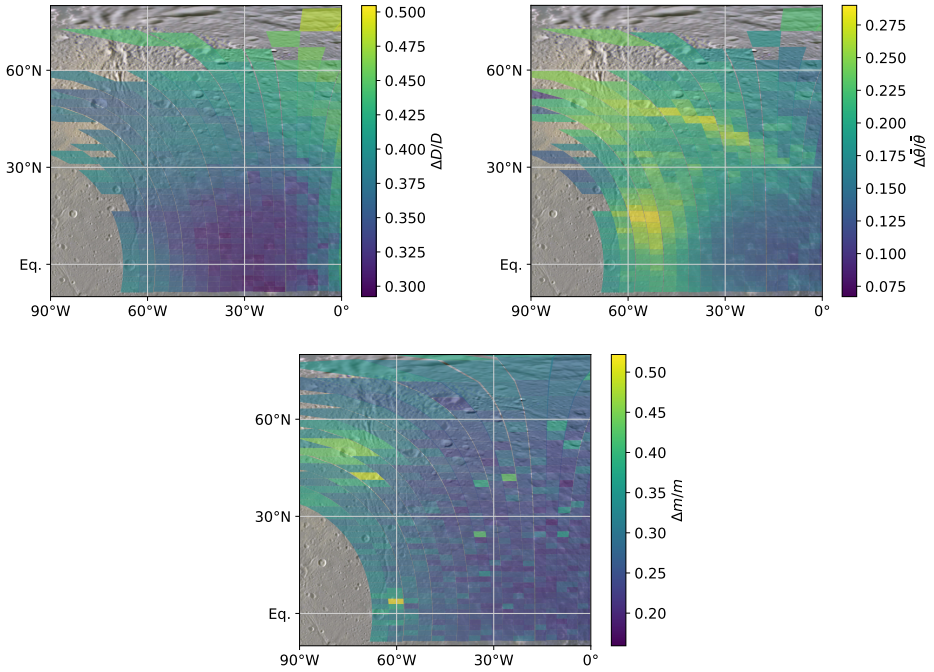

Figure B.2: Relative errors of D, $\bar{\theta}$ and m of Dione's cube 1649318884_1, which estimated values are shown in Fig. 6.5

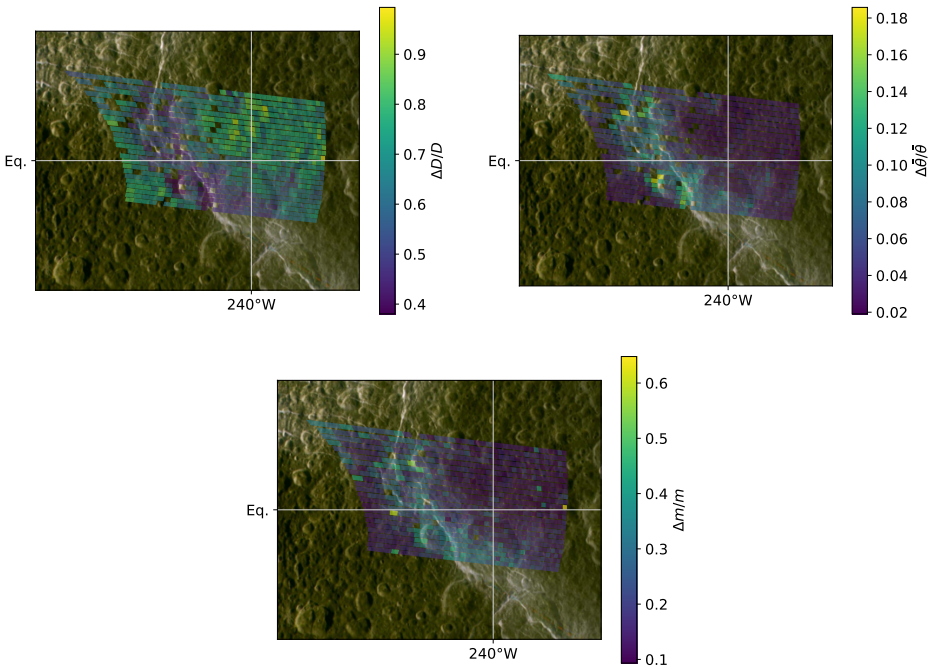

Figure B.3: Relative errors of D, $\bar{\theta}$ and m of Dione's cube 1507745050_1, which estimated values are shown in Fig. 6.6.

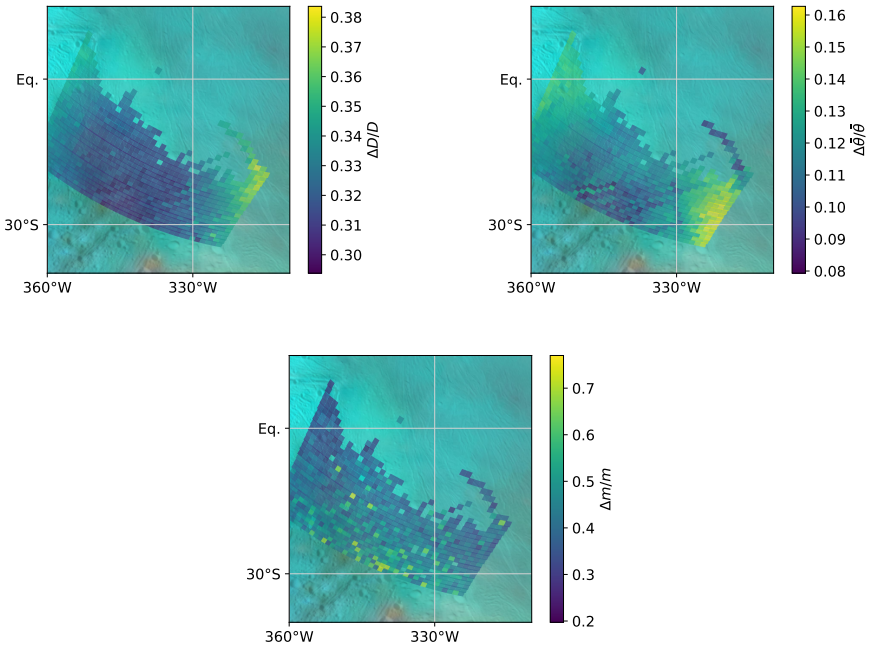

Figure B.4: Relative errors of D, $\bar{\theta}$ and m of Enceladus' cube 1829241298_1, which estimated values are shown in Fig. 6.7.

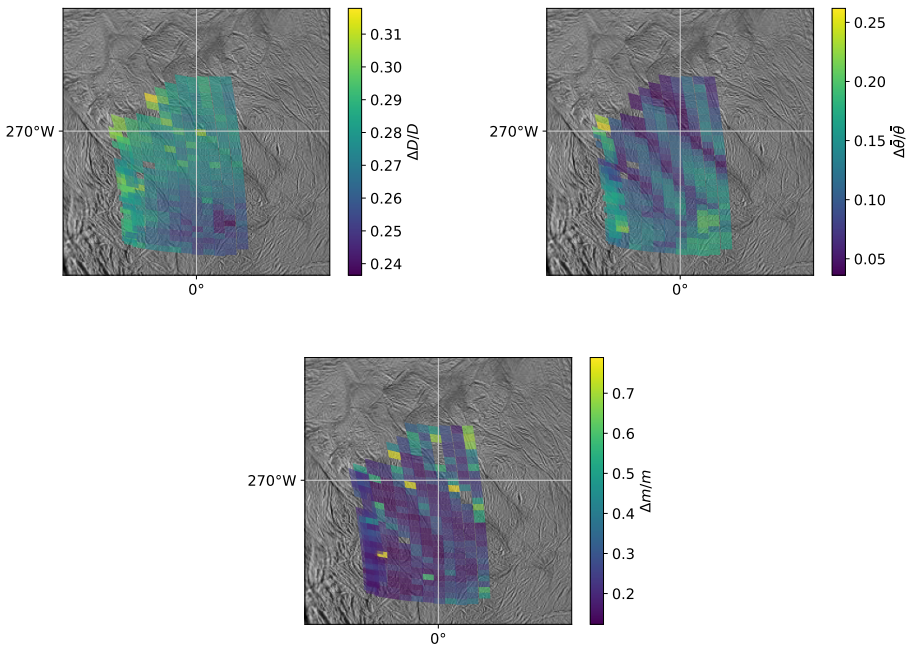

Figure B.5: Relative errors of D, $\bar{\theta}$ and m of Enceladus' cube 1500061286_1, which estimated values are shown in Fig. 6.8.

C

Longitudinal study coverage and results

This appendix shows the numerical results and uncertainties of the longitudinal study of Section 6.3. The uncertainties are calculated following the statistical method described in Section 6.1.

Table C.1: Rhea's longitudinal study values of D, $\bar{\theta}$, m and normalized partial area of the 1.65-micron feature at latitude 60°N.

Lon	Pix Area	# Pixels	D [μm]	$\bar{\theta}$ [deg]	Area [-]	m [-]
0	7272	14	70 ± 6	48 ± 1	0.91 ± 0.02	0.19 ± 0.02
20	7484	14	75 ± 6	48 ± 1	0.88 ± 0.01	0.19 ± 0.02
40	6199	10	72 ± 8	51 ± 2	0.84 ± 0.02	0.20 ± 0.02
60	4665	3	62 ± 14	54 ± 5	0.88 ± 0.03	0.20 ± 0.03
80	1212	3	48 ± 12	62 ± 4	0.80 ± 0.08	0.19 ± 0.03
100	3580	4	48 ± 10	67 ± 3	0.80 ± 0.05	0.07 ± 0.02
120	6626	12	73 ± 8	69 ± 3	1.0 ± 0.2	0.05 ± 0.02
140	5558	24	73 ± 6	81 ± 1	0.70 ± 0.04	0.06 ± 0.01
160	5465	20	90 ± 8	89.9 ± 0.1	0.71 ± 0.04	0.09 ± 0.01
180	5318	21	85 ± 7	77 ± 2	0.68 ± 0.02	0.08 ± 0.01
200	6656	20	78 ± 8	71 ± 2	0.79 ± 0.06	0.06 ± 0.01
220	8044	6	70 ± 20	47 ± 14	NaN	0.06 ± 0.02
240	NaN	0	NaN	NaN	NaN	NaN
260	NaN	0	NaN	NaN	NaN	NaN
280	NaN	0	NaN	NaN	NaN	NaN
300	7635	10	55 ± 8	60 ± 3	0.83 ± 0.05	0.16 ± 0.02
320	6847	16	60 ± 5	55 ± 2	0.94 ± 0.02	0.19 ± 0.02
340	7175	14	63 ± 6	50 ± 2	0.91 ± 0.02	0.20 ± 0.02

Table C.2: **Rhea**'s longitudinal study values of D, $\bar{\theta}$, m and normalized partial area of the 1.65-micron feature at latitude 30°N.

Lon	Pix Area	# Pixels	D [μm]	$\bar{\theta}$ [deg]	Area [-]	m [-]
0	5471	5	61 ± 11	55 ± 3	0.93 ± 0.04	0.24 ± 0.03
20	1550	3	64 ± 12	49 ± 3	0.87 ± 0.07	0.23 ± 0.03
40	1917	3	65 ± 13	51 ± 3	0.82 ± 0.07	0.22 ± 0.03
60	2297	3	55 ± 13	64 ± 4	0.80 ± 0.03	0.21 ± 0.03
80	7099	4	50 ± 12	67 ± 3	NaN	0.07 ± 0.03
100	7286	22	72 ± 6	70 ± 1	0.81 ± 0.05	0.06 ± 0.01
120	4134	19	85 ± 6	58 ± 2	0.66 ± 0.02	0.16 ± 0.01
140	3813	14	98 ± 8	59 ± 3	0.67 ± 0.03	0.17 ± 0.02
160	4086	16	93 ± 6	58 ± 4	0.69 ± 0.03	0.18 ± 0.01
180	2916	16	86 ± 7	61 ± 3	0.69 ± 0.03	0.18 ± 0.01
200	3753	21	66 ± 5	67 ± 2	0.70 ± 0.03	0.20 ± 0.01
220	5688	19	53 ± 5	64 ± 2	0.70 ± 0.03	0.21 ± 0.01
240	7914	10	69 ± 10	54 ± 5	0.85 ± 0.09	0.23 ± 0.02
260	NaN	0	NaN	NaN	NaN	NaN
280	NaN	0	NaN	NaN	NaN	NaN
300	1256	1	35 ± 20	70 ± 4	$1.14 \pm$ NaN	0.27 ± 0.07
320	3254	4	34 ± 8	74 ± 2	1.00 ± 0.08	0.28 ± 0.03
340	1244	3	45 ± 12	66 ± 3	0.99 ± 0.08	0.27 ± 0.03

Table C.3: **Rhea**'s longitudinal study values of D, $\bar{\theta}$, m and normalized partial area of the 1.65-micron feature along the equator.

Lon	Pix Area	# Pixels	D [μm]	$\bar{\theta}$ [deg]	Area [-]	m [-]
0	2991	2	45 ± 14	69 ± 4	0.98 ± 0.04	0.24 ± 0.04
20	4651	3	59 ± 13	82 ± 1	0.95 ± 0.03	0.19 ± 0.03
40	4605	2	42 ± 20	88 ± 1	1.23 ± 0.05	0.21 ± 0.05
60	7096	1	9 ± 7	80 ± 3	$1.19 \pm$ NaN	0.24 ± 0.07
80	8940	8	27 ± 5	78 ± 1	NaN	0.06 ± 0.02
100	6373	15	103 ± 9	53 ± 3	0.63 ± 0.02	0.15 ± 0.01
120	4553	16	114 ± 8	50 ± 3	0.63 ± 0.02	0.16 ± 0.01
140	3843	18	102 ± 6	52 ± 2	0.64 ± 0.02	0.21 ± 0.01
160	3533	20	99 ± 5	52 ± 2	0.64 ± 0.02	0.21 ± 0.01
180	3606	21	97 ± 5	56 ± 2	0.64 ± 0.03	0.21 ± 0.01
200	2859	17	77 ± 6	63 ± 2	0.64 ± 0.03	0.23 ± 0.01
220	5108	20	52 ± 5	66 ± 1	0.64 ± 0.03	0.25 ± 0.01
240	8080	11	52 ± 7	56 ± 2	0.66 ± 0.05	0.23 ± 0.02
260	7974	1	54 ± 20	46 ± 8	$0.64 \pm$ NaN	0.36 ± 0.04
280	NaN	0	NaN	NaN	NaN	NaN
300	NaN	0	NaN	NaN	NaN	NaN
320	2336	1	25 ± 14	73 ± 4	$1.21 \pm$ NaN	0.31 ± 0.06
340	2837	3	29 ± 9	73 ± 2	1.01 ± 0.07	0.27 ± 0.03

Table C.4: **Rhea**'s longitudinal study values of D, $\bar{\theta}$, m and normalized partial area of the 1.65-micron feature at latitude 30°S.

Lon	Pix Area	# Pixels	D [μm]	$\bar{\theta}$ [deg]	Area [-]	m [-]
0	6304	3	8 ± 5	70 ± 4	1.31 ± 0.09	0.33 ± 0.03
20	4177	2	14 ± 9	55 ± 3	1.22 ± 0.02	0.29 ± 0.04
40	2822	3	10 ± 6	62 ± 2	1.17 ± 0.04	0.31 ± 0.03
60	2323	3	15 ± 8	59 ± 4	1.12 ± 0.07	0.23 ± 0.04
80	9911	5	89 ± 13	76 ± 1	0.72 ± 0.02	0.10 ± 0.02
100	7667	15	97 ± 8	66 ± 2	0.56 ± 0.02	0.17 ± 0.01
120	4116	15	108 ± 8	53 ± 3	0.55 ± 0.03	0.18 ± 0.02
140	3783	18	104 ± 6	54 ± 3	0.54 ± 0.02	0.22 ± 0.01
160	3426	20	100 ± 5	52 ± 2	0.55 ± 0.02	0.22 ± 0.01
180	2758	17	96 ± 6	56 ± 3	0.53 ± 0.03	0.22 ± 0.01
200	3460	16	79 ± 7	64 ± 2	0.53 ± 0.03	0.23 ± 0.01
220	5698	17	60 ± 6	68 ± 2	0.50 ± 0.03	0.25 ± 0.01
240	8473	11	55 ± 7	64 ± 2	0.46 ± 0.05	0.25 ± 0.02
260	NaN	0	NaN	NaN	NaN	NaN
280	NaN	0	NaN	NaN	NaN	NaN
300	NaN	0	NaN	NaN	NaN	NaN
320	NaN	0	NaN	NaN	NaN	NaN
340	7681	2	6 ± 4	82 ± 2	1.25 ± 0.06	0.30 ± 0.05

Table C.5: **Rhea**'s longitudinal study values of D, $\bar{\theta}$, m and normalized partial area of the 1.65-micron feature at latitude 60°S.

Lon	Pix Area	# Pixels	D [μm]	$\bar{\theta}$ [deg]	Area [-]	m [-]
0	2473	1	8 ± 8	73 ± 7	$1.10 \pm$ NaN	0.24 ± 0.06
20	1988	3	15 ± 9	56 ± 5	1.2 ± 0.2	0.22 ± 0.04
40	NaN	0	NaN	NaN	NaN	NaN
60	NaN	0	NaN	NaN	NaN	NaN
80	11125	2	67 ± 20	87 ± 1	0.53 ± 0.02	0.22 ± 0.03
100	9486	10	79 ± 8	86.1 ± 0.4	0.53 ± 0.05	0.19 ± 0.02
120	7679	11	84 ± 8	65 ± 3	0.44 ± 0.03	0.19 ± 0.02
140	5863	14	84 ± 7	67 ± 3	0.44 ± 0.03	0.19 ± 0.01
160	5312	14	87 ± 7	71 ± 3	0.44 ± 0.03	0.20 ± 0.01
180	5531	14	88 ± 7	72 ± 3	0.45 ± 0.03	0.19 ± 0.01
200	7114	14	82 ± 7	70 ± 2	0.43 ± 0.03	0.18 ± 0.01
220	9380	11	80 ± 8	72 ± 2	0.39 ± 0.04	0.20 ± 0.02
240	8963	9	69 ± 8	85 ± 1	0.16 ± 0.14	0.28 ± 0.02
260	NaN	0	NaN	NaN	NaN	NaN
280	NaN	0	NaN	NaN	NaN	NaN
300	NaN	0	NaN	NaN	NaN	NaN
320	NaN	0	NaN	NaN	NaN	NaN
340	NaN	0	NaN	NaN	NaN	NaN

Table C.6: Dione's longitudinal study values of D, $\bar{\theta}$, m and normalized partial area of the 1.65-micron feature at latitude 60°N.

Lon	Pix Area	# Pixels	D [μm]	$\bar{\theta}$ [deg]	Area [-]	m [-]
0	2917	10	51 ± 8	63 ± 3	0.76 ± 0.04	0.17 ± 0.01
20	3197	8	56 ± 9	60 ± 4	0.75 ± 0.04	0.18 ± 0.02
40	3378	7	64 ± 10	60 ± 4	0.72 ± 0.03	0.19 ± 0.02
60	3540	5	73 ± 14	59 ± 6	0.71 ± 0.04	0.18 ± 0.02
80	4523	2	88 ± 29	58 ± 11	0.78 ± 0.04	0.16 ± 0.04
100	NaN	0	NaN	NaN	NaN	NaN
120	4843	5	64 ± 20	NaN	0.55 ± 0.08	0.21 ± 0.02
140	3317	17	74 ± 8	64 ± 3	0.38 ± 0.05	0.19 ± 0.01
160	3652	22	58 ± 5	62 ± 2	0.50 ± 0.04	0.19 ± 0.01
180	3506	24	56 ± 5	59 ± 2	0.53 ± 0.04	0.17 ± 0.01
200	3774	27	47 ± 4	60 ± 2	0.50 ± 0.06	0.18 ± 0.01
220	4080	18	38 ± 5	64 ± 2	0.61 ± 0.06	0.20 ± 0.01
240	3065	8	32 ± 7	61 ± 3	0.35 ± 0.20	0.22 ± 0.02
260	3973	1	27 ± 16	56 ± 7	0.78 ± NaN	0.16 ± 0.05
280	3786	1	38 ± 20	73 ± 4	1.02 ± NaN	0.25 ± 0.04
300	1930	2	NaN	NaN	0.75 ± 0.26	0.16 ± 0.03
320	1637	3	47 ± 14	66 ± 5	0.79 ± 0.18	0.17 ± 0.02
340	3091	7	49 ± 9	64 ± 3	0.70 ± 0.05	0.17 ± 0.02

Table C.7: Dione's longitudinal study values of D, $\bar{\theta}$, m and normalized partial area of the 1.65-micron feature at latitude 30°N.

Lon	Pix Area	# Pixels	D [μm]	$\bar{\theta}$ [deg]	Area [-]	m [-]
0	1352	13	54 ± 7	68 ± 2	0.83 ± 0.04	0.21 ± 0.01
20	2228	16	64 ± 6	60 ± 3	0.88 ± 0.03	0.20 ± 0.01
40	2471	11	72 ± 8	59 ± 4	0.84 ± 0.02	0.21 ± 0.02
60	2064	11	72 ± 9	64 ± 4	0.82 ± 0.03	0.19 ± 0.02
80	2826	7	66 ± 10	74 ± 4	0.80 ± 0.03	0.17 ± 0.02
100	4356	12	65 ± 10	82 ± 1	0.72 ± 0.11	0.13 ± 0.02
120	2216	21	66 ± 5	66 ± 2	0.68 ± 0.03	0.14 ± 0.01
140	1657	15	72 ± 6	69 ± 3	0.66 ± 0.03	0.15 ± 0.01
160	1555	13	69 ± 6	61 ± 3	0.59 ± 0.04	0.15 ± 0.01
180	1876	21	65 ± 5	60 ± 2	0.67 ± 0.05	0.16 ± 0.01
200	2418	27	50 ± 4	66 ± 1	0.64 ± 0.05	0.18 ± 0.01
220	2675	30	33 ± 3	73 ± 1	0.70 ± 0.05	0.19 ± 0.01
240	3268	17	32 ± 4	71 ± 1	0.84 ± 0.05	0.12 ± 0.01
260	4435	3	24 ± 8	72 ± 2	0.87 ± 0.01	0.07 ± 0.05
280	2556	1	51 ± 21	66 ± 6	1.09 ± NaN	0.22 ± 0.05
300	1914	6	16 ± 6	72 ± 2	NaN ± 1.34	0.24 ± 0.02
320	2256	8	22 ± 6	79 ± 1	0.87 ± 0.08	0.22 ± 0.02
340	1700	12	35 ± 6	76 ± 1	0.81 ± 0.06	0.21 ± 0.01

Table C.8: **Dione**'s longitudinal study values of D, $\bar{\theta}$, m and normalized partial area of the 1.65-micron feature along the equator.

Lon	Pix Area	# Pixels	D [μm]	$\bar{\theta}$ [deg]	Area [-]	m [-]
0	1793	18	54 ± 6	75 ± 2	0.95 ± 0.05	0.21 ± 0.01
20	1897	19	73 ± 5	64 ± 2	0.98 ± 0.04	0.20 ± 0.01
40	2439	15	74 ± 6	58 ± 2	0.97 ± 0.03	0.21 ± 0.01
60	1732	10	70 ± 8	64 ± 4	0.90 ± 0.03	0.17 ± 0.02
80	2910	8	63 ± 9	71 ± 3	0.86 ± 0.03	0.14 ± 0.02
100	3440	17	66 ± 8	81 ± 1	0.71 ± 0.05	0.10 ± 0.01
120	2173	13	63 ± 7	69 ± 2	0.71 ± 0.03	0.16 ± 0.01
140	1533	10	77 ± 8	56 ± 3	0.71 ± 0.04	0.17 ± 0.02
160	1286	13	79 ± 6	53 ± 2	0.67 ± 0.05	0.18 ± 0.01
180	1662	23	76 ± 5	58 ± 1	0.75 ± 0.04	0.19 ± 0.01
200	2083	25	53 ± 5	66 ± 1	0.77 ± 0.07	0.22 ± 0.01
220	2531	29	31 ± 3	77 ± 1	0.78 ± 0.07	0.24 ± 0.01
240	2562	22	25 ± 3	79 ± 1	0.82 ± 0.07	0.19 ± 0.01
260	4762	1	15 ± 12	86 ± 1	$1.34 \pm$ NaN	0.22 ± 0.05
280	NaN	0	NaN	NaN	NaN	NaN
300	1713	9	42 ± 12	69 ± 3	0.84 ± 0.12	0.19 ± 0.02
320	1529	12	24 ± 5	84 ± 1	1.04 ± 0.05	0.23 ± 0.02
340	1205	15	36 ± 6	83 ± 1	0.98 ± 0.05	0.23 ± 0.01

Table C.9: **Dione**'s longitudinal study values of D, $\bar{\theta}$, m and normalized partial area of the 1.65-micron feature at latitude 30°S.

Lon	Pix Area	# Pixels	D [μm]	$\bar{\theta}$ [deg]	Area [-]	m [-]
0	1024	18	54 ± 6	70 ± 2	0.97 ± 0.03	0.17 ± 0.01
20	1730	19	68 ± 6	60 ± 3	1.02 ± 0.03	0.17 ± 0.01
40	2606	13	68 ± 7	59 ± 3	0.95 ± 0.03	0.19 ± 0.01
60	1831	10	63 ± 8	64 ± 3	0.93 ± 0.02	0.16 ± 0.02
80	3924	10	56 ± 8	69 ± 2	0.93 ± 0.04	0.05 ± 0.02
100	3233	11	62 ± 9	58 ± 3	0.68 ± 0.06	0.10 ± 0.01
120	2089	15	66 ± 7	56 ± 3	0.75 ± 0.05	0.16 ± 0.01
140	1798	13	75 ± 7	55 ± 3	0.76 ± 0.05	0.17 ± 0.01
160	2219	16	71 ± 6	58 ± 2	0.75 ± 0.05	0.18 ± 0.01
180	2419	21	64 ± 5	61 ± 2	0.80 ± 0.05	0.18 ± 0.01
200	2061	27	50 ± 4	71 ± 1	0.77 ± 0.05	0.19 ± 0.01
220	2501	22	35 ± 4	76 ± 1	0.72 ± 0.08	0.20 ± 0.01
240	4327	9	34 ± 7	79 ± 1	0.52 ± 0.13	0.19 ± 0.01
260	4545	1	11 ± 9	81 ± 2	$0.97 \pm$ NaN	0.24 ± 0.04
280	2795	1	10 ± 9	80 ± 2	$1.12 \pm$ NaN	0.32 ± 0.04
300	1154	8	43 ± 13	83 ± 2	0.72 ± 0.07	0.23 ± 0.02
320	1726	14	33 ± 6	84 ± 1	0.88 ± 0.09	0.20 ± 0.01
340	1352	17	48 ± 6	76 ± 2	0.98 ± 0.03	0.17 ± 0.01

Table C.10: Dione's longitudinal study values of D, $\bar{\theta}$, m and normalized partial area of the 1.65-micron feature at latitude 60°S.

Lon	Pix Area	# Pixels	D [μm]	$\bar{\theta}$ [deg]	Area [-]	m [-]
0	1558	12	51 ± 8	67 ± 3	0.93 ± 0.04	0.15 ± 0.02
20	1944	14	51 ± 7	66 ± 2	0.99 ± 0.05	0.15 ± 0.01
40	2105	13	56 ± 8	63 ± 3	0.97 ± 0.04	0.15 ± 0.01
60	2715	8	58 ± 9	60 ± 3	1.02 ± 0.06	0.11 ± 0.02
80	4557	14	60 ± 7	79 ± 1	0.90 ± 0.04	-0.01 ± 0.01
100	3605	11	61 ± 10	80 ± 1	0.78 ± 0.11	-0.02 ± 0.01
120	3237	10	66 ± 9	58 ± 3	0.62 ± 0.04	0.16 ± 0.01
140	2910	11	66 ± 8	60 ± 3	0.67 ± 0.05	0.16 ± 0.02
160	2490	10	60 ± 7	62 ± 3	0.72 ± 0.08	0.16 ± 0.02
180	2130	15	55 ± 6	64 ± 2	0.64 ± 0.05	0.17 ± 0.01
200	3131	18	48 ± 5	69 ± 1	0.68 ± 0.06	0.15 ± 0.01
220	3562	12	46 ± 6	86.4 ± 0.4	0.61 ± 0.09	0.15 ± 0.01
240	3908	7	54 ± 10	88.5 ± 0.3	0.53 ± 0.09	0.13 ± 0.01
260	NaN	0	NaN	NaN	NaN	NaN
280	4153	1	NaN	NaN	0.98 ± NaN	0.30 ± 0.06
300	1506	6	22 ± 9	64 ± 5	NaN ± 29.06	0.25 ± 0.02
320	1740	10	44 ± 9	75 ± 2	1.00 ± 0.09	0.13 ± 0.02
340	2121	13	46 ± 6	68 ± 2	1.01 ± 0.05	0.13 ± 0.01

Table C.11: Enceladus' longitudinal study values of D, $\bar{\theta}$, m and normalized partial area of the 1.65-micron feature at latitude 60°N.

Lon	Pix Area	# Pixels	D [μm]	$\bar{\theta}$ [deg]	Area [-]	m [-]
0	688	20	74 ± 7	42 ± 4	NaN	0.18 ± 0.02
20	673	25	64 ± 6	48 ± 3	2.03 ± 1.26	0.19 ± 0.02
40	675	27	79 ± 6	46 ± 3	0.74 ± 0.03	0.17 ± 0.02
60	674	27	84 ± 7	44 ± 3	0.79 ± 0.03	0.16 ± 0.01
80	742	25	87 ± 8	53 ± 3	0.77 ± 0.03	0.14 ± 0.02
100	837	19	101 ± 10	63 ± 2	0.85 ± 0.06	0.15 ± 0.02
120	902	8	95 ± 13	81 ± 1	0.80 ± 0.07	0.13 ± 0.03
140	976	8	81 ± 11	52 ± 5	0.84 ± 0.05	0.20 ± 0.02
160	930	9	82 ± 11	47 ± 6	0.80 ± 0.03	0.21 ± 0.02
180	979	12	81 ± 10	47 ± 6	0.85 ± 0.02	0.21 ± 0.02
200	955	10	76 ± 12	48 ± 8	0.97 ± 0.07	0.17 ± 0.02
220	843	4	94 ± 15	46 ± 15	1.00 ± 0.07	0.12 ± 0.03
240	821	5	65 ± 14	60 ± 4	1.38 ± 0.45	0.03 ± 0.03
260	777	3	115 ± 19	34 ± 8	0.84 ± 0.10	0.08 ± 0.03
280	767	4	91 ± 16	71 ± 3	-0.05 ± 1.01	0.12 ± 0.04
300	472	5	100 ± 21	NaN	0.98 ± 0.17	0.13 ± 0.03
320	660	9	102 ± 13	42 ± 7	0.75 ± 0.07	0.12 ± 0.03
340	659	15	84 ± 9	83 ± 1	0.82 ± 0.06	0.19 ± 0.02

Table C.12: Enceladus' longitudinal study values of D, $\bar{\theta}$, m and normalized partial area of the 1.65-micron feature at latitude 30°N.

Lon	Pix Area	# Pixels	D [μm]	$\bar{\theta}$ [deg]	Area [-]	m [-]
0	536	29	71 ± 5	38 ± 4	NaN	0.22 ± 0.02
20	633	44	78 ± 4	40 ± 2	0.82 ± 0.01	0.20 ± 0.01
40	575	45	86 ± 4	41 ± 2	0.84 ± 0.02	0.18 ± 0.01
60	529	43	103 ± 4	45 ± 2	0.89 ± 0.03	0.15 ± 0.01
80	636	46	111 ± 5	55 ± 2	0.85 ± 0.02	0.12 ± 0.01
100	650	34	108 ± 6	54 ± 2	0.87 ± 0.07	0.13 ± 0.02
120	928	24	100 ± 7	62 ± 2	0.89 ± 0.03	0.13 ± 0.01
140	800	20	100 ± 6	49 ± 3	0.81 ± 0.01	0.18 ± 0.01
160	696	20	99 ± 6	44 ± 3	0.79 ± 0.01	0.24 ± 0.01
180	682	26	90 ± 5	45 ± 2	0.81 ± 0.03	0.23 ± 0.01
200	694	26	83 ± 5	42 ± 3	0.81 ± 0.02	0.21 ± 0.01
220	864	22	89 ± 7	45 ± 4	0.84 ± 0.03	0.17 ± 0.01
240	837	9	74 ± 11	57 ± 4	0.93 ± 0.12	0.12 ± 0.02
260	646	12	87 ± 10	66 ± 2	0.84 ± 0.15	0.07 ± 0.02
280	178	4	82 ± 14	50 ± 7	0.61 ± 0.04	0.13 ± 0.03
300	187	1	97 ± 27	49 ± 20	$0.68 \pm$ NaN	0.05 ± 0.05
320	888	3	95 ± 25	41 ± 17	0.68 ± 0.07	0.23 ± 0.03
340	597	17	79 ± 8	47 ± 6	0.99 ± 0.16	0.26 ± 0.02

Table C.13: Enceladus' longitudinal study values of D, $\bar{\theta}$, m and normalized partial area of the 1.65-micron feature along the equator.

Lon	Pix Area	# Pixels	D [μm]	$\bar{\theta}$ [deg]	Area [-]	m [-]
0	461	34	56 ± 4	43 ± 3	NaN	0.21 ± 0.01
20	570	46	82 ± 4	42 ± 2	0.84 ± 0.02	0.18 ± 0.01
40	487	46	87 ± 3	42 ± 2	0.85 ± 0.02	0.17 ± 0.01
60	526	47	95 ± 4	43 ± 2	0.88 ± 0.02	0.16 ± 0.01
80	594	43	100 ± 4	49 ± 2	0.91 ± 0.02	0.12 ± 0.01
100	662	32	99 ± 6	61 ± 2	0.81 ± 0.04	0.11 ± 0.02
120	887	24	97 ± 7	61 ± 2	0.82 ± 0.03	0.16 ± 0.02
140	688	19	100 ± 6	42 ± 3	0.84 ± 0.01	0.20 ± 0.01
160	645	28	90 ± 5	48 ± 2	0.74 ± 0.03	0.22 ± 0.01
180	558	31	81 ± 4	43 ± 2	0.77 ± 0.02	0.22 ± 0.01
200	568	31	81 ± 4	40 ± 2	0.79 ± 0.02	0.19 ± 0.01
220	725	28	84 ± 5	41 ± 3	0.80 ± 0.02	0.16 ± 0.01
240	704	18	89 ± 8	68 ± 2	0.91 ± 0.05	0.09 ± 0.02
260	453	5	93 ± 14	65 ± 4	0.54 ± 0.08	0.07 ± 0.03
280	620	2	89 ± 20	51 ± 8	0.66 ± 0.02	0.12 ± 0.05
300	162	1	88 ± 21	38 ± 10	$0.91 \pm$ NaN	0.14 ± 0.05
320	787	5	84 ± 11	44 ± 4	0.85 ± 0.10	0.17 ± 0.03
340	467	9	44 ± 7	45 ± 4	NaN $\pm$ 2.83	0.17 ± 0.03

Table C.14: Enceladus' longitudinal study values of D, $\bar{\theta}$, m and normalized partial area of the 1.65-micron feature at latitude 30°S.

Lon	Pix Area	# Pixels	D [μm]	$\bar{\theta}$ [deg]	Area [-]	m [-]
0	553	34	89 ± 5	54 ± 3	1.04 ± 0.06	0.16 ± 0.02
20	574	47	89 ± 4	42 ± 2	0.93 ± 0.03	0.16 ± 0.01
40	536	53	88 ± 4	42 ± 2	0.87 ± 0.02	0.16 ± 0.01
60	536	45	97 ± 4	47 ± 2	0.91 ± 0.02	0.15 ± 0.01
80	587	50	95 ± 4	60 ± 2	0.86 ± 0.04	0.14 ± 0.01
100	638	20	95 ± 8	76 ± 2	0.92 ± 0.02	0.09 ± 0.02
120	851	19	88 ± 8	84 ± 1	0.88 ± 0.02	0.14 ± 0.02
140	814	24	90 ± 6	62 ± 2	0.83 ± 0.02	0.18 ± 0.01
160	643	34	84 ± 5	58 ± 2	0.79 ± 0.02	0.16 ± 0.01
180	600	32	84 ± 5	47 ± 2	0.77 ± 0.03	0.17 ± 0.01
200	690	28	83 ± 5	47 ± 3	0.83 ± 0.03	0.16 ± 0.01
220	890	26	86 ± 6	66 ± 2	0.90 ± 0.02	0.11 ± 0.01
240	797	8	61 ± 9	71 ± 2	1.01 ± 0.21	0.08 ± 0.02
260	334	3	76 ± 17	45 ± 8	0.70 ± 0.09	0.09 ± 0.04
280	567	9	84 ± 10	56 ± 4	0.70 ± 0.07	0.15 ± 0.03
300	314	7	79 ± 11	50 ± 4	0.84 ± 0.08	0.15 ± 0.03
320	500	11	81 ± 9	51 ± 3	0.84 ± 0.05	0.18 ± 0.02
340	420	25	88 ± 6	51 ± 2	0.99 ± 0.09	0.20 ± 0.02

Table C.15: Enceladus' longitudinal study values of D, $\bar{\theta}$, m and normalized partial area of the 1.65-micron feature at latitude 60°S.

Lon	Pix Area	# Pixels	D [μm]	$\bar{\theta}$ [deg]	Area [-]	m [-]
0	552	21	94 ± 8	56 ± 2	0.85 ± 0.08	0.18 ± 0.02
20	528	28	84 ± 6	59 ± 2	0.91 ± 0.05	0.14 ± 0.02
40	542	31	92 ± 6	61 ± 1	0.94 ± 0.05	0.16 ± 0.02
60	517	34	93 ± 6	64 ± 1	0.82 ± 0.03	0.17 ± 0.02
80	674	20	105 ± 9	55 ± 3	0.81 ± 0.03	0.22 ± 0.02
100	748	8	97 ± 14	67 ± 3	0.88 ± 0.02	0.12 ± 0.03
120	847	11	93 ± 11	71 ± 2	0.86 ± 0.06	0.06 ± 0.02
140	660	17	94 ± 8	73 ± 1	0.55 ± 0.05	0.28 ± 0.01
160	755	23	95 ± 7	73 ± 1	0.72 ± 0.05	0.22 ± 0.01
180	694	24	107 ± 7	58 ± 2	0.66 ± 0.04	0.24 ± 0.01
200	730	15	105 ± 10	54 ± 3	0.73 ± 0.05	0.23 ± 0.02
220	575	5	104 ± 14	52 ± 4	0.69 ± 0.12	0.18 ± 0.03
240	584	8	106 ± 12	71 ± 2	0.55 ± 0.04	0.16 ± 0.02
260	642	10	90 ± 10	83 ± 1	0.61 ± 0.09	0.15 ± 0.02
280	483	7	70 ± 9	87.6 ± 0.3	0.56 ± 0.13	0.21 ± 0.03
300	594	7	81 ± 11	60 ± 3	0.69 ± 0.13	0.20 ± 0.03
320	750	13	77 ± 8	67 ± 1	1.72 ± 0.70	0.14 ± 0.03
340	693	17	76 ± 7	60 ± 2	1.55 ± 0.54	0.18 ± 0.02

Table C.16: Rhea's values of D, $\bar{\theta}$, m and normalized partial area of the 1.65-micron feature for comparative study.

Location	Pix Area [km^2]	# Pixels	D [μm]	$\bar{\theta}$ [deg]	m [-]	Area [-]
0° N 0° W	2991	2	45 ± 14	69 ± 4	0.24 ± 0.04	0.98 ± 0.04
0° N 90° W	8818	12	90 ± 9	70 ± 1	0.10 ± 0.02	0.73 ± 0.03
0° N 180° W	3606	21	97 ± 5	56 ± 2	0.21 ± 0.01	0.64 ± 0.03
0° N 260° W	7974	1	54 ± 20	46 ± 8	0.36 ± 0.04	$0.64 \pm$ NaN
90° N 0° W	5612	8	61 ± 8	60 ± 3	0.20 ± 0.02	0.86 ± 0.04
70° S 180° W	7805	11	86 ± 8	79 ± 2	0.18 ± 0.02	0.43 ± 0.03

Table C.17: Dione's values of D, $\bar{\theta}$, m and normalized partial area of the 1.65-micron feature for comparative study.

Location	Pix Area [km^2]	# Pixels	D [μm]	θ [deg]	m [-]	Area [-]
0° N 0° W	1793	18	54 ± 6	75 ± 2	0.21 ± 0.01	0.95 ± 0.05
0° N 90° W	4196	16	67 ± 7	71 ± 2	0.08 ± 0.01	0.87 ± 0.03
0° N 180° W	1661	23	76 ± 5	58 ± 1	0.19 ± 0.01	0.75 ± 0.04
0° N 270° W	2829	1	10 ± 10	83 ± 2	0.31 ± 0.03	$1.45 \pm$ NaN
70° N 0° W	2562	6	53 ± 11	61 ± 4	0.16 ± 0.02	0.73 ± 0.03
70° S 180° W	2794	9	66 ± 8	75 ± 1	2.0267 ± 0.0002	0.56 ± 0.02

Table C.18: Enceladus' values of D, $\bar{\theta}$, m and normalized partial area of the 1.65-micron feature for comparative study.

Location	Pix Area [km^2]	# Pixels	D [μm]	θ [deg]	m [-]	Area [-]
0° N 0° W	461	34	56 ± 4	43 ± 3	0.21 ± 0.01	0.89 ± 0.04
0° N 90° W	647	41	101 ± 5	54 ± 2	0.11 ± 0.01	0.87 ± 0.03
0° N 180° W	662	22	81 ± 4	43 ± 2	0.22 ± 0.01	0.77 ± 0.02
0° N 270° W	552	4	60 ± 12	62 ± 4	0.12 ± 0.03	0.79 ± 0.20
80° N 0° W	880	6	82 ± 15	44 ± 5	0.12 ± 0.04	0.74 ± 0.04
90° S 0° W	567	8	144 ± 15	70 ± 2	0.46 ± 0.03	0.37 ± 0.03